The Dissertation Committee for Otitoaleke Gideon Akinola Certifies that this is the approved version of the following dissertation:

Magnetic Materials: Fundamental Synthesis of Two-Dimensional Magnets and Applications to Neuromorphic Computing

Committee:

Jean Anne Incorvia, Supervisor

Deji Akinwande

Brian Korgel

Frank Register

Edward Yu

Magnetic Materials: Fundamental Synthesis of Two-Dimensional Magnets and Applications to Neuromorphic Computing

by

Otitoaleke Gideon Akinola

Dissertation

Presented to the Faculty of the Graduate School of

The University of Texas at Austin

in Partial Fulfillment

of the Requirements

for the Degree of

Doctor of Philosophy

The University of Texas at Austin

May 2021

Dedication

This is dedicated to all those who persist despite daunting challenges. To those who stand up against injustice and systemic oppression. And to the God who controls the forces of the universe in our favor.

Acknowledgements

I am grateful to God who has blessed me immeasurably with people and opportunities that He has strategically placed in my life. My PhD years have been a time of growth enabled by a host of people.

First, I deeply appreciate my amazing advisor Dr. Jean Anne Incorvia who has provided her full support at all fronts – her tutelage and professional guidance throughout my research have been very pivotal to my success. She provided the mentorship and the technical/professional exposure that I needed at a critical time of my PhD journey. I am also grateful to Dr. Deji Akinwande for giving me the head start at the inception of my PhD program.

Moreover, I would like to thank Dr. Deji Akinwande, Dr Brian Korgel, Dr Leonard Frank Register, and Dr. Edward Yu, for serving on my dissertation committee, and for their immeasurable suggestions and advice on my research.

The Center for Dynamics and Control of Materials, an NSF MRSEC at UT gave me multidisciplinary research exposure and grounds for growth. I learned a great deal from almost all stakeholders in the center. My interactions with the faculties, staff, post-docs, and students bolstered my confidence in curiosity-driven research. Through the center I also met one of my industry mentors, Ben Rathsack whose career tips and advice have been priceless.

I would like to thank all my graduate group members at the Integrated Nano Computing (INC) Lab – Suyogya Karki, Mahshid Alamdar, Can Cui, Xintong Li, Sam Liu, Thomas Leonard – for their immense help and support on different occasions and collaborations on various projects. I appreciate the great assistance that the undergraduate researchers – Vivian Rogers, Isha Chakraborty, Bendy Mendawar, Bishweshwor Rimal and Eun Jin Kim – gave to my research. I admire their passion and hunger for knowledge.

Special thanks to Maruthi Nagavalliyogeesh, Amritesh Rai, Nitin Prasad, Tanmoy Pramanik, Michael Rodder, Hasibul Alam who helped me especially at the early stages of my PhD journey to learn a lot of the fabrication and theoretical skills integral to the success of my research. It is also important for me to mention Willy Vasquez and Venkata Rayudu. We served on the board of Graduate ECE together and they eventually became my friends in other ECE tracks that I run to whenever I need insights and perspectives from their field.

I have learned a great deal from my collaborators including Dr. Joseph Friedman, Naimul Hassan, Xuan Hu, and Wesley Brigner from the department of Electrical and Computer Engineering at the university of Texas at Dallas; Dr. Tianyao Xiao, Dr. Christopher Bennet and Dr. Matthew Marinella from the Sandia National Labs; and Levisse Alexandre from École polytechnique fédérale de Lausanne (EPFL). Every of my interactions with them gave me new perspectives and insights.

My sincere thanks to the staffs of the Microelectronics Research Center (especially Ricardo Garcia, William James, Sarmita Majumder, and the late Johnny Johnson) and of the Texas Materials Institute (especially Hugo Celio, Raluca Gearba, Steve Swinnea, Andrei Dolocan, and Karalee Jarvis) for training me on the tools that I needed and providing necessary help with synthesis, measurement, or analysis whenever I need it. Also, thanks to the staff of the UT Electrical and Computer Engineering Department: Jean Toll, Melanie Gulick, Melody Singleton, Christine Wood for their help in all administrative matters.

My research internships at IBM Yorktown Heights, and NXP Semiconductors Austin were greatly enriching. They gave me exposure to research at the industry level and the opportunity to learn from great minds. In addition, the Brumley Next Generation Fellowship on International Law and Security challenged me to think about my research from a policy and security standpoint.

It is vital for me to appreciate the emotional support that I get from the Graduate InterVarsity (GradIV) at UT led by Tim Wang. It has been awesome to have Brandon Crooms, Michael Wade, and Joshua Chen, who are fellow PhD students in my support group. Their prayers and vulnerability helped a great deal.

Last but not least, I am greatly indebted to my family for their unconditional love, support, encouragement, and prayers throughout my graduate research. I am deeply grateful to my parents who gave me the foundations on which I could build on. My siblings, Ireti and his wife Simone, Funke, and Bidemi, were steadfast in their support and gave me a lot of personal and technical feedback. Finally, I would like to thank my close relatives and friends, too numerous to name, for their love and support.

Abstract

Magnetic Materials: Fundamental Synthesis of Two-Dimensional Magnets and Applications to Neuromorphic Computing

Otitoaleke Gideon Akinola, Ph.D.

The University of Texas at Austin, 2021

Supervisor: Jean Anne Incorvia

Two dimensional magnetic materials hold the promise of helping to achieve beyond CMOS computing tasks. 2D magnetic materials can be used in fabricating magnetic tunnel junctions with higher tunnel magnetoresistance which can then be applied to making new neuromorphic computing architectures primarily geared towards artificial intelligence and machine learning applications.

In this work I summarize my synthesis and investigation of the properties of Cr_2C which belongs to the group of 2D transition metal carbides or nitrides called MXenes. Cr_2C has been predicted to have intrinsic half metallic ferromagnetic behaviors. These magnetic behaviors can be tuned based on the level of functionalization of the surface of the material. I show different parameters such as etchant, reaction temperature, and molar concentration that I have tuned in order to optimally derive Cr_2C from its parent MAX phase Cr_2AlC by removing the Al layer with a fluoride salt and hydrochloric acid.

I also show how magnetic tunnel junctions (MTJs), which are two ferromagnetic layers with a tunnel barrier in between, can be used to make a synapse which is a neuromorphic computing primitive. The synapse circuit that I have proposed displays spike timing dependent plasticity which is an integral component of learning and memory in the brain. I show how different delay conditions between the presynaptic signal and the

postsynaptic signal lead to currents of different magnitudes flowing through the ferromagnetic layer of the magnetic tunnel junction synapse. I also show how these currents move the domain wall both in micromagnetic simulation and using a domain wall MTJ Spice model that has been developed. I went on to wire four of these synapses together to observe the temporal dynamics of the system. My results show that the lower the delay between the presynaptic pulse and the postsynaptic pulse, the higher the current through the MTJ synapse and hence the larger the domain wall displacement.

These studies pave the way for empirical understanding of the Cr_2C MXene, including its potential magnetic properties, as well as doing online machine learning classification tasks with arrays of magnetic synapses.

Table of Contents

List of Tables

List of Figures

Chapter 1: Introduction

The movement of charges and the spin of elementary particles are the fundamental basis of magnetism. Electrons are relatively stable, light, long-lived, and present in all observable matter, making them easily exploited in application. Each electron revolves around the nucleus of an atom contributing to its orbital angular momentum (L) and represented by the orbital angular momentum quantum number l. Each electron also spins on its own axis (in the classical picture) thereby acquiring a spin angular momentum (S) represented by the spin angular momentum quantum number s. These two momentum quantities contribute to the electron's magnetic moment. The spontaneous alignment of the electron's magnetic moment in a material due to exchange interactions give rise to its magnetism. When magnetic moments collectively align in the same direction in a material as a result of inherent coupling, the material is said to be ferromagnetic[1].

1.1. Two Dimensional Magnetic Materials

In a ferromagnet, this alignment has to be long range and stable against thermal fluctuations. According to the Mermin-Wagner theorem, enhanced thermal fluctuations may make ferromagnetism a hard reality in two-dimensional (2D) systems [2]. However, recent discoveries make us know that by opening up magnon excitation gap to resist thermal agitation, magnetic anisotropy can stabilize the long-range magnetic order in 2D magnetic crystals. These 2D magnets are however still challenging to synthesize.

A couple of properties make 2D magnets attractive for applications in emergent technologies such as ultra-dense spintronics, on-chip optical communications, and quantum computing. These properties which include their mechanical flexibility and their ability to largely decouple from their substrates in addition to allowing for electrical control

and chemical functionalization sets them apart from the traditional magnetic thin films. Their low dimensionality and flexibility offer great access to their ground states and allows for engineering them for a swath array of external stimuli – such as electrostatic doping, light incidence, mechanical deformation, chemical decoration – while responding sensitively to magneto-resistive, magneto-electric, magneto-optical and magneto-biological effects[3].

In the past two decades, several approaches have been taken towards achieving tunable magnetism in 2D crystals like graphene and monolayer transition metal dichalcogenide. Some of these explored the possibility of extrinsically inducing magnetic response using proximity effect to induce spin polarization from a magnetic substrate such as depositing magnetic adatoms on the surface or edges, defect engineering by carefully introducing surface or edge defects, band structure engineering, among other methods [3–14]. These approaches are however experimentally challenging. Not until the early 2017 were the first observations of intrinsic long-range magnetic ordering made in pristine 2D crystals of $Cr_2Ge_2Te_6$ and CrI_3. $Cr_2Ge_2Te_6$ is a 2D Heisenberg ferromagnet with small magnetic anisotropy with a measured Curie temperature (T_C) of 30 K for the bilayer[15] whereas CrI_3 is a 2D Ising A-type antiferromagnet for the bilayer [3,16] and ferromagnetic for the monolayer with a measured T_C of 61 K [16–19]. Subsequently, isostructural structures of $Cr_2Ge_2Te_6$ and CrI_3 have been identified including $Cr_2Si_2Te_6$ [20], $Cr_2Sn_2Te_6$ [21], $CrBr_3$ [22], $CrCl_3$ [23–25]. Other 2D crystals that have been identified include $CrCl_{3-x}Br_x$ which has increasing T_C from 33 K to 63K with increasing value for x [26], and Fe_3GeTe_2 which is a Stoner ferromagnetic metal with a tunable T_C of ~200 – 230 K [27–34].

However, most of this intrinsic 2D magnets can only be derived by mechanical exfoliation. They also typically have very low Curie temperatures: much lower than those of their 3D counterparts. Hence, to see more practical applications, more work is needed in wafer-scale synthesis of 2D magnets that operate at room temperature in addition to developing techniques for integrating them with the existing semiconductor fabrication process and CMOS technologies.

Apart from the fact that the 2D properties of the material will result in higher TMR, lower energy losses, higher switching speeds, and higher circuit density, their successful synthesis provides a viable pathway towards integration with excellent materials like graphene in memory in logic computing architecture of the future.

1.2. 2D TRANSITION METAL CARBIDES/NITRIDES (MXENES)

2D MXenes are a large class of 2D layered transition metal carbides and/or nitrides, discovered in 2011[35], with the general formula $M_{n+1}X_nT_m$. They are derived by the selective removal of the "A" layers from MAX phases, which are ternary carbides, nitrides or carbonitrides with the general formula $M_{n+1}AX_n$ $(n = 1 - 3)$; where $M =$ early transition metal e.g. Ti, V, Cr, and Mo; A is mainly a group 13 or 14 element; $X = C$ or N; and T_m is surface functional groups, OH, O or F. The MAX phase is structured such that the stacks of $M_{n+1}X_n$ nanosheets are interleaved with "A" layers which can be chemically etched out. This results in weakly bonded $M_{n+1}X_n$ layers which can be exfoliated into MXenes, as illustrated in Fig. 1.1 using the Vesta visualization software.

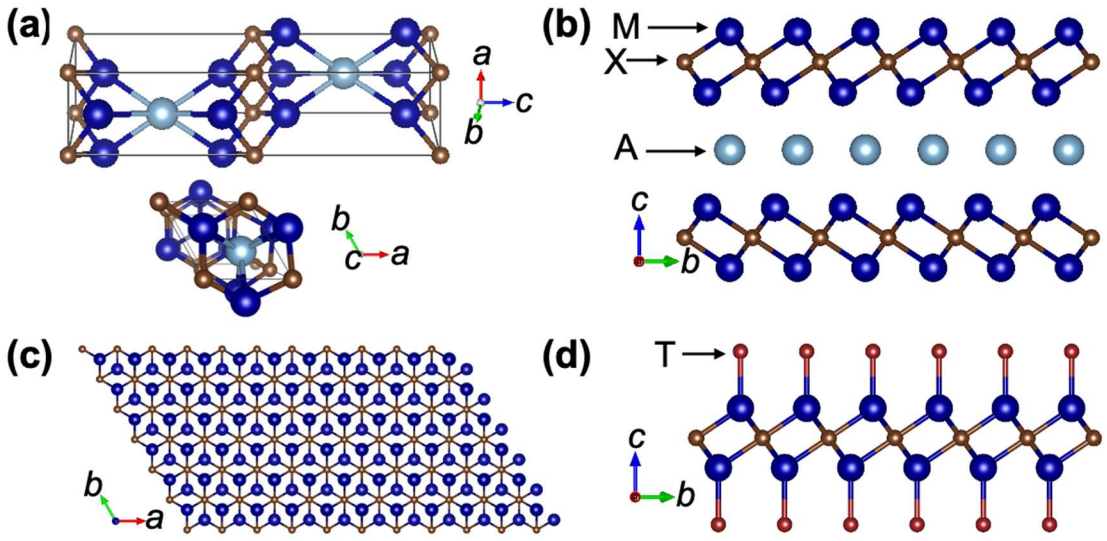

Figure 1.1: MAX and MXene crystal structure. Cartoon images of: (a) The MAX phase; the view along the c^direction is shown in the inset. (b) Unetched MAX phase along the $\hat{a}$ direction, with elements identified as transition metal M (Cr in this case), group III element A (Al in this case), and carbon or nitrogen X (carbon in this case) to form Cr2AlC. The A atoms are chemically etched to produced Cr2C MXenes, shown in (c) in the $\hat{c}$ direction after etching. (d) Cr2C MXene sheet in the $\hat{a}$ direction after surface functionalization, where T is an F, O, H or OH radical.

MXenes have been shown to demonstrate excellent mechanical and electronic properties[36,37]. They have also been predicted and shown to have many great applications in electrode materials[38], sensors, catalysis[39], and energy storage[40–43], and carbon capture[44]. MXenes can also have magnetic properties[45]. For example, from theory, pristine Ti_2C and Ti_2N are nearly half-metallic ferromagnets, Cr_2N is antiferromagnetic, and Cr_2C is a half-metallic ferromagnet which can undergo ferromagnetic metallic to anti-ferromagnetic insulating state transitions[45]. However, significant work needs to be done to synthesize these MXene species to test and use their predicted properties.

Cr_2C MXene has a trigonal crystal structure and a P3m1 [164] space group. It is produced by selectively etching Al atoms from the MAX phase Cr2AlC. Two-dimensional Cr_2C MXenes have been predicted, using density functional theory calculations, to have to have ferromagnetic behavior in which the itinerant Cr d electrons introduces intrinsic half-metallicity with a gap as large as 2.85 eV[46]. These itinerant Cr d electrons are 100% spin polarized around the Fermi surface. Cr_2C has also been predicted to demonstrate a ferromagnetic to antiferromagnetic transition accompanied by a metal to insulator transition when the surface is functionalized with F, OH, H, or Cl groups due to the localization of the Cr d electrons[46]. The energy gap is also tunable by the choice of the functional group[46]. This half-metallicity in Cr_2C MXenes is completely intrinsic, in contrast to many low-dimensional materials such as graphene or transition metal dichalcogenides which need strong external electric field or carefully selective doping to induce half-metallicity[46]. Cr_2C has also been predicted to demonstrate a ferromagnetic-to-antiferromagnetic transition accompanied by a metal-to-insulator transition when the surface is functionalized with F, OH, H, or Cl groups due to the localization of the Cr *d* electrons[46]. The energy gap is also tunable by the choice of the functional group[46]. This makes Cr_2C MXenes potentially attractive for nanoscale spintronics applications if Cr_2C MXene nanosheets could be reliably produced experimentally.

In this dissertation I have highlighted my methods of synthesizing Cr_2C and the characterization results. Though more work is essential at optimizing the synthesis techniques and in obtaining more detailed data, I believe that my work is an important first step in the direction of large scale application of this MXene material in magnetic, sensor, and neuromorphic applications in the electronics world.

1.3. MAGNETIC TUNNEL JUNCTIONS (MTJS)

The magnetic tunnel junction (MTJ) is one of the fundamental building blocks for the state-of-the art spintronics technology. One of the advantages of an MTJ device with all 2D material is the possibility of an all-area tunneling thereby achieving optimal efficiency. Hence, while work is still ongoing towards perfecting the synthesis of 2D magnets and developing techniques to integrate them into existing MTJ fabrication process, it is imperative that the frontiers of use cases for the MTJ device is being pushed forward simultaneously.

An MTJ is a nanostructure device in which two ferromagnetic films/layers are separated by a thin oxide layer and allows current to tunnel depending on the tunnel magnetoresistance (TMR). (TMR) is the tendency of an MTJ to change the value of its electrical resistance in an externally applied field or spin polarized current. The field or current changes the magnetization of one of the ferromagnetic layers thereby changing the alignment of the magnetization of the ferromagnetic layers. The magnitude of the tunneling current depends on the relative orientation of the magnetization of both ferromagnetic films.

This effect is based on a couple of assumptions. First, is that there is electron spin conservation during the tunnelling process. Hence, electrons from one spin state in the first ferromagnetic layer are accepted by unfilled states of the same spin in the second ferromagnetic layer. Second, the tunneling current for a particular spin orientation is proportional in the first order to the product of the effective density-of-states of the two ferromagnetic films at the Fermi level. Third, the ground-state energy bands of ferromagnetic materials in the vicinity of the Fermi level are shifted in energy giving rise to separate majority and minority bands for electrons with opposite spins[47,48], and hence two partial currents (one for spin-up electrons and the other for spin-down electrons) in the

presence of an applied bias voltage. This is illustrated in Fig. 1a. Electrons tunnel in both directions with equal rates when no voltage is applied to the junction.

The TMR can be written as:

$$TMR = \frac{R_{AP} - R_P}{R_P}$$

where R_{AP} is the electrical resistance in the anti-parallel state, and R_P is the resistance in the parallel state. In terms of spin polarizations of the ferromagnetic film, the TMR can be written as:

$$TMR = \frac{2P_1P_2}{1 - P_1P_2}$$

where P_1 and P_2 are the spin polarizations, P, of the two ferromagnetic films given by,

$$P = \frac{\mathcal{D}_\uparrow(E_F) - \mathcal{D}_\downarrow(E_F)}{\mathcal{D}_\uparrow(E_F) + \mathcal{D}_\downarrow(E_F)}$$

$\mathcal{D}_\uparrow$ and $\mathcal{D}_\downarrow$ are the spin dependent density of states (DOS) at the Fermi energy (E_F) for the spin-up ↑ and spin-down ↓ states, respectively.

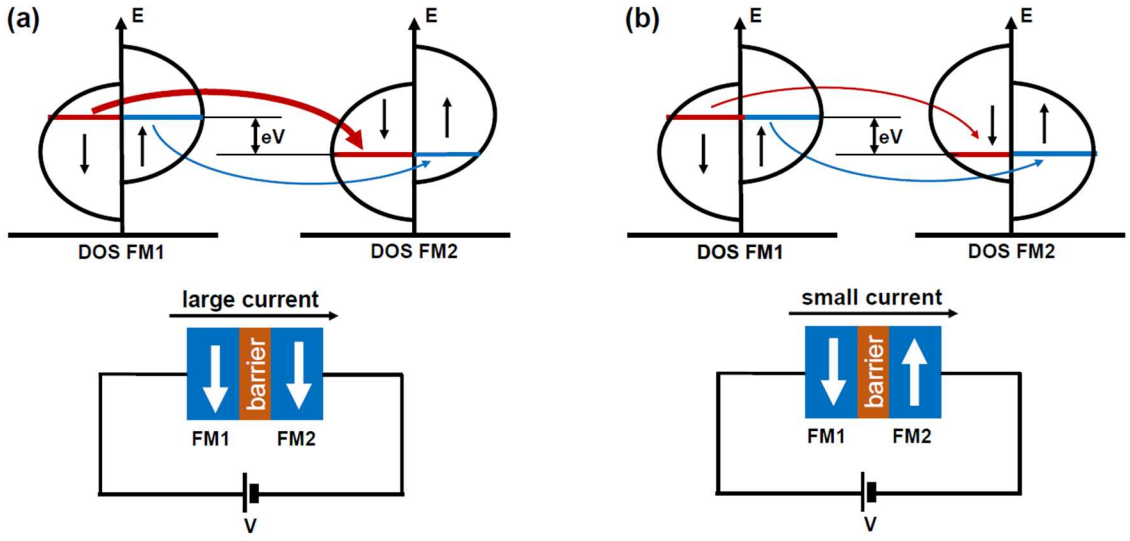

Figure 1.2: Band structure of parallel and antiparallel MTJ with applied voltage, V. (a) In the parallel configuration, majority electrons tunnel from the majority states in the left ferromagnet (FM1) to the majority spin states in the right ferromagnet (FM2) shown in red arrow while minority electrons tunnel from minority spin states in FM1 to minority spin states in FM2 shown in blue arrow. This configuration results in lower resistance, hence a high current. (b) In the antiparallel configuration, majority electrons tunnel from the majority states in FM1 to the minority spin states in FM2 (shown in red arrow), while minority electrons tunnel from minority spin states in FM1 to majority spin states in FM2 (shown in blue arrow). This results in higher tunneling resistance and a lower current.

1.4. THREE TERMINAL MAGNETIC TUNNEL JUNCTIONS (3T-MTJS)

The three-terminal magnetic tunnel junction (3T-MTJ) or domain wall MTJ (DW-MTJ) is an MTJ device where the free ferromagnetic layer is separated from the pinned ferromagnetic layer by a tunneling oxide barrier and there are three terminals: one terminal connecting to the top pinned electrode and two terminals on either side of the free ferromagnetic layer, or magnetic wire, as shown in Fig. 1b. The free layer can be set up to have two oppositely magnetized regions separated by a domain wall, and the free layer magnetization can be manipulated to orient either fully parallel, antiparallel, or inbetween,

relative to the magnetization of the pinned layer. The extra third terminal is to provide separate read/write control channels and separate control of the domain wall, compared to the two-terminal MTJs (2T-MTJs) in MRAM where the same channel is used as both read and write[49,50]. The domain wall of the free ferromagnetic layer can be displaced by spin transfer torque (STT) exerted on it by spin polarized current flowing through the ferromagnet (FM)[51] or by spin orbit torque (SOT) exerted by a charge current flowing through an underlying heavy metal (HM)[52–54]. The dynamics of STT is given by the Landau Lifshitz Gilbert equation:

$$\frac{d\hat{\boldsymbol{m}}}{dt} = -\gamma\left(\hat{\boldsymbol{m}} \times \boldsymbol{H}_{eff}\right) + \alpha\left(\hat{\boldsymbol{m}} \times \frac{d\hat{\boldsymbol{m}}}{dt}\right) + \frac{1}{qN_s}\left(\hat{\boldsymbol{m}} \times \boldsymbol{I}_s \times \hat{\boldsymbol{m}}\right),$$

where $\hat{\boldsymbol{m}}$ is the unit vector of the free layer magnetization; $\gamma = \frac{2\mu_B\mu_0}{\hbar}$ is the gyromagnetic ratio for the electron; α is the Gilbert's damping ratio; $\boldsymbol{H}_{eff}$ is the effective magnetic field; $N_s = \frac{M_s V}{\mu_B}$ is the number of spins in the free layer of volume V with M_s being the saturation magnetization and μ_B being the Bohr magneton; and $\boldsymbol{I}_s$ is the input spin current. More details about the dynamics to spin transfer torques (STT) and spin orbit torques (SOT) will be discussed in chapter 3.

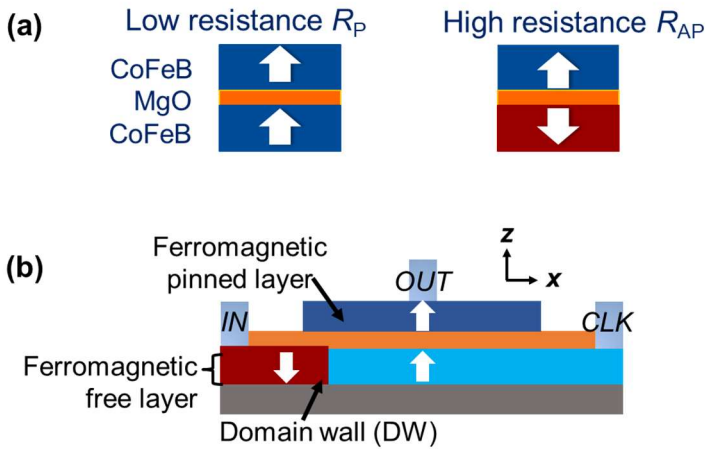

Figure 1.3: (a) shows the basic structure of an MTJ. The top and bottom CoFeB ferromagnetic layers are separated by the tunnel barrier, usually MgO shown in orange. When the magnetization (indicated by the white arrow) of the top and bottom layers are in the same direction, the MTJ device assumes a low resistance state R_P. However, when the magnetizations are in opposite directions as shown on the right, the MTJ device assumes a high resistance state R_{AP} (b) Cartoon of a side-view of the 3T-MTJ device. The up/down arrows and blue/red color represent the magnetization vector of the ferromagnetic thin films; the orange represents the tunnel barrier.

1.5. Applications to Neuromorphic Computing

There has been growing interest in the adoption of new computing paradigms, not just at the software level but at the hardware level [1], [2]. This is because most of the conventional infrastructures (especially data centers and supercomputing centers) that have been developed to handle the technological demands of Artificial Intelligence (AI) and Big Data (BD) still operate on the von Neumann architecture and are limited by speed and energy efficiency [3].

Dedicated architecture for artificial intelligence (AI) applications can overcome the limitations of the von Neumann architecture in accomplishing data-intensive tasks. Transistors are traditionally used as binary logic devices, whereas applications like

perception, prediction, and decision-making are inherently non-binary tasks. The von Neumann architecture also faces a memory access bottleneck, as separation between the memory unit and the computing unit necessitates the frequent transfer of data between these two units, which results in significant delay and energy consumption[55,56]. Due to these reasons, there has been a paradigm shift towards biologically-inspired neuromorphic computing which is the development of artificial neural networks that take the form of the brain. Neuromorphic computing has the potential to accomplish data-intensive tasks with orders of magnitude energy reduction compared to von Neumann architectures [57]. However, the implementation of this will require engineering devices and computing elements with functionalities that approximate the main physiological components of the brain, i.e. neurons and synapses, and embody dynamical operations such as learning and real-time adaptation (plasticity)[58].

Neurons are cells within the nervous system that receive signals from other neurons through their dendrites, perform non-linear processing on the signals in their soma, and transmit the output to the next set of neurons through their axon[59]. A synapse is a structure in the nervous system that allows a neuron to pass an electrical signal (electrical current) or a chemical signal (neurotransmitters) to another neuron or to a target effector cell[60]. Synaptic plasticity is believed to be a major contributor to memory and learning. In response to increases or decreases in specific patterns of a synapse's activity, the synapse strengthens or weakens over time. While plasticity is an ongoing topic of research in neuroscience, well-established hallmarks of plasticity operations include changes in the quantity of neurotransmitters, changes in the strength and number of receptors on the post-synaptic neuron, and changes in how rapidly the post-synaptic neuron responds to stimulation from the pre-synaptic neuron.

Spike-timing-dependent plasticity (STDP) has been identified as a key operation for learning and memory in the brain, as well as the basis for development and refinement of neuronal circuits during brain development. It is a biological process in which the strength of the synapse (synaptic weight) is correlated with the time differences between pre-synaptic neural spikes and post-synaptic neural spikes[61,62]. This is commonly refered to as “cells that fire together, wire together,”[63] in which the synaptic connection between the neurons gets reinforced in the form of Long-Term Potentiation (LTP) or weakened in the form of Long-Term Depression (LTD).

Numerous types of emerging non-volatile memory devices are being studied as artifical neurons for low-power computing elements and synapses as adaptive memory elements[64]. So far, most research in this area has focused on technologies such as resistive random access memory (RRAM)[65,66], phase change memory (PCM)[64,67], and conductive-bridge RAM (CBRAM)[68]. For example, complex plasticity effects have been physically demonstrated in CBRAM devices[69,70] and used for nanodevice-powered learning architectures[71,72].

Magnetic tunnel junctions have recently gained the main stage as candidates for neuromorphic computing building blocks due to their low switching energy, high endurance compared to other resistive memory devices for data-intensive tasks [73], complex behaviors that can be mapped onto the neuromorphic system [74], back-end-of-the-line compatibility for high density applications, and leveraging of close-to-market magnetic random access memory (MRAM) [75].

Moreover, there has been significant interest in fully implementing plasticity operations in magnetic random access memory (MRAM) systems based on magnetic tunnel junction (MTJ) devices. This is because magnetic devices have many properties similar to the neurons and synapses of the brain, such as low-energy[76] and stochastic switching[77],

nonvolatility, and co-localized memory and logic[78]. Additionally, magnetic devices have been proposed to act as both synapses and neurons[79–82], providing a potential platform for monolithic neuromorphic circuits.

Some progress has been made on emulating the neuron and the synapse using magnetic devices [83,84]. In particular, it has been shown that three-terminal magnetic tunnel junctions (3T-MTJs) are well suited for neurons and synapses [85,86], where the third terminal allows manipulation of a domain wall (DW) using spin orbit or spin transfer torque. Increasingly more accurate mimics to the brain are being developed with the 3T-MTJ like the Leaky-Integrate-Fire (LIF)[82] neuron which also shows lateral inhibition, and a 3T-MTJ synapse model which shows spike timing dependent plasticity (STDP) [87,88] and has been predicted to find applications in online training of neural networks. However, more work has to be done in showing and using these components and models in online machine learning tasks.

1.6. OUTLINE OF THE DISSERTATION

This dissertation presents experiment computational and experimental studies on magnetic structures for future logic and computation applications. Here I give an outline of the main focus of subsequent chapters.

In chapter 2, I discuss my work on synthesizing novel 2D chromium carbide Cr_2C MXene material that has been predicted to have magnetic properties. Here, I discuss my synthesis methods and various characterizations that were made. This work was made with the hopes that the probable magnetic properties of Cr_2C will pave the way for more energy efficient MTJs with lower dimensional requirements and faster switching speeds.

In chapter 3, I discuss my computational work at simulating the domain wall dynamics for a scaled ferromagnetic wire in application in a multiply and add circuit

architecture. I also summarize my work on experimental setups to characterize the ferromagnetic switching of MTJs. This involves writing codes to observe field switching of the soft ferromagnetic layers of prefabricated MTJ devices and observing the hysteresis curves and TMRs of such devices.

In chapter 4, I discuss my contributions to computational micromagnetic modeling of neuronal behaviors with MTJs and my primary published work on developing a biological synapse model with the MTJ. Further, I present preliminary data on the behavior of the circuit if I have a 2 X 2 synaptic array. In addition, I discuss my ongoing work at expanding this synaptic array model developed in designing a full-scale spiking neural network synaptic array for machine learning purposes. This work is intended to be further applied to neuromorphic computing hardware development in the future.

Finally, chapter 5 summarizes the work done in this dissertation and proposes the possible directions for future research work.

Chapter 2: Synthesis and Characterization of Cr2C MXene nanosheets.[1]

2.1. INTRODUCTION

Here I discuss my work on synthesizing Cr2C which is a 2D transition metal carbide also known as MXene. This work is currently under review in the Journal of Materials Research (JMR) as an invited paper for the 2020 Materials Research Society (MRS) Spring/Fall Meeting. Hence, I will be taking excerpts from the manuscript for use in this chapter.

There are three main methods seen in literature for deriving MXenes from the corresponding MAX phase: the use of hydrofluoric (HF) acid, the use of a fluoride salt and an acid, or the use of ammonium bifluoride[89,90]. In this experiment, fluoride salts and hydrochloric acid were used as the etchant due to the high yield and milder nature of the acid on the resulting reaction compared to the use of HF[37,89,90]. Also, it is considered to be a safer method when compared to direct handling of HF[89,90].

Here, a chemical exfoliation process to reduce the Cr_2AlC MAX phase into Cr_2C MXene was developed. To achieve optimal etching results, we varied the fluoride salt used, the reaction environment temperature, the concentration of the reactants, and the after-etch extraction procedure (including speed of centrifugation, method of product separation, and delamination technique), as described subsequently. We discuss how changing these different parameters affect the characteization results, including scanning electron microscopy (SEM) images, electron dispersive x-ray spectroscopy (EDX), x-ray

[1]The results, discussions and figures presented in this section have been adapted with permission from the following reference under review as at the time of writing this dissertation: O. Akinola, I. Chakraborty, H. Celio, D. Akinwande, & J. A. C. Incorvia. Synthesis and Characterization of Cr_2C MXenes. *Journal of Materials Research* (2021). The dissertator, O.G. Akinola designed conceived and designed the experiment, carried out the etch, performed most of the measurements, analyzed most of the data, and largely wrote the manuscript with contributions from all the authors.

diffraction (XRD), and x-ray photoelectron spectroscopy (XPS) measurements done both on the bulk and exfoliated samples. We also identify the Raman signature and the transmission electron microscopy (TEM) structure of the synthesized Cr_2C. The results show that the best exfoliation, i.e. highest yield, lowest byproduct, fastest etch time, and largest area sheets, was acheived using a modified MILD (mMILD) method with sodium fluoride (NaF) salt and hydrochloric acid (HCl) in a 9 °C environment.

An additional section is also presented where I discuss initial attempts to separate the synthesized MXene into individual sheets by using mechanical tape exfoliation. I also discuss preliminary magnetic measurements using superconducting quantum interference device (SQUID) mangnetometry. Results gotten from the tape exfoliation and magnetic measurements are inconclusive and further work needs to be done to get better data.

2.2. SYNTHESIS APPROACH

The chemical reaction equation to derive Cr_2C from Cr_2AlC using HCl and a fluoride salt is given as follows:

$$2Cr_2AlC\ (s) + 6XF\ (s) + 6HCl\ (l) \xrightarrow{yields} 2Cr_2C(s) + 2AlF_3\ (aq) + 6XCl + 3H_2\ (g)$$

where X is a cationic element like Na or Li; (s), (l), (aq), and (g) imply the materials are in solid, liquid, aqueous, and gaseous states, respectively.

Etch Procedures

Using two fluoride salts

We carried out two separate reactions to compare using Lithium Fluoride (LiF) and Sodium Fluoride (NaF). In two separate beakers, 3 ml of 12 M concentrated Hydrochloric Acid (HCl, J.T. Baker, 37% CMOS grade) was added to 3 ml of DI water to dilute. Then, 0.919 g of LiF (Alfa Aesar, 98.5%) was added to one of the beakers, whereas 1.521 g of

NaF (Alfa Aesar, 99%) was added to the other beaker. The two beakers were shaken vigorously for a minute or two to ensure that the fluoride salts dissolve optimally in the acid. Afterwards, 1.728 g of ball-milled Chromium Aluminum Carbide (Cr_2AlC, ACI Alloys, purity > 99.9%) with average grain size of 1 mm was gradually added to each of the beakers containing the acid-salt solution. On addition of the Cr_2AlC, the reaction heats up showing exothermicity, there is a release of Hydrogen gas molecules, and the mixture turns dark green as expected.

The reaction sat at room temperature and samples were collected from the reaction after 48 hours, 72 hours, and 96 hours. These samples were washed through 5 cycles using distilled water and centrifuged at a speed of 3,500 rpm for 10 mins per cycle. After each cycle, the solute mix was decanted off and fresh distilled water was added for the next cycle.

Varying the temperature of the reaction environment

To determine the effect of reaction temperature, we put two beakers, one containing HCl + NaF + Cr_2AlC and the other containing HCl + LiF + Cr_2AlC, in a heating bath at 50 °C. Another two beakers each with NaF or LiF were put in a cold environment at 9 °C. The reaction sat for 96 hours and sampled every 24 hours. Cleaning procedures were carried out as described above.

Varying reactant concentration using the mMILD method.

To observe the effect of varying the reactant concentration, we used a modified minimally intensive layer delamination (mMILD) method[91]. This involved slightly increasing the concentration of the acid and the fluoride salt to release more cations for intercalation and delamination. In two separate beakers, 3 ml of DI water was added to 3 ml of HCl to dilute. Then, 0.783 g of LiF was added to one of the beakers while 1.268 g of

NaF was added to the other beaker. The two beakers were shaken vigorously for a minute or two to dissolve the fluoride salts in the acid. Afterwards, 0.576 g of Cr_2AlC was gradually added to each of the beakers containing the acid-salt solution.

Achieving better separation and delamination after etching reaction

For better etch quality, the reaction products were first washed in up to 50 ml of HCl before going on to wash with DI water. Washing the etch product in HCl helps to precipitate the remaining fluoride salts and other salt byproducts while the MXene product remains dispersed in acid. The MXene-acid colloid was then decanted into a separate beaker diluted in water and centrifuged to extract the MXene which had settled to the bottom of the centrifuge tube. Afterwards, the supernatant was decanted and the MXene mass was washed several times in DI water until a pH of about 7. In addition, the samples were centrifuged at 2000 rpm for 15 minutes rather than 3500 rpm for 10 minutes that was earlier used.

We also tested the effect of delamination with Tetrabutylammonium hydroxide (TBAOH). After washing the etch reaction in DI water until a satisfactory pH is achieved, 12.5 ml of TBAOH was added to 1 g of the etched MXene and made to mix on a rotator for 4 hours. After, the products are washed in DI water until a pH of about 7.

2.3. CHARACTERIZATION TECHNIQUES

After the supernatant from the reaction had reached pH of between 6 and 7, the samples were drop-casted on a 1 cm^2 silicon chip and dried on a hotplate at about 500 °C. The physical structure of the samples was observed using scanning electron microscopy (SEM, Zeiss Neon 40) with 5 kV beam voltage and the in-lens secondary electron detector.

Initial elemental analysis was carried out using the Bruker electron dispersive x-ray spectrometer (EDX) attached to the SEM. For further elemental analysis, some of the dried MXene samples were put on a graphite tape and Kratos X-ray Photoelectron Spectrometer was used to analyze the elements present in the sample. After sputtering the surface for 30 seconds to remove surface impurities, surveys and region scans were made for Cr, O, Al, and C using a step size of 0.05 eV for 580 steps with a dwell time of 1.5 s and a characteristic energy of 1486.6 eV. Further data analysis was carried out with Casa XPS software to identify the regions and components for the various binding energies.

Powder X-ray diffraction (XRD) analysis was carried out on dried samples using a Scintag X1 Theta-Theta Diffractometer and a Rigaku R-Axis Spider Diffractometer, both with monochromatic Cu Kα X-ray sources (wavelength 1.54 Å).

Raman analysis was performed on the optimized-etched Cr_2C MXene using a Witec Micro-Raman Spectrometer Alpha 300 with an Ar laser (wavelength 514 nm). Scanning transmission electron microscopy (STEM) was performed for a closer look into the structure of the etched MXene product, using a JEOL NEOARM.

2.4. KEY RESULTS AND DISCUSSION

2.4.1. Physical Morphology

Figures 2 (a) and (b) show the physical structure of the unetched Cr_2AlC under SEM. Using LiF and HCl as etchant at room temperature after 72 hours of etch, the Cr_2C MXene sheets began to become visible as the Cr_2AlC bulk blocklike structure began to transform into an accordion structure as though a book is drenched in water, taken out, and dried. This structure is shown in Figs. 2.1 (c) and (d). After 96 hours the MXene was fully etched, shown in Figs. 2.1 (e) and (f) where example stacks of MXene sheets are surrounded by byproducts.

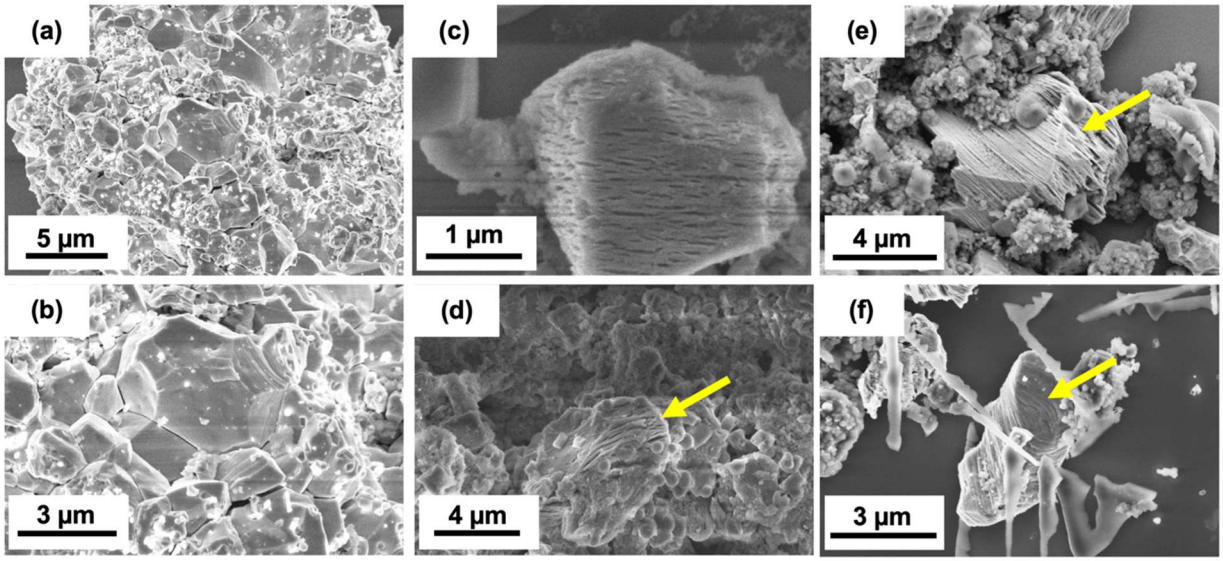

Figure 2.1: Etch process over time. SEM images of (a), (b) unetched Cr_2AlC MAX phase. (c), (d) Cr_2C MXenes after 72 hours of etching, and (e), (f) Cr_2C MXenes after 96 hours of etching, all in a mixture of LiF and HCl. The accordion-shaped structure signifies that the inter-MXene Aluminum layer has been etched off by the fluoride salt and hydrochloric acid mixture. (c) shows how the structure looks midway through the etch. Arrows indicate example Cr_2C sheets.

The etch results were further improved, to achieve higher yield, lower byproduct, and shorter etch time, by using the mMILD technique, a cold environment of 9 °C, and using NaF + HCl as the etchant, with results shown in Fig. 2.2. The mMILD technique used was an adaptation of the MILD method that has proven successful for etching titanium-based MXenes, where the concentration of the fluoride salt and acid is increased and sonication is decreased[42,89–94]. Here, the concentration of the fluoride salt and acid was kept lower than in the original MILD method, since too high a concentration damaged the MXene sheets.

When the reaction temperature was swept between 9 °C, room temperature, and 50 °C, we found the optimized etch time was 45 hours, 96 hours, and 120 hours, respectively. Since the reaction is exothermic, reducing the temperature drives the reaction in the forward direction quicker. The benefit of cold temperature is contrary to what has been observed in other works, where better etch results were reported at higher temperatures[95–98], since the increased temperature increases the solubility of the fluoride salts, liberating more of the fluoride ions to take part in the reaction while the cations can take part in the intercalation. Here, since the mMILD method already provided high molar concentrations of the fluoride salts, the higher temperature was not needed, and the low temperature helped to drive the reaction forward.

Figure 2.2 compares the use of LiF and NaF. In Fig. 2.2(a), LiF is used as the etchant, which produces accordion structures, but with fluorine residue visible as a fuzzy surface on the crystals, confirmed by EDX. We expect less residue using NaF, since NaF solubility is 4.13 g/L compared to LiF solubility of 1.34 g/L[99]. Hence, at the end of the reaction there will be four times less undissolved NaF in the solution.

Figures 2.2(b-d) show the results using NaF. Figure 2.2(b) shows an example of a clean, low-residue accordion structure achieved with this optimized method, looking like pages of a book. This structure gives proof of successful reduction of the MAX phase Cr_2AlC to Cr_2C MXene sheets. Figure 2.2(c) shows a larger area with many accordion structures visible, showing the high yield. Figure 2.2(d) highlights the yellow box area to show an example structure in more detail. Washing the etch product in HCl before washing in DI water further helped reduce residual salts and byproducts in the etch product mix.

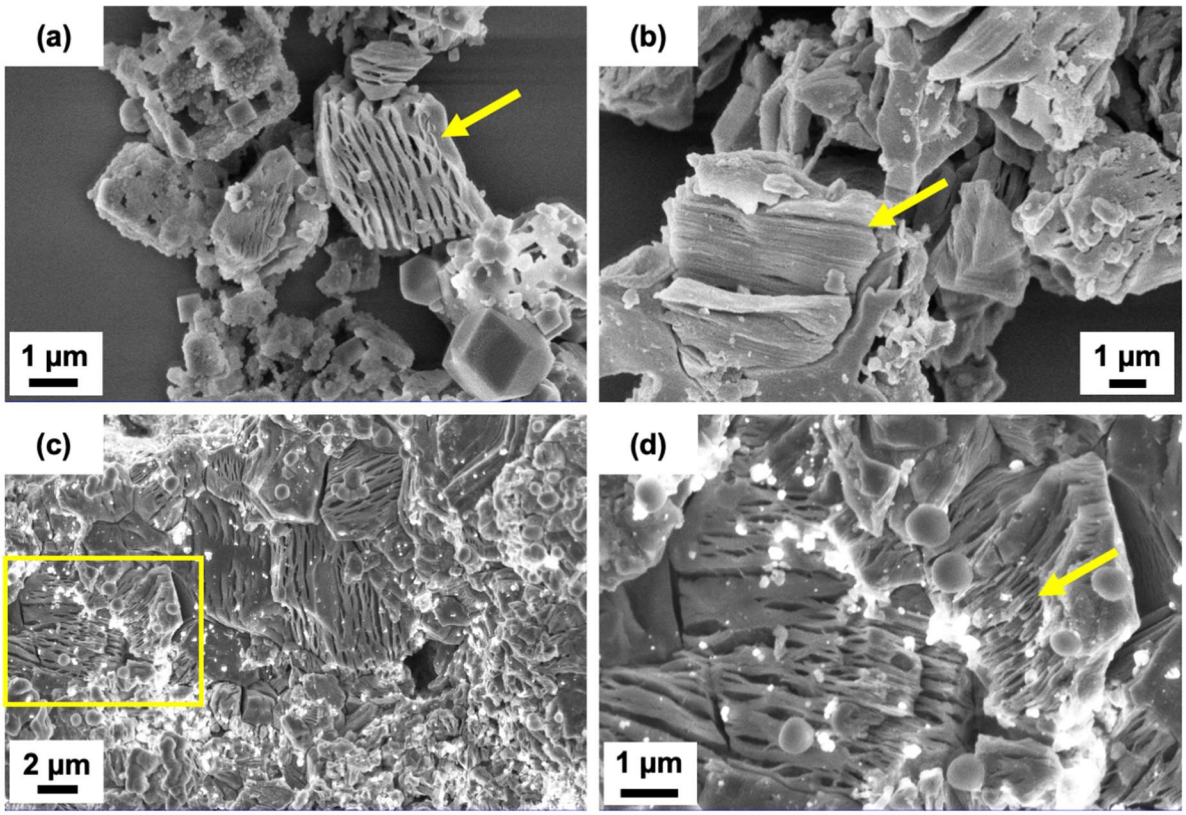

Figure 2.2: Optimized etch conditions comparing etchants. All images show the etch product after 45 hours of etching in 9 °C environment using the mMILD method. (a) Using LiF etchant. (b) Using NaF etchant. (c) Larger area using NaF etchant, with yellow box area shown in (d). Arrows indicate example Cr_2C sheets.

In Fig. 2.3, the process was further optimized to increase delamination, increase yield, and reduce byproduct. Tetrabutylammonium hydroxide (TBAOH) was used to attempt to further delaminate the sheets[89,91,92,100–102], but as can be seen in Fig. 2.3(a), it introduced more organic impurities into the mix. These organics adhered to the dangling bonds left as the result of the etch, visible as smears of amorphous material on the MXene products. Figure 2.3(b) shows the effect of not using TBAOH at all. The cation in the fluoride salt is sufficient for intercalation and delamination of the MXene sheets.

Washing to a pH of about 7 ensures that most of the salt has been removed and that the cations are well intercalated in-between the MXene sheets. Sonicating the reaction for an hour at the beginning of the etching reaction helps in mixing the reactants and further aids in the intercalation process. It should also be noted that the choice of the centrifuging speed plays a role in preserving the integrity of the MXene sheets. We noticed that using a 2000 rpm rather than a 3500 rpm centrifuging speed helped to produce better quality products.

Figures 2.3(c-d) show example SEM images with improved delamination, high yield, and low byproduct wherein sonication was added in the first hour of the etch to promote delamination, and the reaction product was washed in HCl before washing with DI water. Because salts have lower solubility in lower pH conditions, this helped precipitate the excess unreacted fluoride salts and salt byproducts in the solution, leading to lower byproduct for both salts. The images show better sheet-like structures compared to (b).

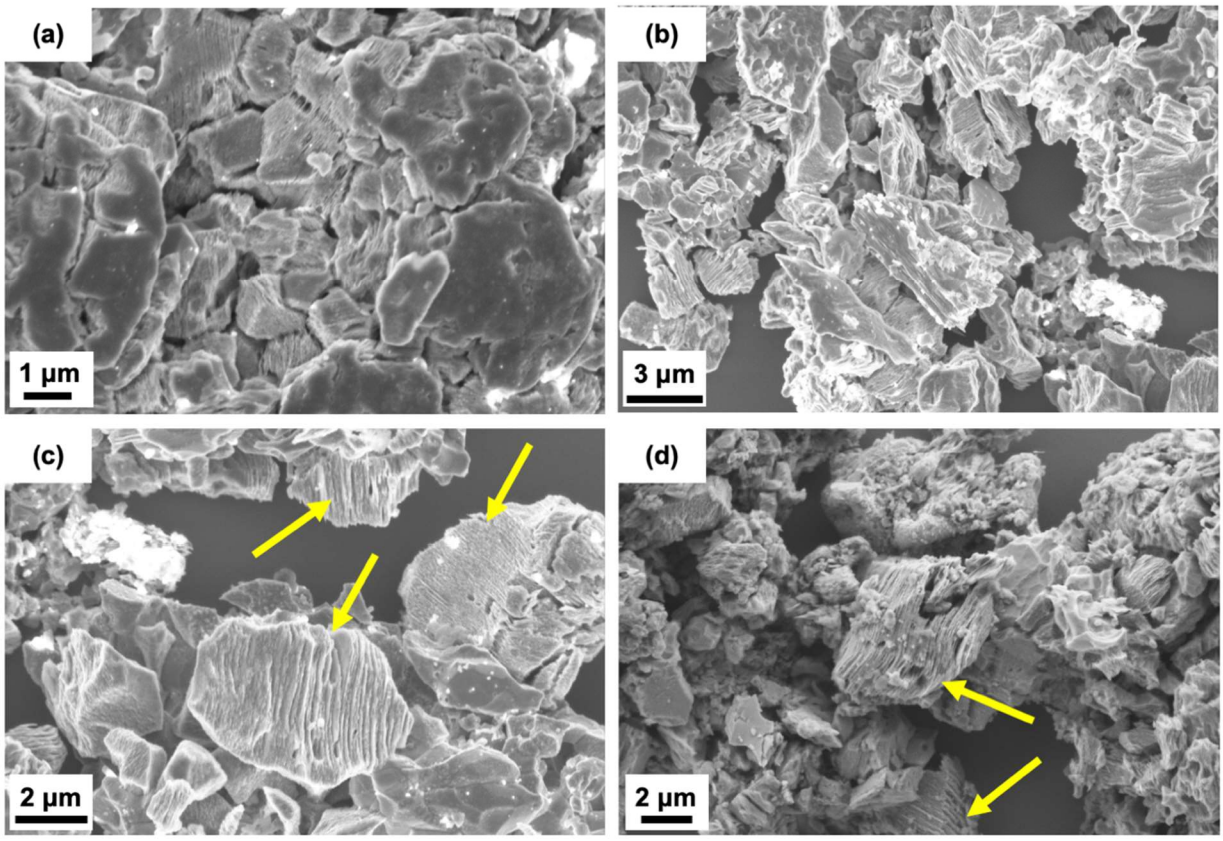

Figure 2.3: Optimized etch conditions using NaF etchant. (a) SEM image of the etch products after using TBAOH, showing increased amorphous material on the surfaces. (b) Etch product without using any TBAOH. (c) Etch product when sonication and HCl wash steps are added, which show improved delamination and yield and reduced byproduct, using the in-lens detector and (d) using secondary electron detector.

2.4.2. Chemical Analysis

Figure 2.4 shows the initial elemental analysis using EDX for (a-b) unetched Cr_2AlC, (c-d) LiF-etched Cr_2C MXene, and (e-f) NaF-etched Cr_2C MXene. The Al counts are lower for the etched products vis-à-vis the Cr counts, as compared to that of the unetched material, indicating the Al has been significantly removed. There are also more significant fluorine counts for the LiF-etched Cr_2C MXene in Fig. 2.4(d) when compared

to the NaF-etched counterpart in Fig. 2.4(f), corroborating the SEM images that show amorphous fluorine on the MXene surface using the LiF etchant. This is an indication that etching with NaF salt gives a cleaner etch result. Since the Cr Lα and the O Kα energies are very close, a more accurate method is required for the elemental analysis.

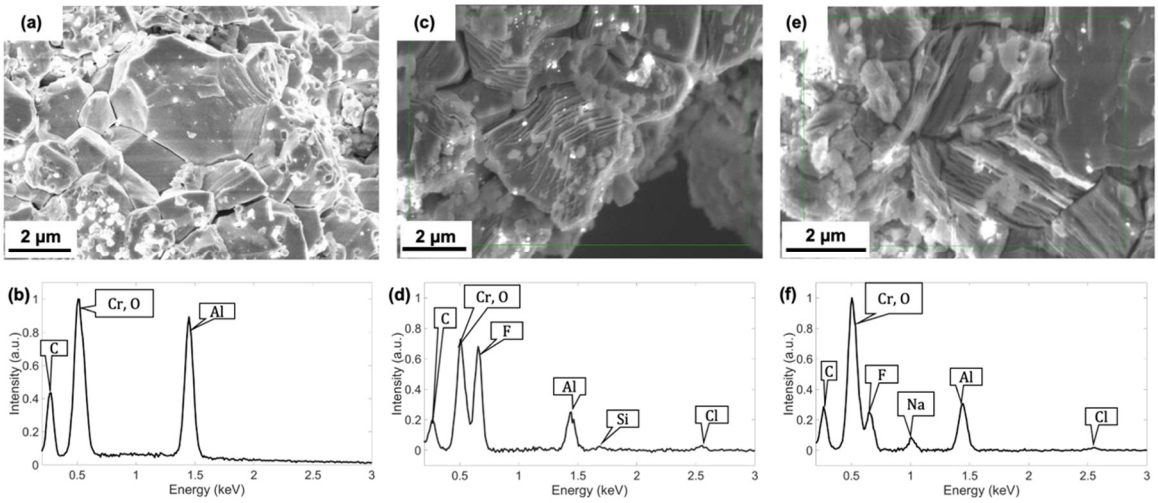

Figure 2.4: EDX analysis. SEM images of (a) unetched Cr2AlC MAX phase, (c) Cr2C MXene after etching in LiF and HCl for 45 hours, and (e) Cr2C MXene after etching in NaF and HCl for 45 hours, with corresponding EDX plots in (b), (d), and (f), respectively.

XPS was carried out on the dried MXene samples to analyze the elements present before and after etching and identify the regions and components of the various binding energies. Before measurement, the sample was sputtered for 30 seconds to remove surface impurities.

Figure 2.5 shows the XPS signal intensity vs. binding energy before and after the optimized etching for the energy regions of (a) Cr, (b) Al, (c) O, and (d) C. The XPS data shows the etch product has reduced Al and that new binding energies are visible for Cr and C, confirming formation of Cr_2C. In Fig. 2.5(a), Cr 2p shows up as a doublet Cr 2p1/2 and

Cr 2p3/2. After etching, the Cr signal is stronger, indicating some looseness between the layers as a result of stripping off the interlayer Al atoms making more surface Cr atoms available. In Fig. 2.5(b), after etching the intensities for the Al 2s region peaks reduced considerably and shifted. This signifies that the bulk of the Al component of the Cr_2AlC was removed and some of the remaining Al formed new compounds as shown in the supplementary Fig S3. In Fig. 2.5(c), after etching the O 1s peaks did not change significantly in intensity but did slightly shift to higher binding energies also signifying the formation of new oxides.

In Fig. 2.5(d), after etching the intensities of the C 1s peaks increased and shifted, showing that new compounds of carbon were formed in the etching process. The C 1s etched data is further analyzed in Fig. 2.5(e). As shown by the orange, light green, and blue traces, a major contributor to the intense C peak is adventitious carbon with the C – C bond, the C – O bond group, and the C = O bond group at binding energies 284.67 eV, 285.85 eV, and 288. 02, respectively. These are labeled with **C**, **B**, and **A**, respectively. This is expected because breaking off the Al bonds in the Cr_2AlC created more dangling bonds on the Cr for the adventitious C and CO group to latch onto. Also, the creation of Cr_2C nanosheets creates more exposed surface area for new surface chemistry. The peak **D** at 282.88 eV is expected to correspond to that of Cr_2C, while peak **E** at 281.86 eV is characteristic of Cr_7C_3 [103,104].

The Cr XPS signal from Fig. 2.5(a) is further analyzed in Fig. 2.5(f). The binding energy peaks are identified to the nearest 0.2 eV as Cr_7C_3 at 574.18 eV (peak **C**) and 583.38 eV. The peak **B** is conjectured to be a mix of Cr_2C and CrC at 575.23 eV repeating itself at 584.43 eV, while the peak **A** at 575.63 eV is thought to be CrC also repeating at 584.83 eV[103,105–112]. It should be noted that that the peak for CrC shows up more intensely similar to our XRD analysis data. Further work needs to be done to separate out the Cr_2C

and CrC etch products. Additional analysis of the XPS regions and components are included in supplementary information.

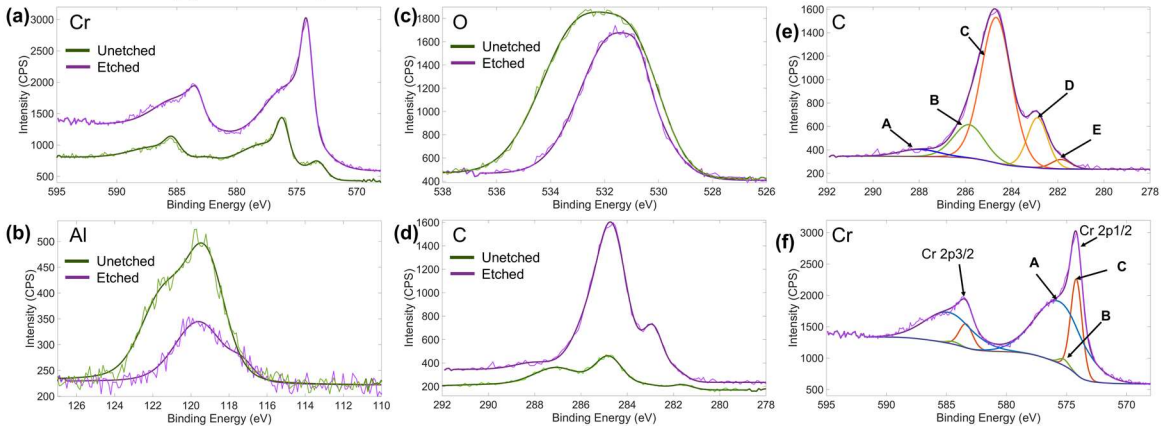

Figure 2.5. X-ray photoelectron spectroscopy of the unetched Cr_2AlC MAX phase (green trace) compared to optimized etched Cr_2C MXene (purple trace). The data are overlayed with an envelope function. (a) Energy region for Cr 3/2p and Cr 1/2p doublets. (b) Energy region for Al 2s. The Al 2p lines are very close to the Cr 3s lines, so the Al 2s lines were observed. (c) Energy region for O 1s. (d) Energy region for C 1s. (e) XPS measurement plots for the C 1s region overlayed with the envelope function (purple trace) and showing different components of Cr_7C_3, Cr_2C/CrC, the C – C adventitious carbon, the C – O bond group, and the C = O bond group, as marked by **E**, **D**, **C**, **B**, **A,** respectively. (f) XPS measurement plots for the Cr 2p region overlayed with the envelope function (purple trace) and showing different components of Cr 2p1/2 and Cr 2p3/2 doublets. The binding energy peaks indicative of Cr_7C_3, Cr_2C and CrC are indicated by **C**, **B**, and **A**, respectively.

Further analysis of the regions and components for Al 2s, Cr 2p, O 1s and C 1s are shown in Figs 2.6, Fig 2.7, and Table 2.1 below.

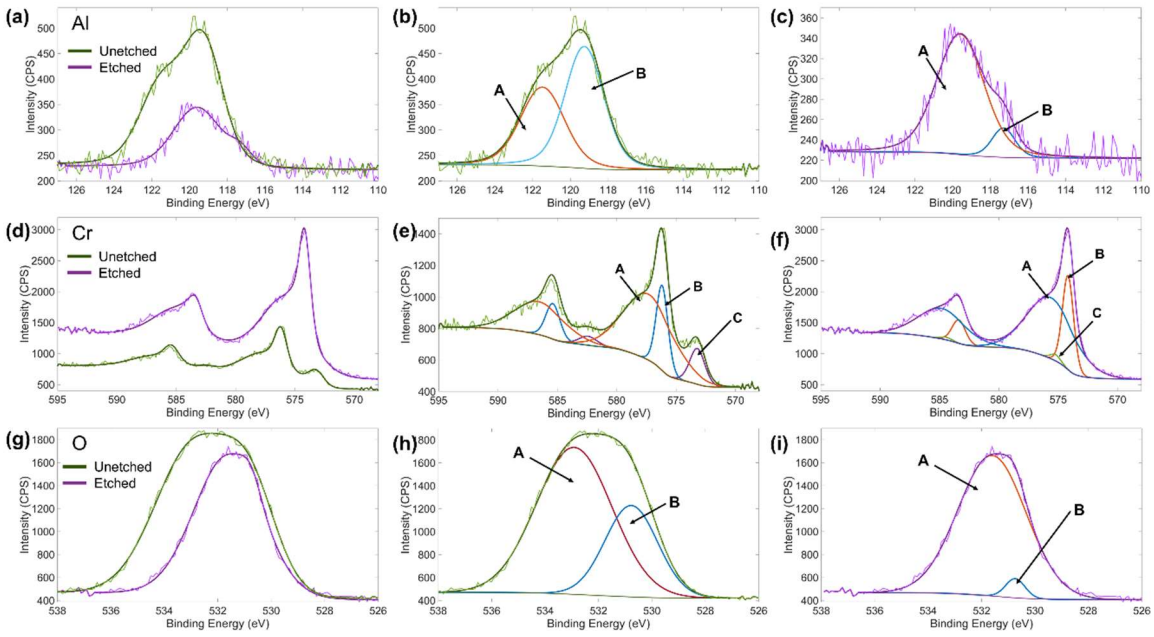

Figure 2.6: X-ray photoelectron spectroscopy of the unetched Cr_2AlC MAX phase (green trace) compared to optimized etched Cr_2C MXene (purple trace). The data are overlayed with an envelope function. (a) Energy region for Al 2s. The Al 2p lines are very close to the Cr 3s lines, so the Al 2s lines were observed. (b) Show Al 2s components before the etch and (c) show the components of Al 2s after etch. The peaks labelled **A** and **B** both shifted showing the formation of new compounds. More importantly is that the significant reduction of their counts especially **B**. (d) Energy region for Cr 3/2p and Cr 1/2p doublets. (e) Plots for the Cr 2p region before the etch and (f) after the etch. The rearrangement of the peak positions shows that there are new compounds being formed. (g) Energy region for O 1s. (h) region and components for O 1s before etching and (i) after etching. Notice how the component labeled **A** remained stable even after the plot. This shows the component from atmospheric contamination.

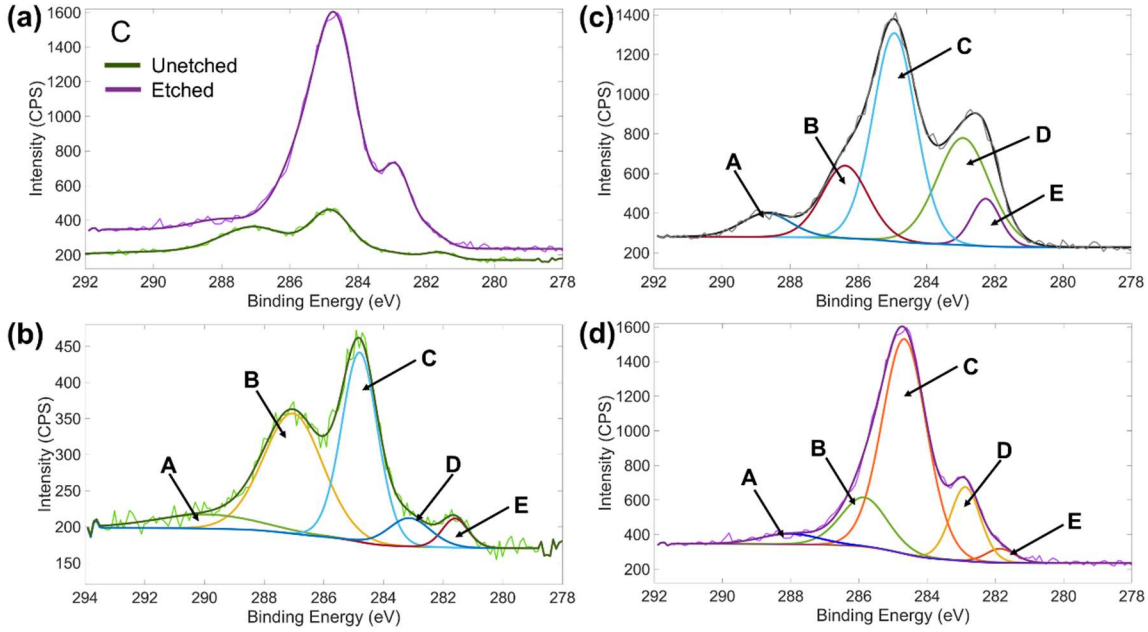

Figure 2.7: X-ray photoelectron spectroscopy of the unetched Cr_2AlC MAX phase (green trace) compared to optimized etched Cr_2C MXene (purple trace). The data are overlayed with an envelope function. (a) Energy region for C 1s. (b) Components for the C 1s region before the etch. (c) Components for the C 1s region after etching. (d) Components for the C 1s region after etching and after 30 s of Argon sputtering to remove some of the surface adventitious carbon. This is shown by the reduction in the C = O bond group, the C – O bond group and the C – C bond group labelled **A**, **B**, and **C** respectively and which make up adventitious carbon. The peak at **D** is identified as mix of Cr_2C and CrC while the peak at E is identified as Cr_7C_3.

		Before Etch			After Etch				
Element	Name	Position (eV)	FWHM	Area	Position (eV)	FWHM	Area	Label	Phase
Cr	Cr 2p	586.51	4.93	1116.73	584.83	4.65	2479.7		
	Cr 2p	585.38	1.4	341.55	584.43	1.2	54.39		
	Cr 2p	582.41	1.8	110.63	583.38	1.33	548.39		
	Cr 2p	577.31	4.93	2233.46	575.63	4.65	4959.3	**A**	CrC
	Cr 2p	576.18	1.17	683.1	575.23	1	108.78	**B**	Cr_2C
	Cr 2p	573.21	1.5	368.76	574.18	1.11	1828	**C**	Cr_7C_3
Al	Al 2s	121.48	2.74	499.74	119.59	2.97	414.15	**A**	
	Al 2s	119.26	2.43	684.92	117.3	1.45	49.01	**B**	
C	C 1s	289.92	4.04	85.94	288.02	2	132.97	**A**	Cr_7C_3
	C 1s	287.04	2.35	425.5	285.85	1.6	495.2	**B**	Cr_2C
	C 1s	284.8	1.42	405.55	284.67	1.54	2077.4	**C**	C - C
	C 1s	283.13	1.66	70.73	282.88	1.04	481.32	**D**	C - O
	C 1s	281.6	1.02	44.82	281.86	1	87.21	**E**	C = O
O	O 1s	532.91	3.34	4569.46	531.6	3	3921.5	**A**	
	O 1s	530.77	2.32	1978.67	530.74	0.86	153.65	**B**	

Table 2.1: Table shows the binding energy peak positions, area, and phase identifications for the different regions and components of Cr, Al, C and Oxygen labeled in Figures S3 and S4.

2.4.3. Phase Analysis.

Figure 2.8 shows powder XRD peaks for unetched and etched samples. Peaks for Cr_2C are marked by red crosses, Cr_2AlC by blue diamonds, Cr_7C_3 by gold triangles, and CrC by black circles. The diffraction peaks for the starting Cr_2AlC MAX phase material are shown by the black trace in Fig. 2.8(a). The peaks indicating Cr_2AlC are clear and distinct although there are a few Cr_7C_3 phases also showing up as well.

When the etch is done with NaF and HCl using the mMILD method at 9 °C, more Cr_2C phases at 27.86°, 37.44°, 40.61°, 74.96°, 81.25° and 82.70° appear as shown in Fig. 2.8(b) compared to other methods (see supplementary material)[113–116]. Also, the

intensities for Cr_2AlC and Cr_7C_3 reduced compared to the rest of the methods. The complementary appearance of prominent CrC phases in addition to this indicates that after 45 hours of etching most of the Al from the starting Cr_2AlC MAX phase has been etched out. See Supplementary Information for additional XRD analysis of sample degradation over a 2-year period.

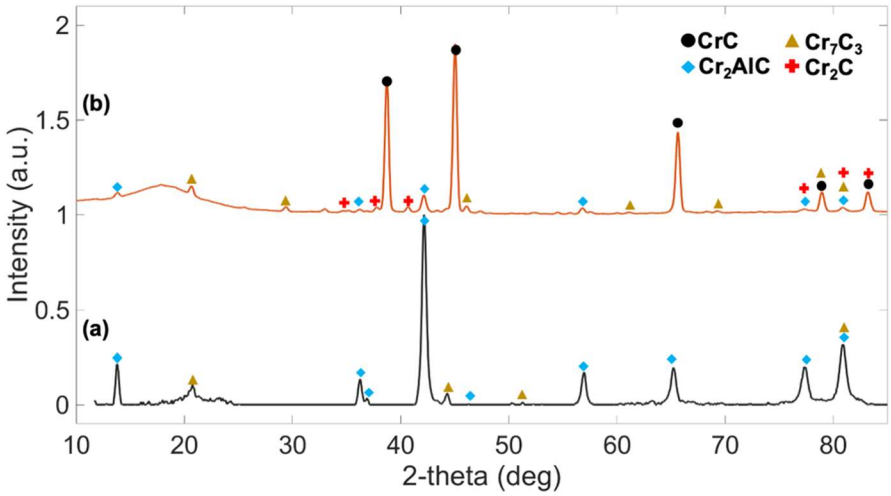

Figure 2.8: Powder x-ray diffraction (XRD) peaks for unetched and etched samples. Peaks for Cr_2C (red crosses), CrC (black circles), Cr_7C_3 (gold triangles), and Cr_2AlC (blue diamonds) are marked. (a) Black trace shows the scan of the starting Cr_2AlC MAX phase material showing distinct peaks for Cr_2AlC and some trace of Cr_7C_3. (b) Orange trace shows the result after etched with NaF and HCl at 9 °C for 45 hours using the mMILD method. More phases for Cr_2C are seen, as well as fewer impurities and fewer phases of Cr_2AlC and Cr_7C_3. Although intense peaks for CrC also show up, lower intensities of Cr_2AlC indicate that the etch is more successful.

The comparison of the other different combinations of parameters are shown in Fig 2.9. Powder x-ray diffraction (XRD) peaks for unetched and etched samples. Peaks for Cr_2C, Cr_2AlC, Cr_7C_3 and CrC are marked by red crosses, blue diamonds, gold triangles, and black circles respectively. In Fig 2.9(a), black trace shows the scan of the starting

Cr_2AlC MAX phase material showing distinct peaks for Cr_2AlC and some trace of Cr_7C_3. The purple trace in Fig 2.9(b) shows the result after etched with LiF and HCl at room temperature for 96 hours. Traces of Cr_2C begin to show up at 37.44° and 67.09°. The result after etched with NaF and HCl at room temperature for 96 hours is shown by the green trace in Fig 2.9 (c). While new phases of Cr_2C show up at 27.86° and 82.70°, there are many similar products showing up as well such as CrC shown in black circle markers and Cr_7C_3 shown in golden triangle markers. Figure 2.9 (d) shows the result in blue trace after etched with NaF and HCl at 9 °C for 45 hours. The orange trace in Fig 2.9(e) shows the result after etched with NaF and HCl at 9 °C for 45 hours and including the mMILD method. More phases for Cr_2C show up at 27.86°, 37.44°, 40.61°, 74.96°, 81.25° and 82.70°. There are fewer impurities and fewer phases of Cr_2AlC and Cr_7C_3. Although more intense peaks for CrC also show up compared to the method in 2.7 (d), lower intensities of Cr_2AlC indicate that the etch is more successful. In Fig 2.9 (f) Red trace shows the result after etched with LiF and HCl at 9 °C for 45 hours, and including the mMILD method, showing fewer Cr_2C and CrC peaks.

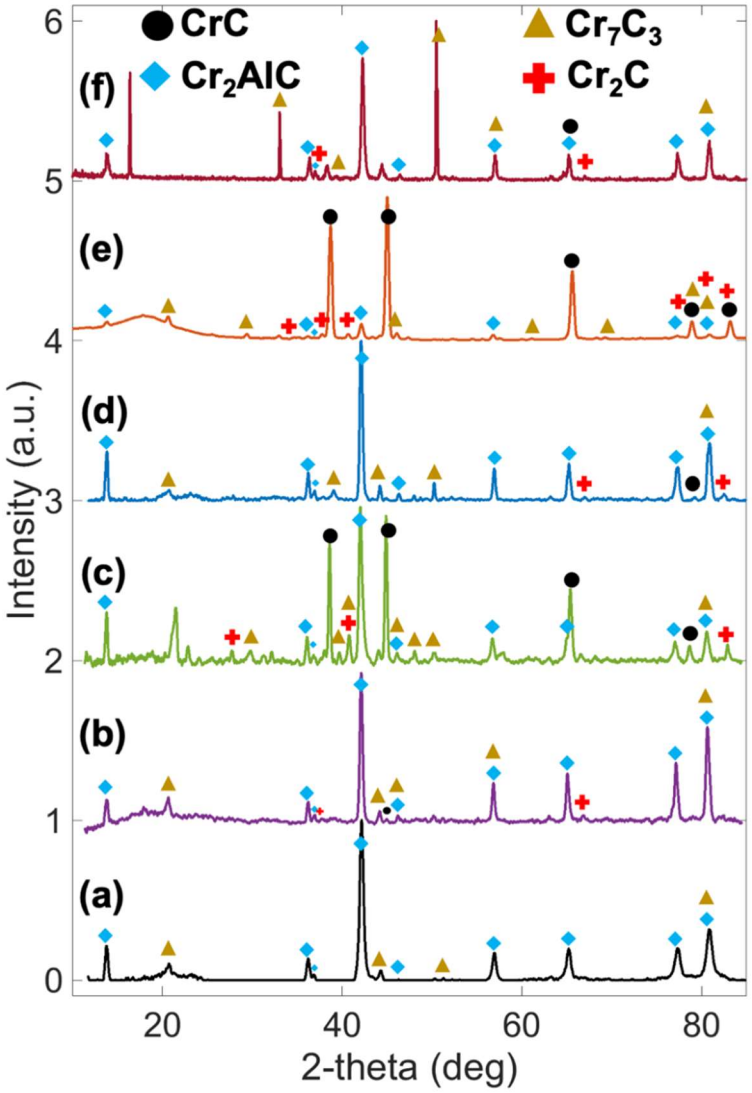

Figure 2.9. Powder x-ray diffraction (XRD) peaks for unetched and etched samples. Peaks for Cr_2C are marked by red crosses, Cr_2AlC by blue diamonds, Cr_7C_3 by gold triangles, and CrC by black circles. (a) Black trace shows the scan of the starting Cr_2AlC MAX phase material. (b) Purple trace shows the result after etched with LiF and HCl at room temperature for 96 hours. (c) Green trace shows the result after etched with NaF and HCl at room temperature for 96 hours. (d) Blue trace shows the result after etched with NaF and HCl at 9 °C for 45 hours. (e) Orange trace shows the result after etched with NaF and HCl at 9 °C for 45 hours and including the mMILD method. (f) Red trace shows the result after etched with LiF and HCl at 9 °C for 45 hours, and including the mMILD method, showing fewer Cr_2C and CrC peaks.

2.4.4. Additional Analysis and Discussions

Sample Degradation in Air over 2 Years

After a passage of time of about 2 years the diffraction analysis of the starting Cr_2AlC material shows that there is subtle degradation into Cr_7C_3 over time. This is shown in Fig. 2.10 where the diffraction pattern for the pristine Cr_2AlC material is plotted in black trace (a) and that of the degraded material is plotted in blue trace (b). The markers show that more phases of Cr_7C_3 show up in the material after a while. However, as shown in the orange trace in the plot (c), some Cr_2C phases tend to appear even when the degraded Cr_2AlC material is etched. This shows that the Cr_2AlC material is pretty stable as a starting material for the synthesis of Cr_2C.

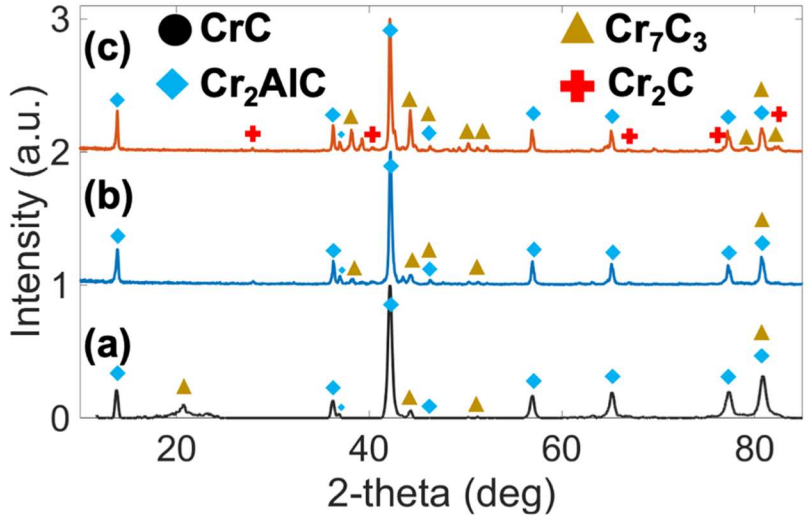

Figure 2.10: Powder x-ray diffraction (XRD) over time. (a) Unetched Cr_2AlC for freshly sintered material (black curve) compared to (b) the same unetched material after sitting in air for 2 years blue curve). (c) Etch products of (b) after 2 years.

Further Discussion of Temperature Effects

We note that the best etch result was gotten at a cold temperature of 9 °C, contrary to what was observed in other works where better etch results were reported at higher temperatures [95–98]. Since the reaction is exothermic, it is expected that reducing the temperature helps to drive the reaction quicker. Hence the reduction in time to 45 hours for the etch to be complete when done at 9 °C compared to the 96 hours required at room temperature, and 120 hours when doing in a hotter environment at 50 °C. A possible argument for increasing the reaction temperature could be that increasing the temperature increases the solubility of the fluoride salts, hence liberating more of the fluoride ions to take part in the reaction while the cations can take part in the intercalation.

Raman Analysis

Figure 2.11(a) shows the Raman spectra for the etched MXenes. The Raman modes show a D peak at 1327 cm^{-1}, a G peak at 1564 cm^{-1}, and a 2D peak at 2642 cm^{-1}. The peaks showing up are at 513.7 cm^{-1} and 962.2 cm^{-1} are believed to be characteristic of chromium carbides.

TEM Imaging

The acquired TEM images are shown in Fig. 2.11(b). The structures in (i) and (ii), as identified by the arrow, show striations indicating delaminated MXene sheets. In (iii) and (iv) the boundaries of different layers of the MXene sheets are visible.

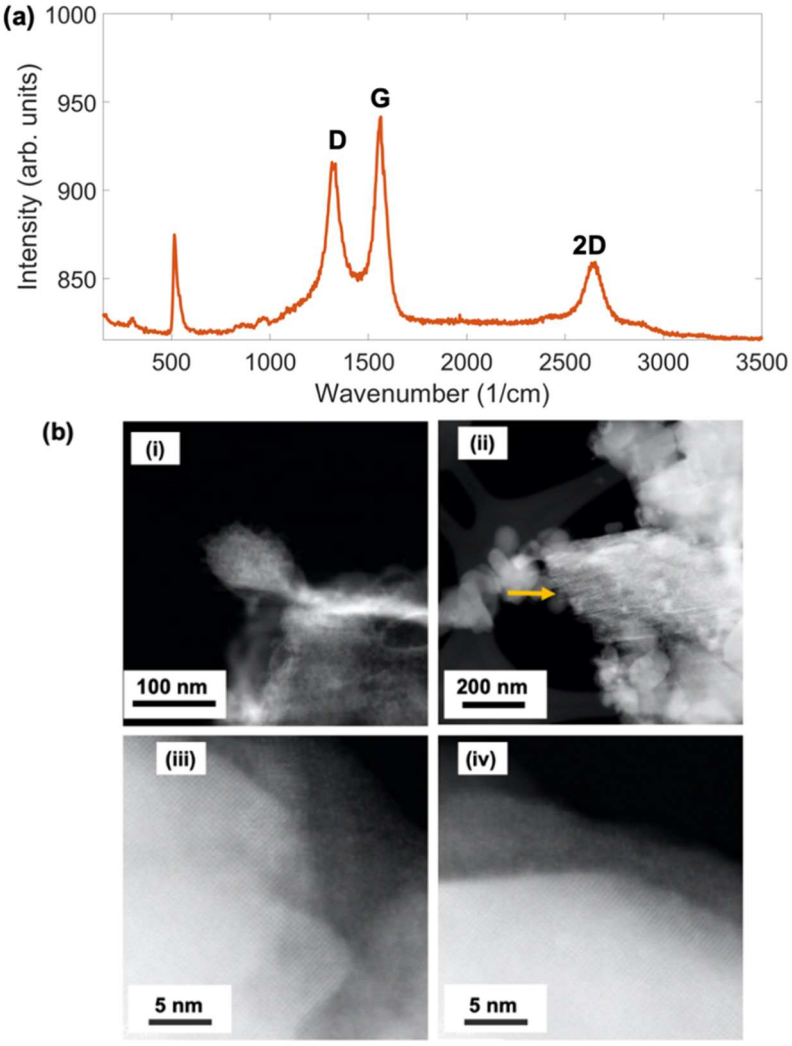

Figure 2.11: (a) Raman spectrum for the etched Cr_2C MXene. (b) STEM images for the etched Cr_2C MXene.

Magnetic Characterization

Figure 2.12 shows the results of the SQUID shows different zones labelled **A** to **D** ranging from paramagnetic to antiferromagnetic. Weak ferromagnetic-like signal shows up in region B likely coming from the larger Cr_2C flakes. However, at larger temperatures as shown in region **D**, the flakes are A-type antiferromagnetically stacked in the lowest energy configuration. A possible explanation for the paramagnetic signal showing up in regions **A**

and **C** is that the signals from the magnetic samples are so weak that they become dominated by the paramagnetic behavior of the other unetched components of the sample.

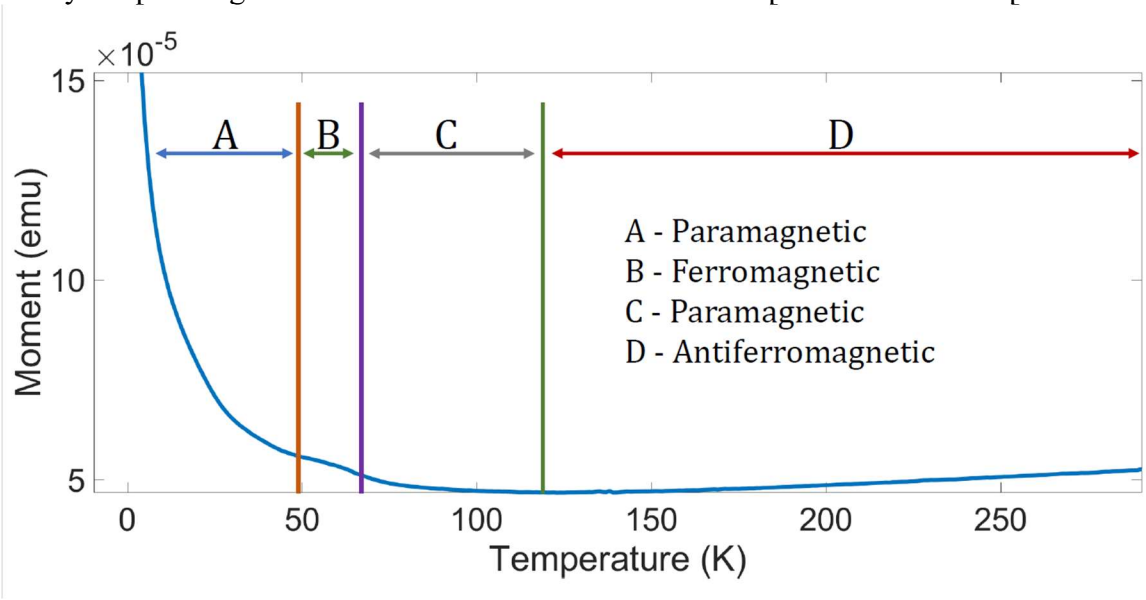

Figure 2.12 Superconducting quantum interference device (SQUID) magnetometry data for the synthesized Cr_2C.

Mechanical Tape Exfoliation

Some of the etched materials were dried in a rotating evaporator for 24 hours. And the side walls of the test tubes were scooped, and tape exfoliated to see if some nanosheets can be gotten. I observed what seems to be some folded sheets in the SEM. EDX scan shows that they were MXene products as shown in Fig 2.13. More work need to be done to ascertain this, get larger lateral dimensions and do some effective characterization of the chemical, morphological and magnetic properties.

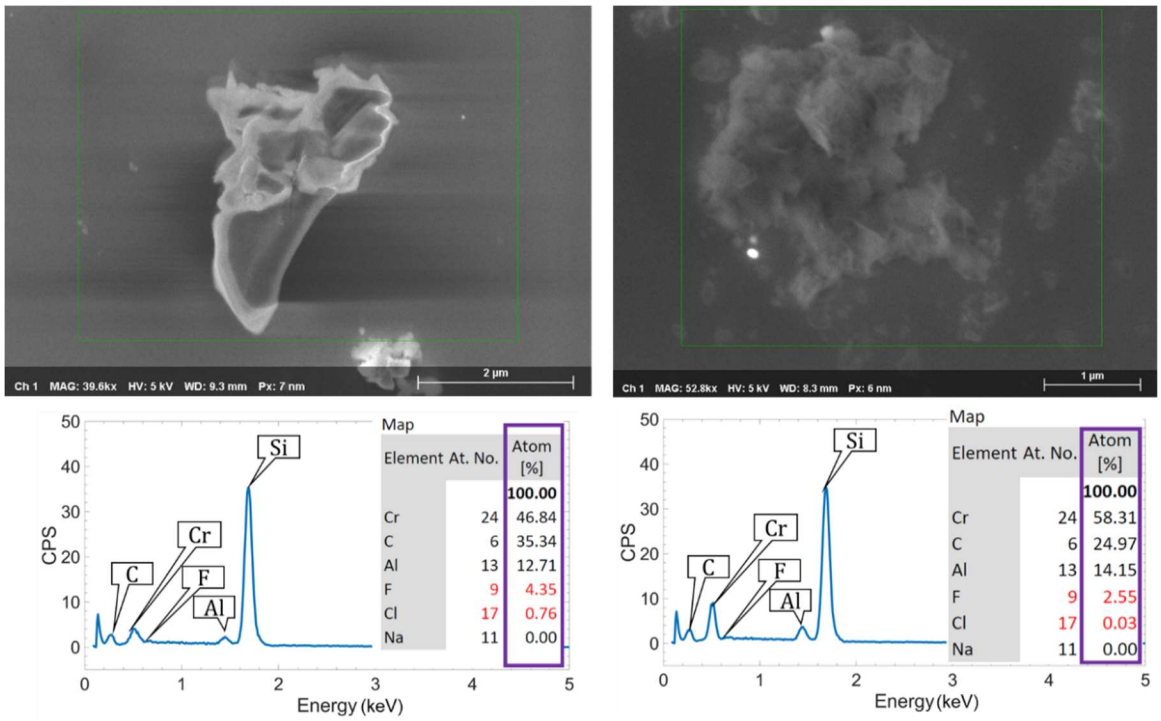

Figure 2.13 Scanning electron microscope images of exfoliated Cr_2C MXenes and the EDX data showing that the flakes are etched Cr_2C

2.5. CONCLUSION

While many MXenes have been theoretically predicted, the careful balance required in the exfoliation between breaking the inter-layer bonds without damaging the intra-layer bonds of the sheets has limited synthesis and experimental study. We have developed a chemical exfoliation process that derives Cr_2C MXenes from the parent Cr_2AlC MAX phase. Our results show that the best exfoliation, i.e. highest yield, lowest byproduct, fastest etch time, and largest area sheets, was acheived using our mMILD method with NaF salt and HCl in a 9 °C environment. In addition, sonicating for the first hour of the reaction and washing in an acid medium before washing in DI water up to a pH of 7 further helped the intercalation and delamination process. Having a proper choice of

centrifuging speed helps to preserve the quality of the flakes. A series of analysis including SEM, EDX, XPS and XRD confirm our findings.

The XRD and XPS data shows that a significant amount of CrC is being produced in addition to the intended Cr_2C MXene, showing further work needs to be done to separate the Cr_2C from CrC. Overall, these results open up Cr_2C to experimental study, including of its predicted emergent magnetic properties, and develop guidelines for synthesizing new MXene materials.

Chapter 3: Observing Spin Torque Dynamics: Simulation and Measurement

In this chapter I give a brief introduction into micromagnetics and report my work on using micromagnetic simulation software MuMax3 [117] to investigate the spin-orbit torque (SOT) behavior of a scaled MTJ. I also present how I have helped to design the code that is use for the electrical characterization of a fabricate MTJ device which shows great cycle-to-cycle variation in its SOT switching voltage.

3.1. A BRIEF INTRODUCTION TO MICROMAGNETICS

While atomic level theory focuses on the quantum mechanical ab initio calculations in the < 1 nm scale, and domain theory focuses on description of domain structures in the 1 – 1000 μm resolution, micromagnetic theory focuses on continuous description of magnetization in the 1 – 1000 nm length scale.

In Ferromagnetic materials exchange interaction causes electrons with overlapping wave functions to tend to align in the parallel direction. Assuming the nearest neighbor magnetic moments $\overrightarrow{\boldsymbol{m}}_i$ are almost parallel, i.e., $\overrightarrow{\boldsymbol{m}}_i \approx \overrightarrow{\boldsymbol{m}}_j$ for $\left|\vec{\boldsymbol{r}}_i - \vec{\boldsymbol{r}}_j\right| < \lambda$, where λ is the exchange interaction length, the discrete distribution of the magnetic moments can be approximated by a continuous vector density, $\overrightarrow{\boldsymbol{M}}(\vec{\boldsymbol{r}})$, having a constant norm.

The time derivative of unit magnetization $\overrightarrow{\boldsymbol{m}}(\vec{\boldsymbol{r}}, t)$ in a magnetic material produces a torque $\vec{\tau}$ given by:

$$\frac{\partial \overrightarrow{\boldsymbol{m}}}{\partial t} = \vec{\tau}$$

$\vec{m}$ is the reduced magnetization of unit length given by $\vec{m} = \vec{M}/M_s$ and M_s is the saturation magnetization of the material.

$$\vec{\tau} = \vec{\tau}_{LL} + \vec{\tau}_{ZL} + \vec{\tau}_{SL} \tag{1}$$

$\vec{\tau}_{LL}$ is the Landau – Lifshitz – Gilbert contribution to the torque given by:

$$\vec{\tau}_{LL} = -\gamma' \vec{m} \times \vec{B}_{eff} - \lambda \vec{m} \times (\vec{m} \times \vec{B}_{eff}) \tag{2}$$

The first part of the equation constitutes the precessional term due to an effective field while the second half of the equation is the phenomenological damping term. γ' is the precessional term written as $\gamma' = \frac{\gamma}{1+\gamma^2\eta^2 M_s^2}$; and λ is a phenomenological damping parameter given by $\lambda = \frac{\gamma^2 \eta}{1+\gamma^2\eta^2 M_s^2}$ but often replaced by $\lambda = \alpha \frac{\gamma}{M_s}$. γ is the gyromagnetic ratio, η is the damping parameter which is characteristic of the material, and α is a dimensionless constant called the damping factor which is a dimensionless constant.

$$\vec{B}_{eff} = \vec{B}_{ext} + \vec{B}_{demag} + \vec{B}_{ex} + \vec{B}_{anis} + \vec{B}_{dm} + \vec{B}_{th} \tag{3}$$

where $\vec{B}_{ext}$ is the externally applied field; $\vec{B}_{demag}$ is the demagnetization or magnetostatic field; $\vec{B}_{ex}$ is the effective field as a result of the Heisenberg exchange interaction given by $\vec{B}_{ex} = 2\frac{A_{ex}}{M_s}\Delta\vec{m}$ where A_{ex} is the exchange constant[118] ; $\vec{B}_{anis}$ is the effective field due to magneto-crystalline anisotropy and has contributions from both the uniaxial anisotropy and cubic anisotropy. The effective field due to uniaxial magneto-crystalline anisotropy given by $\vec{B}_{anis,u} = \frac{2K_{u1}}{B_{sat}}(\vec{u}\cdot\vec{m})\vec{u} + \frac{4K_{u2}}{B_{sat}}(\vec{u}\cdot\vec{m})^3\vec{u}$ where K_{u1} and K_{u2} are the first order and second order anisotropy constants respectively. The cubic anisotropy effective field

$\vec{\boldsymbol{B}}_{anis,c}$ can be looked up in ref materials[119]. $\vec{\boldsymbol{B}}_{dm}$ is the effective field due to induced Dzyaloshinkskii-Moriya interaction for thin films with out of plane symmetry breaking and is written as $\vec{\boldsymbol{B}}_{dm} = \frac{2D}{M_s}(\frac{\partial m_z}{\partial x}, \frac{\partial m_z}{\partial y}, -\frac{\partial m_x}{\partial x} - \frac{\partial m_y}{\partial y})$ [120,121]. $\vec{\boldsymbol{B}}_{th}$ is the fluctuating thermal field given by the approximation, $\vec{\boldsymbol{B}}_{th} = \vec{\eta}(step)\sqrt{\frac{2\mu_0 \alpha k_B T}{B_{sat}\gamma \Delta V \Delta t}}$ where α is the damping parameter, k_B is the Boltzmann constant, T is the temperature, B_{sat} is the saturation magnetization in Tesla, γ is the gyromagnetic ratio in radian per second per tesla, ΔV is the cell volume, Δt is the time step, and $\vec{\eta}(step)$ is the standard normal distribution changing values for every time step.

3.1.1. Spin Transfer Torque (STT)

$\vec{\tau}_{ZL}$ is the Zhang-Li spin-transfer torque that applies when current flows through spatial and time varying magnetization zones such as a domain wall[122]. It is given by:

$$\vec{\tau}_{ZL} = b_J(\vec{\boldsymbol{m}} \times (\vec{\boldsymbol{m}} \times (\vec{\boldsymbol{j}} \cdot \nabla)\vec{\boldsymbol{m}})) + c_J((\vec{\boldsymbol{m}} \times (\vec{\boldsymbol{j}} \cdot \nabla)\vec{\boldsymbol{m}}))$$

The first term on the right of the equation is the adiabatic torque while the second term constituted the nonadiabatic torque or field-like torque where

$$b_J = \frac{P\mu_B}{eM_s(1+\xi^2)};\ c_J = \frac{P\mu_B\xi}{eM_s(1+\xi^2)}$$

b_J and c_J have the units of velocity. b_J is the adiabatic term which describes the adiabatic process of nonequilibrium conduction electrons, while c_J is the nonadiabatic term that controls the terminal velocity of the domain wall and is related to the spatial mistracking of spins between the conduction electrons and local magnetization [122]. P is the spin current polarization of the ferromagnet, $\vec{\boldsymbol{j}}$ is the electron charge density, μ_B is the Bohr

magneton, e is the electron charge, ξ is the degree of non-adiabaticity, and M_s is the saturation magnetization. The critical switching current for spin transfer torque (STT) is reached when the energy gained by the spin transfer torque is overcome by the energy lost due to damping in each precession cycle [123]. Figure 3.1 shows a description of all the torques exerted on a magnetic moment.

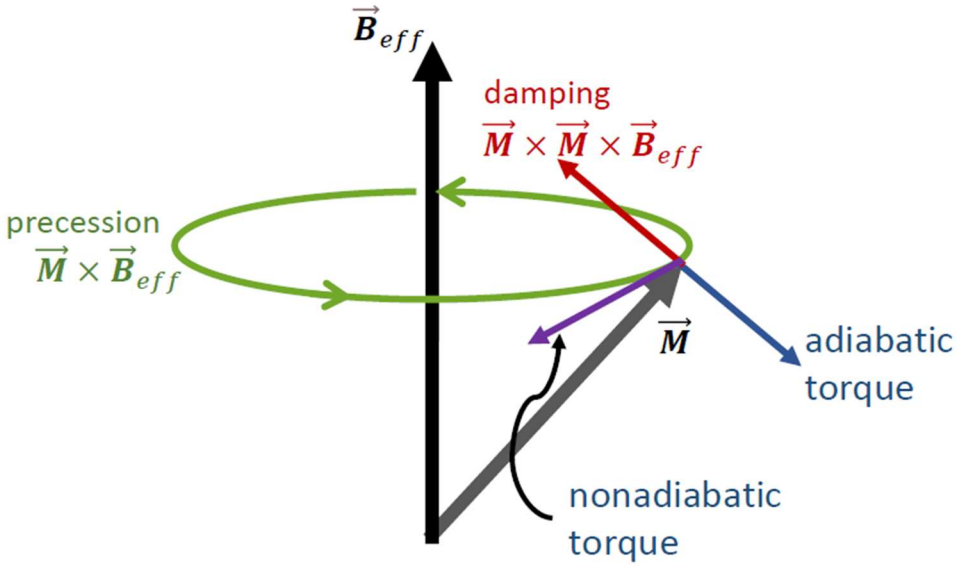

Figure 3.1: Illustrations of the precessional, damping, adiabatic and nonadiabatic components of the torque

$\vec{\tau}_{SL}$ is the Slonczewski spin transfer torque induced which acts when that acts upon the magnetization when a spin-polarized current flows through two ferromagnets separated by a spacer layer. This is particularly applicable to MTJs and it is given by:

$$\vec{\tau}_{SL} = \tau_{\parallel} \frac{\vec{m} \times (\vec{x} \times \vec{m})}{|\vec{x} \times \vec{m}|} + \tau_{\perp} \frac{(\vec{x} \times \vec{m})}{|\vec{x} \times \vec{m}|}$$

where

$$\tau_{\parallel} = \beta\frac{\epsilon - \alpha\epsilon'}{1+\alpha^2}; \tau_{\perp} = \beta\frac{\alpha\epsilon - \epsilon'}{1+\alpha^2};\ \beta = \frac{j_z\hbar}{M_s e d};\ \epsilon = \frac{P(\vec{\boldsymbol{r}},t)\Lambda^2}{(\Lambda^2+1)+(\Lambda^2-1)(\vec{\boldsymbol{x}}\cdot\vec{\boldsymbol{m}})}$$

j_z is the current density along the z axis, d is the free layer thickness, $\vec{\boldsymbol{x}}$ is the fixed layer magnetization, P is the spin polarization, Λ is the Slonczewski parameter used to characterize the spacer layer, and ϵ' is the secondary spin-torque parameter [124,125]. As with the Zhang-Li torque, the first term is the adiabatic torque and the second term is the non-adiabatic or field like torque. Figure 3.2 shows the mechanism of magnetization switching in an MTJ and domain wall motion in a ferromagnetic track using STT.

The STT induced magnetization switching however has a couple of shortcomings. The charge and spin channels overlap, the domain wall requires large current density to move it, and the time to initiate switching is unpredictable and large. Spin orbit torque induced magnetization switching overcomes some of these limitations because it separates the charge channel from the spin channel, and requires no incubation time to start switching [126,127]. In addition, the critical switching current density is an order of magnitude lower than that required for STT [126,127].

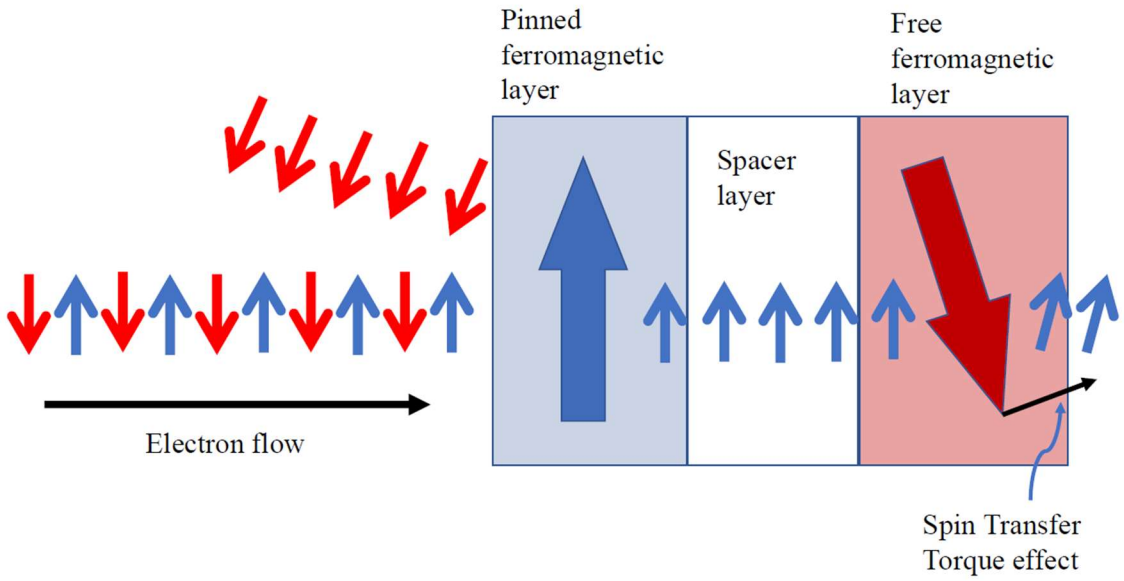

Figure 3.2: Illustration of Spin Transfer Torque (STT) mechanism in an MTJ. The small arrows show the electron spins with the blue showing spin up and the red showing spin down. The big blue and red arrows show the direction of magnetization for the ferromagnetic layers. The Pinned ferromagnetic layer reflects the spin down electrons and transmits the spin up electrons which then exert a torque on the magnetization of the free ferromagnetic layer. As so much electrons is required to switch this larger magnetization compared to the electron, the process is inefficient.

3.1.2. Spin Orbit Torque (SOT)

For heavy metals, spin-orbit interaction which is the relativistic interaction between a charge's spin and its orbital motion inside a potential (around the nucleus) becomes nonnegligible. This electromagnetic interplay between an electron's magnetic dipole, its orbital motion, and the electrostatic field of the positively charged nucleus is referred to as spin-orbit coupling [128,129]. And it leads to couple of effects including (a) magnetocrystalline anisotropy [130], (b) antisymmetric exchange also known as the

Dzyaloshinskii–Moriya interaction (DMI) [131–133], (c) magnetic damping [134], (d) anisotropic magnetorestistance [135,136], (e) anomalous Hall effect [137,138], (f) spin Hall effect [139–143], (g) Rashba effects (both the Bychkov-Rashba effect [144,145] and the Rashba-Edelstein effect) [146–148], and (h) Dresselhaus effect [149]. The effective magnetic field due to spin-orbit coupling can be written as $\vec{\boldsymbol{B}}_{SO}(\vec{k}) = \frac{1}{c^2}\left(\vec{\boldsymbol{v}} \times \vec{\boldsymbol{E}}\right)$ which can be added to equation 3 above.

Two of these effects are major contributors to the SOTs needed to induce magnetization switching in ferromagnetic structures and devices like the MTJ. First is the spin Hall effect (SHE) which occurs when spin-dependent scattering causes transverse spin imbalance of charge currents and hence spin accumulation at the lateral surfaces of the material.

The Rashba spin-orbit coupling occurs as a result of space inversion symmetry that is broken at surfaces and interfaces. The confinement of electrons at the surface give rise to a potential *V* that is normal to the surface and which leads to a magnetic field by Lorentz transformation in the rest frame of the electron. The interaction between this magnetic field and the electron's spin results in the spin-orbit Hamiltonian known as Rashba spin – orbit coupling [150].

As mentioned earlier, SOT has been shown to be more effective in switching of magnetization in MTJ devices [151].

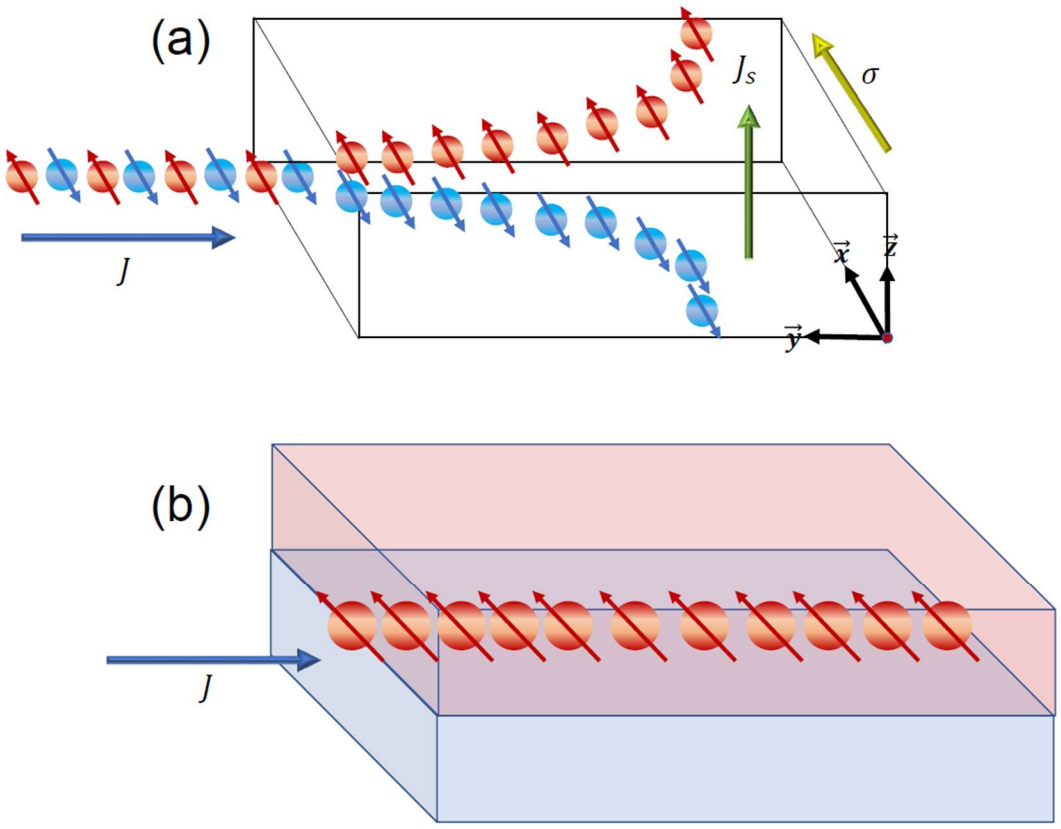

Figure 3.3: Illustration of Spin Orbit Torque components showing (a) Spin Hall Effect, and (b) Rashba Effect. J is the electron current, J_s is the spin polarized current, and σ is the spin polarization direction.

3.2. SIMULATION OF DOMAIN WALL DYNAMICS FOR EFFICIENT SWITCHING OF SCALED MTJS

Micromagnetic simulation software packages have been developed to observe the dynamics behavior of the magnetic moments and domain walls in ferromagnetic materials.

It is important to observe the domain wall dynamics of the ferromagnetic free layers of MTJs. The numbers obtained in these micromagnetic simulations can then be used as device parameters in circuit and register transfer level (RTL) simulations.

One of the architectures that has been identified to reap the immense benefit of memory and compute capability of an MTJ is a multiply and add accelerator architecture for matrix manipulation in machine learning tasks. This promises to employ the non-volatility of MTJs and the energy efficiency of a normally off MTJ circuit.

However, to ascertain that these benefits are indeed possible to achieve, it is important to observe some of the physics and obtain some important parameters through the micromagnetic simulation of the MTJ devices.

3.2.1. Device geometry and simulation methods

For this simulation, the ferromagnetic wire is chosen to be of the structure shown in figure 3.1 where t is the thickness of the ferromagnet along the $\hat{z}$ direction, w is the width along the $\hat{y}$ direction, l_T is the length of the ferromagnetic track along which the domain wall is free to move, l_P is the length of the pinned region of the ferromagnetic wire, DW_i is the initial position of the domain wall x_i distance from the median of the ferromagnetic track before a current *SET* pulse is applied and where it ends up after a *RESET* pulse is applied , DW_f is the final position of the domain wall x_f distance from the track median after a current *SET* pulse is applied.

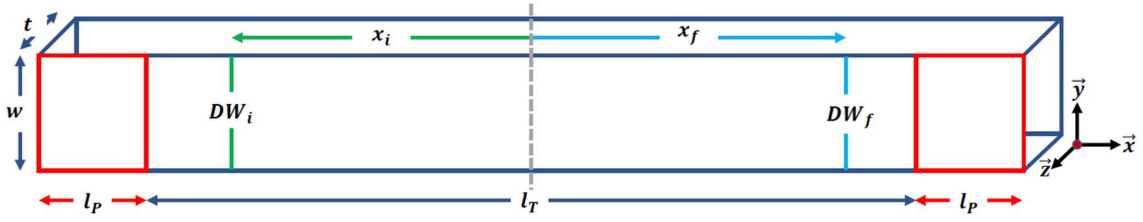

Figure 3.4: Geometry of the simulated ferromagnetic wire

The simulation was done assuming saturation magnetization $M_{sat} = 6.5 \times 10^5\ A/m^2$, first order uniaxial anisotropy constant $K_{u1} = 6.5 \times 10^5\ A/m^2$, interfacial

Dzyaloshinskii-Moriya strength $D_{ind} = -0.5 \times 10^{-3}\, J/m^2$, exchange stiffness $A_{ex} = 13 \times 10^{-1}\ A/m^2$, current polarization $P = 0.2$, Landau-Lifshtz damping constant $\alpha = 0.02$, non-adiabaticity of STT $\xi = 0.04$, and Slonczewski secondary STT term $\epsilon' = 0$. The ferromagnetic wire structure in Figure 3.1 was simulated with width $w = 15\, nm$, ferromagnetic wire thickness $t = 3\, nm$, and ferromagnetic domain wall track length $l_T = 100\, nm$. The width of the pinned region l_P was varied between $5\, nm$, $7\, nm$, $10\, nm$, $15\, nm$, and $20\, nm$. The domain wall was initialized at DW_i which is $40\, nm$ from the median of the wire. And the system was made to relax to find the optimal l_P that would give the most stable domain wall starting position DW_i.

The magnetization value m_z along the DW_i direction was used to track the domain wall position. Figure 3.5 shows the results gotten for the micromagnetic simulation of a perfect wire with no thermal effects and no random anisotropy effects included. The inset shows the simulation image with the orange region showing spin up and the green region showing spin down. The white region in the middle is the domain wall. At the start of the simulation time = 0ns, the domain wall tends to relax to about the same starting position for all the pinned region thickness considered. After allowing the system to run for 10 ns with zero applied current, the domain walls experience a force from the pinned regions that take them to the other end of the wire. Eventually as expected, the domain walls settle down at the middle of the wire. This is because the wire is perfectly symmetrical and there are no forces to pin the domain walls at either ends of the wire. It should also be noted that the force that the domain wall experience from either ends of the wire is proportional to the width of the pinned region l_P evident from the oscillations before the domain wall settles down.

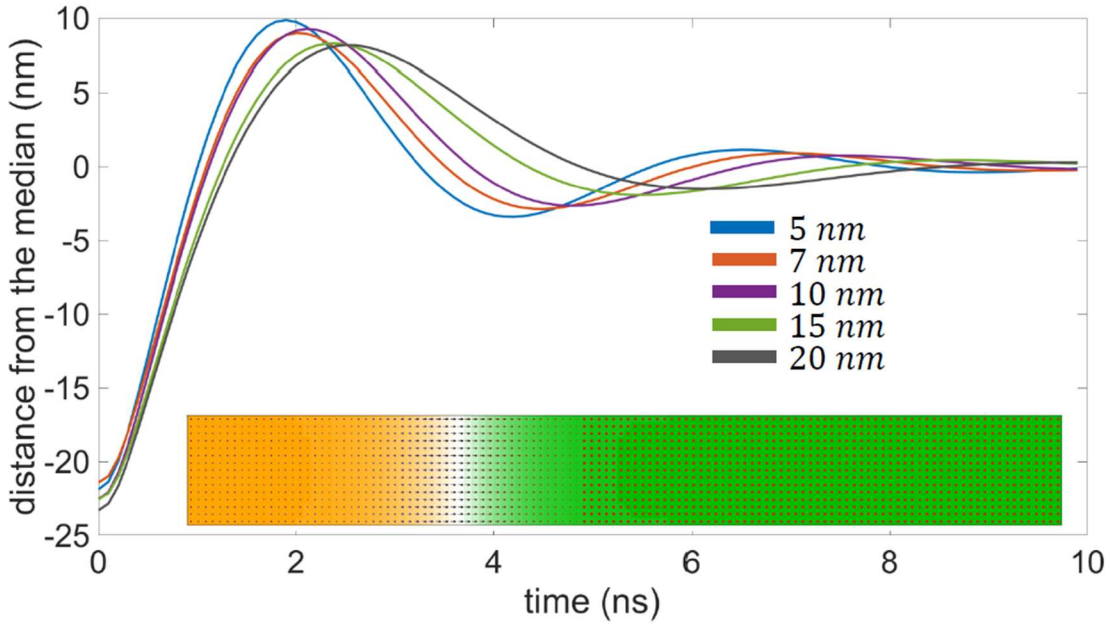

Figure 3.5: Simulation showing that the domain wall settles to the middle irrespective of the pinned region width.

Two methods can be used to pin down the domain wall on either side. First, it is expected that a real wire has random anisotropy effects due to lattice defects and surface roughness, among others. While this helps to pin down the domain wall along the length of the wire preventing it from allowing it to drift to the middle, the effect is quite indeterministic as it is hard to predict variations in lattice defects during wire growth. More work on this in our research shows that this is a probably more energy efficient route to go however more work needs to be done in controlling the intrinsic anisotropy effects of a ferromagnet in a deterministic manner. A more controlled way to pin the domain wall is the second method which is adding notches at each extremes of the wire.

Notches of size $1\ nm^2$ were created on one edge of the wire at DW_i with $x_i = -30\ nm$ and DW_f with $x_f = 30\ nm$ for the 7 nm pinned region width. 2 ns current pulses

were applied in a 5 ns period and the current density was swept from $1 \times 10^{10}\ A/m^2$ to $10 \times 10^{10}\ A/m^2$.

Figure 3.6 shows that wire configuration in fig 3.6(b), the current required to de-pin the domain wall is between $8 - 9 \times 10^{10}\ A/m^2$. While this current is sufficient to de-pin the domain wall, the notch on the other side does not provide enough force to hold it in place. Making the notch size on the right end of the wire twice deeper (structure shown in fig 3.6(c)) dampens the ricocheting force on the domain wall but was not sufficient to stop it as shown by the purple trace in fig 3.6(a). Putting a $2\ nm$ deep notch on both sides of the wire was able to pin the domain wall on the right side.

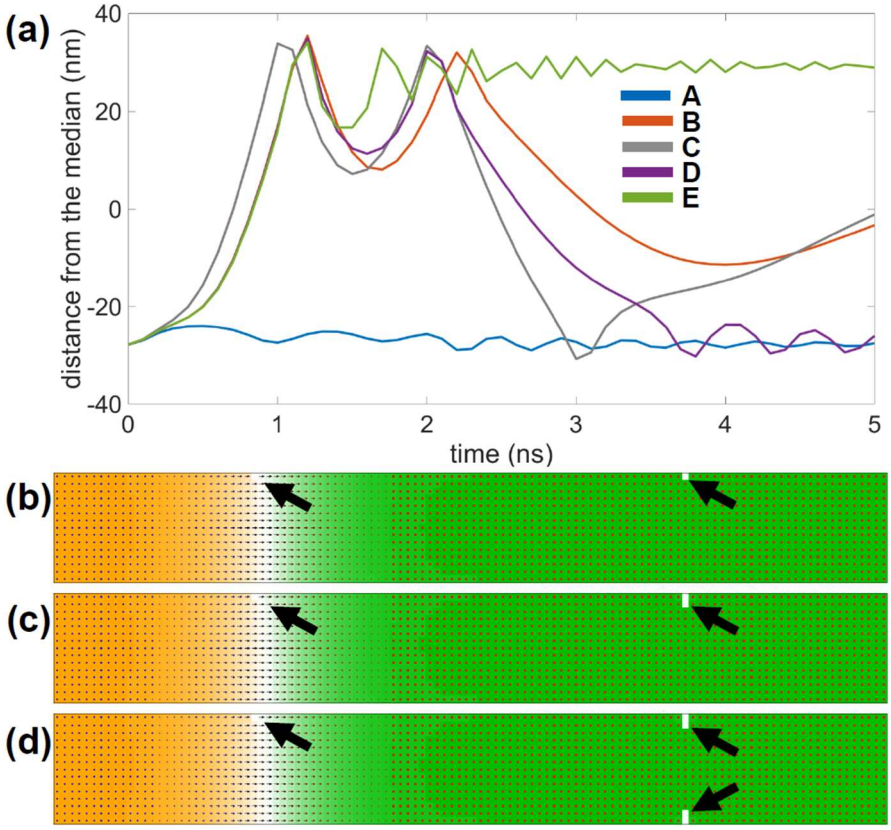

Figure 3.6: Simulation showing how putting notches affects the dynamics of the domain wall. (a) domain wall position with time when current density of **A**: $8 \times 10^{10}\ A/m^2$, **B**: $9 \times 10^{10}\ A/m^2$ and **C**: $10 \times 10^{10}\ A/m^2$ is applied to the geometry shown in (b), **D**: $9 \times 10^{10}\ A/m^2$ applied to the geometry shown in (c), **E**: $9 \times 10^{10}\ A/m^2$ applied to geometry shown in (d)

3.3. ELECTRICAL CHARACTERIZATION OF DOMAIN WALL MAGNETIC TUNNEL JUNCTIONS SPIN-ORBIT TORQUE DEVICES AND CIRCUITS FOR IN-MEMORY COMPUTING USE IT.[2]

3.3.1. Introduction

Magnetic tunnel junctions can be used not only as memory elements, but they can also be used in as computing devices making them excellent candidates for in-memory computing applications. However, they face a couple of challenges such as high current densities and low tunnel magnetoresistance when it comes to their experimental applications. This is despite several micromagnetic simulation works that have predicted superior performance of SOT induced switching in MTJs with perpendicular anisotropy. It is therefore important that careful fabrication and electrical testing techniques be developed to realize the excellent predictions from micromagnetic simulation studies.

In addition, tasks required of modern-day computers are so unstructured and data intensive such that memory access takes up to 96 % of their computing time [152,153] and SRAM idle leakage takes up over 20% or the total computation power [154]. The development of in-memory computing devices where same devices used in computing also serve as memory will help to lower this memory wall between processing and memory blocks on chips [155]. Not only do magnetic devices offer the benefit of non-volatility that

[2]The results, discussions and figures presented in this Chapter have been adapted with permission from the following reference [179] M. Alamdar, T. Leonard, C. Cui, B. P. Rimal, L. Xue, O. G. Akinola, T. Patrick Xiao, J. S. Friedman, C. H. Bennett, M. J. Marinella & J. A. C. Incorvia. Domain wall-magnetic tunnel junction spin–orbit torque devices and circuits for in-memory computing. Appl. Phys. Lett. 118, 112401 (2021). The dissertator, O.G. Akinola designed the instrumentation algorithm and wrote the LabView codes to automate the electrical measurement setup used to characterize the devices fabricated in this project.

reduces idle power, they also are radiation hard making them random bit flipping from solar flares and electromagnetic interference (EMI) [156].

There are three leading MTJ devices that can be used for in-memory computing applications based on their domain wall (DW) dynamics. These are the majority logic [157–159], the mLogic [160–164], and the three-terminal domain wall magnetic tunnel junctions (DW-MTJ) [78,165–168]. Of these three device types, the DW-MTJ is a leading candidate [169,170]. Several promising and exciting applications have been demonstrated for the DW-MTJ. Prototypes have shown how they can be used in circuit fanouts and concatenation [78]. Through simulation work we see how a single DW-MTJ device can perform a NAND function and cascaded into a one-bit adder [171]. This has been taken a step further by a recent work where a 32-bit adder were simulated entirely with DW-MTJ registers [168]. In addition, they have found application in neuromorphic computing circuits for artificial intelligence purposes [49,82,172,173],[174]. In this work, while I explain the experimental procedure and discuss some of the key results, I will focus more on the design of the measurement setup which is my main contribution to this project.

3.3.2. Experimental procedure

The studied DW-MTJ device is shown in Fig. 3.7(a). It consists of a heavy metal/ferromagnet/oxide trilayer, e.g. Ta/CoFeB/MgO, that is patterned into a DW track with an output MTJ centered on top of the track. The position of a DW in the DW track is moved by applying a Voltage V between the *IN* and *CLK* terminals. The DW position determines the centered MTJ resistance and therefore the output current from the *OUT* terminal to the next DW-MTJ device in the circuit[78,171]. The MTJ resistance $R_{MTJ} = R_P$ when the magnetic layers are parallel (P) and $R_{MTJ} = R_{AP}$ when antiparallel (AP). Oe_1 to Oe_2

is an Oersted field electrode used to nucleate the initial DW position entirely with current[175],[176].

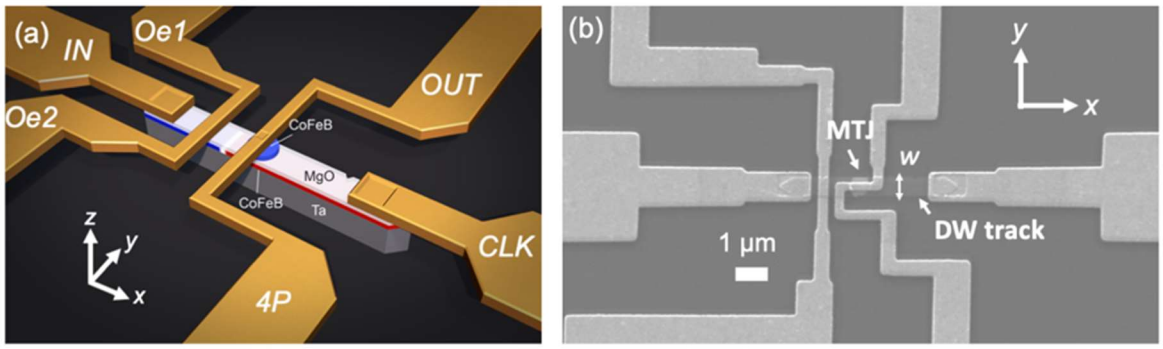

Figure 3.7: DW-MTJ device. (a) Schematic of the three-terminal DW-MTJ device with IN, CLK, and OUT terminals. The DW track is comprised of Ta (grey) / CoFeB (blue/red with white domain wall) / MgO (white), and the output MTJ is shown as a blue circle. Red and blue represent domains in ±z. Only essential layers are shown and not to scale. The 4P terminal is used to measure the four-point resistance of the MTJ; Oe1 to Oe2 is an Oersted field electrode. (b) Top-down scanning electron microscope image of w = 450 nm device prototype with patterned DW track and output MTJ labeled.

The MTJ stack was grown by Applied Materials in an Endura Clover^{TM} physical vapor deposition system[177] with layers Si(substrate) /SiO_2(100) /Ta(10) /CoFeB(1.2) /MgO(1) /CoFeB(1.9) /[Co/Pt](5) /Ru(0.9) /[Co/Pt](6.9) /Ta(1) /Ru(3); numbers are in nm and brackets represent multilayers [177]. The average film properties were measured to have a $TMR = 168 \pm 6\%$ and resistance-area product $RA = 35 \pm 2\ \Omega - \mu m^2$.

The film stack was patterned using electron beam lithography and ion beam etching. Example scanning electron microscope images of the devices are shown in Fig. 1b; DW track of widths w = 250, 350, and 450 nm were patterned with notches fabricated on each side of the track to keep the DW from exiting the device.

3.3.3. Measurement Setup

The block figure of the electrical instrumentation used for the characterization of the devices is shown in Figure 3.8.

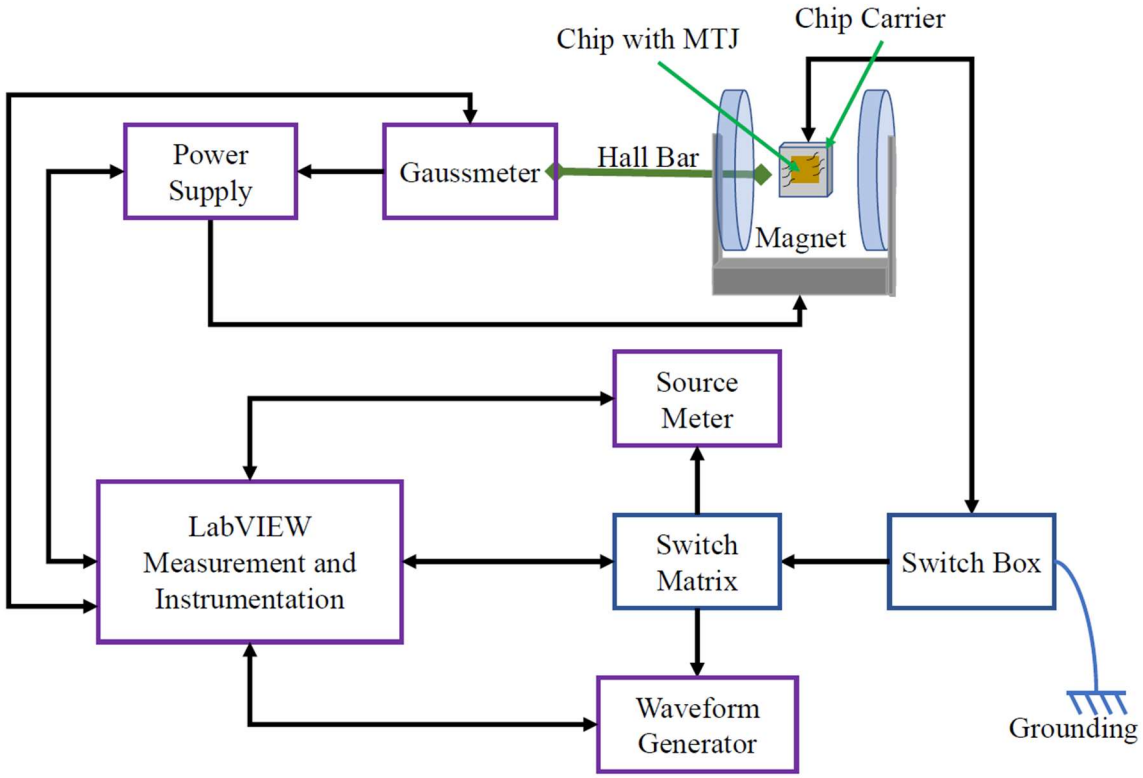

Figure 3.8: Schematic of the electrical measurement setup for characterization of MTJs

All the pieces of equipment were connected to the LabVIEW using the National Instruments Measurement & Automation Explorer (NI-MAX) software using General Purpose Interface Bus (GPIB) cables and controllers as shown in Fig. 3.8. I wrote LabVIEW codes using the virtual interface software architecture (VISA) protocol to communicate with the instruments by writing to and reading from the instrument registers.

A request for a particular field value is sent to the Lakeshore 475 DSP gaussmeter. As a result, the gaussmeter dynamically sends a voltage signal to the Kepco BOP 36 – 6DL bipolar power supply to supply more or less current to the magnet until the desired field is

reached. The power supply can go from 0 to ± 6 A in current and 0 to ± 36 V in voltage. The hall bar that is shown in the green in Fig 3.8 is used by the gaussmeter to sense the magnetic field produced by the magnet. This bar has to be placed close to the MTJ chip being measured in order to get accurate results for the measurement. This feedback mechanism represents a proportional-integral-differential controller, and the parameters have to be carefully selected to ensure that the desired value is reached in the optimum time possible. An overdamped system means that the system will take a longer time to reach the desired value while an underdamped system means that there will be a lot of overshoots and ringing hence the system will take a long time to settle at the desired field value.

The chip is wire-bonded to a chip carrier and mounted at the middle of the two magnetic arms. The chip carrier is then attached to a switch box which also serves the purpose of a grounding box. The switch box helps to eliminate any form of static charges from the device, user, or switching effects of the instruments. This switch box also helps to connect the pins on the MTJ chip to the output channels on the Keithley 708B switching matrix.

The key characterization devices are the Keithley 2401 sourcemeter and the Keysight 33600A series waveform generator. The sourcemeter is used to make Hall measurements and helps to characterize the resistance of the MTJ as shown in Fig 3.9. Figure 3.10 shows how the waveform generator is used to generate voltage pulses that help switch magnetization of the soft ferromagnetic layer or move the domain wall along its track. The waveform generator also helps to nucleate the domain wall.

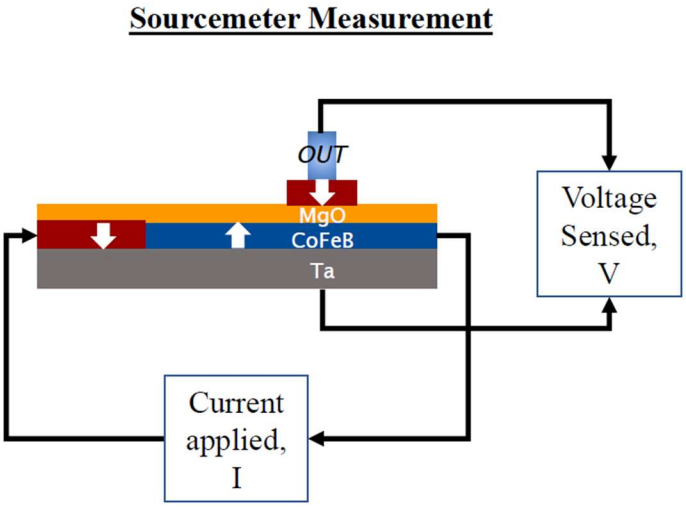

Figure 3.9: Calculating the Resistance of an MTJ using a sourcemeter

When the desired field value is reached, the LabVIEW software that I designed will send an instruction to the switching matrix for the user to select the pin chips that they will like to use in the measurement and then coordinates the sourcemeter and the waveform generator in the device measurement while data is being logged and a plot is automatically generated for the user to view in real time.

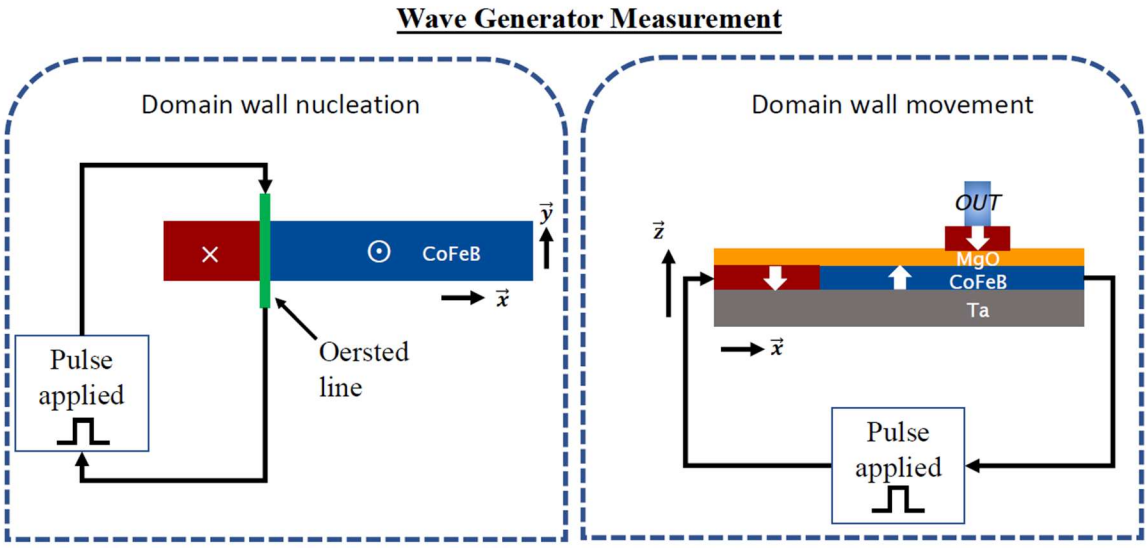

Figure 3.10: How the waveform generator is used to nucleate the domain wall and move the domain wall. Note that if using a STT, the pulse is applied through the CoFeB layer while for an SOT switching, the pulse is applied through the tantalum.

3.3.4. Key findings

The major findings were that the average device *TMR* = 171 $\pm$ 21% was close to the unpatterned average *TMR* = 168 $\pm$ 6%, but with increased standard deviation. The device average *RA* = 29$\pm$ 3 $\Omega - \mu m^2$ was also close to the unpatterned average *RA* = 35 $\pm$ 2 $\Omega - \mu m^2$. These results show both the *TMR* and *RA* are maintained after patterning, and that there is up to 203% *TMR,* close to the expected highest *TMR* (~200%) seen in PMA CoFeB-MgO MTJs[177]. This is a large improvement over previous results where the patterning degraded the *TMR* to 10-40%[169],[170],[174], and overcoming this degradation has been the focus of other recent domain wall-based logic research[178]. The *TMR* value in MTJs is analogous to the ON/OF ratio parameter in transistors. It determines the current separation between the 0 and 1 states[168]. Hence, having a high *TMR* is important in MTJs for logic applications.

Keeping the field under the switching field for the pinned reference layer, $H_{c,pinned}$ = -186 $\pm$ 25 mT, the free layer was switched to obtain $R_{MTJ} = R_P$ or $R_{MTJ} = R_{AP}$.

Studies were carried out to observe the DW-MTJ switching behavior with voltage when no domain walls were nucleated in the free layer. The saturation magnetization of 50 mT was used to initial magnetization of the free layer out of plane and 1 µs voltage pulses V of increasing amplitudes of step size 0.5 V were applied between *IN* and *CLK* terminals. Results show that the cycle-to-cycle distribution of switching voltage V_C of between 44 – 75% was gotten depending on the lattice imperfections of the ferromagnetic wire.

In an alternate case, a 50 ns pulse of 2 V was used to nucleate the DW at an initial position at the left notch of the DW track. A field of -120 mT saturation field was applied to bring

the device to an antiparallel state. We observed, as shown in figure 3.10, that when 1 μs voltages pulses were swept from 0 to 6 V at steps of 0.1 V for a particular device over 10 cycles, we get a reduction in cycle-to-cycle distribution of switching voltage V_C to around 10 % with an average depinning current of 4.22 V. Please refer to ref [179] for further details on the analysis methods and results.

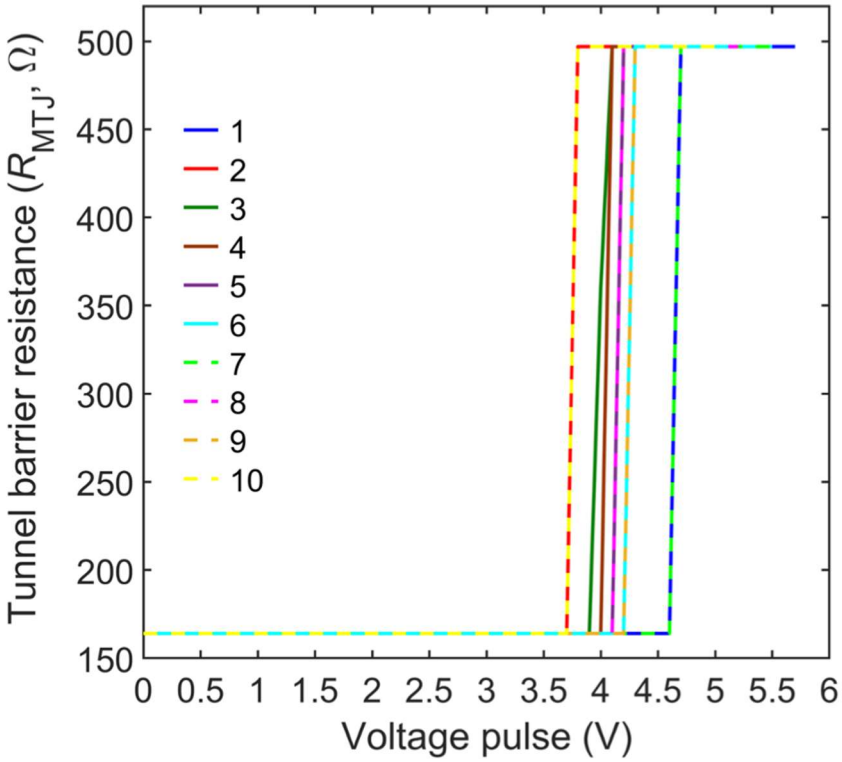

Figure 3.10: Cycle-to-cycle variation. (a) Device 1 initialization cycle-to-cycle variation over 10 cycles, when the DW is re-initialized each cycle using the Oersted field line. H_B = -100 mT.

3.4. CONCLUSION

In this chapter I have shown how the careful understanding of the magnetization dynamics can help us create better and efficient magnetic devices. I highlight my work on the micromagnetic simulation of a scaled MTJ device which will be applied to developing

an energy efficient multiply and add circuit for machine learning purposes. I also present my work in designing the measurement setup used to characterize the critical switching field and voltage for a fabricated MTJ device. There is more work to be done in getting an optimal device geometry for the scaled MTJ that I am simulating and in reducing the variability in device performance after the MTJ fabrication.

Chapter 4: The Application of MTJs to Neuromorphic Computing

4.1. INTRODUCTION

Spiking neural network (SNN) is regarded as the third generation of the neural network model [180,181]. This is because it is the closest to the biological network in neural architectures that has been developed in recent times. The physical realization of SNN in specialized hardware make up the core of neuromorphic computing which involves emulating the neural structure and operation of the human brain [182,183]. The main components of the brain used for memory, logic, and perception are the neuron and the synapse [61,81,184]. As a result, it is important to explore fundamental physics of devices that make them capture neural and synaptic behaviors accurately.

The MTJ has been identified to display both neuronal [82] and synaptic [172] behaviors when the structures are modified as shown in Fig. 4.1. The neuron structure is shown in Fig 4.1a where the tunnel junction is placed at one extreme of the domain wall track while inputs are sent in from the input terminal. When the domain wall reaches the tunnel junction there is a sudden drop in resistance of the MTJ and therefore a large current spike passes through similar to a neural spike. The strong permanent magnet coupled to the base of the MTJ structure induces a stray field that inhibits the motion of the domain wall and also causes its backward motion when no signals are coming in. This behavior largely captures that of a biological neuron that exhibits a leaky-integrate-fire behavior.

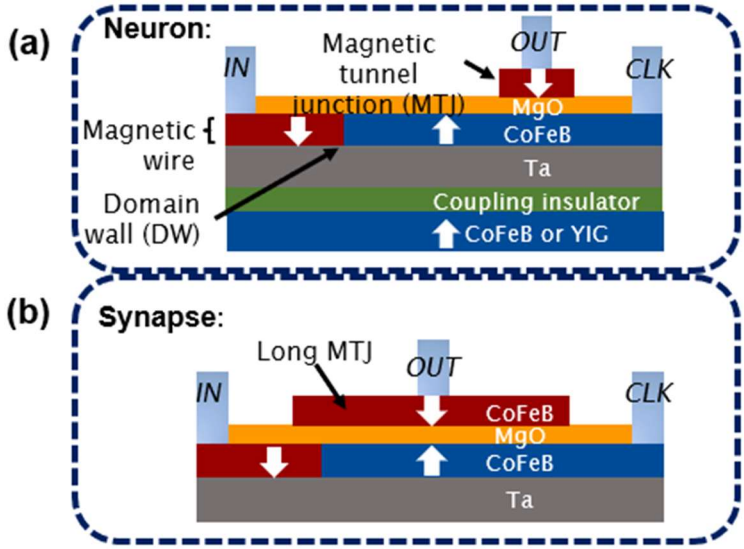

Figure 4.1: Cartoons showing the MTJ structure for (a) a leaky-integrate-fire neuron and (b) a synapse.

While I have collaborated on the work that explores the neuronal behavior of the MTJ [82,185–187], I discuss my primary work on capturing synaptic behavior in the rest of this chapter.

4.2. THREE-TERMINAL MAGNETIC TUNNEL JUNCTION SYNAPSE CIRCUITS SHOWING SPIKE TIMING DEPENDENT PLASTICITY.[3]

4.2.1. Introduction

The majority of the work on spintronic neuromorphic computing has focused on the implementation of neurons using 2T-MTJs [19],[22],[23],[31]–[33] while doing most of the synaptic weight training offline. Others have attempted to use 2T-MTJs as synapses

[3]The results, discussions and figures presented in this section have been adapted with permission from the following reference [172] O. Akinola, X. Hu, C. H. Bennett, M. Marinella, J. S. Friedman & J. A. C. Incorvia. Three-terminal magnetic tunnel junction synapse circuits showing spike-timing-dependent plasticity. *J. Phys. D. Appl. Phys.* **52,** (2019). The dissertator, O.G. Akinola designed conceived and designed the experiment, designed the circuits, performed the simulations, analyzed the data, and largely wrote the manuscript with contributions from all the authors.

which are limited to binary weights [34]. Some work has been done on using 3T-MTJs as neurons [25], including our recent work developing a leaky, integrate, and fire (LIF) neuron with inherent lateral inhibition [24],[35]. But only a few efforts have used 3T-MTJs as synapses. One example is the use of a transistor circuit and a 3T-MTJ to show stochastic STDP in a binary synapse [36]. This, however, does not show a multi-state resistance or conductance weighting system that is similar to the biological synapse [37]–[39]. Another example is an all-spin neural network in which binary 3T-MTJ neurons are connected to binary 3T-MTJ synapses through transistor axons [25]. Although this still uses binary synapses and does not show LTP or LTD, it sought to use less CMOS-based devices, which can be beneficial for energy efficiency. However, that implementation does not allow for fine adjustments of the synaptic weights, which may be critical to implementing plasticity-based learning algorithms.

Here, we have designed and modeled a synapse circuit using 3T-MTJs that captures STDP and allows online learning. We show that there is a correlation between the current amplitude to switch the domain wall and the timing between the pre-synaptic signal and the post-synaptic signal, and that the response of the circuit mimics the biological neural model of potentiation and inhibition. We also show that lithographically-defined notches along the length of the domain wall track create controlled pinning of the domain wall location to enable the semi-analog multiple weight state depending on the pre- and post-synaptic signals.

We first present the 3T-MTJ circuit that has been developed for STDP and provide details about its functionality. Then, we show results from the SPICE simulation of the circuit. Lastly, we show the micromagnetic simulation results for current pulses from the circuit applied to a 3T-MTJ to achieve multiple weight states.

4.2.2. Methods

The model for the artificial synapse is shown in Fig 4.2. To have the 3T-MTJ synapse, Fig. 4.2a, show STDP behavior, we need the position of the domain wall, and therefore the resistance weight, to respond to the timing between spiking signals at both the *IN* and *CLK* terminals. What the domain wall position does respond to is the sign of the current $I_{Synapse}$ between the *IN* and *CLK* terminals, which if above the domain wall depinning current will move the domain wall right or left.

Thus, to achieve STDP we design a circuit that converts the timing of the pre- and post-synaptic signals to a sign and magnitude change in $I_{Synapse}$. We keep the circuit small and as simple as possible so that it could be integrated into a dense array of the 3T-MTJ synapses with a small area overhead.

Figure 4.2b depicts the circuit, consisting of a 3T-MTJ sandwiched between two capacitor-resistor-diode networks (green disks) through which it is connected to the pre- and post-synaptic neurons. The pre-synaptic signal comes from the output of the pre-synaptic neuron; the post-synaptic signal comes from the output of the post-synaptic neuron; and the output of the synapse goes into the input of the post-synaptic neuron. Here, we focus on the synapse behavior; the details of how the neurons and synapses connect are not specified.

The details of the circuit are shown in Fig. 4.2c. It includes minimal additional resistors and capacitors to enable STDP that could be integrated into a crossbar array. We have modeled the FM free layer of the 3T-MTJ in case of an STT device (or HM in case of an SOT device) as a patterned thin film resistance $R_{Synapse}$ in the balanced RC circuit. The center MTJ resistance of the device is not included. Diodes are placed on both ends of the circuit to prevent back current flow.

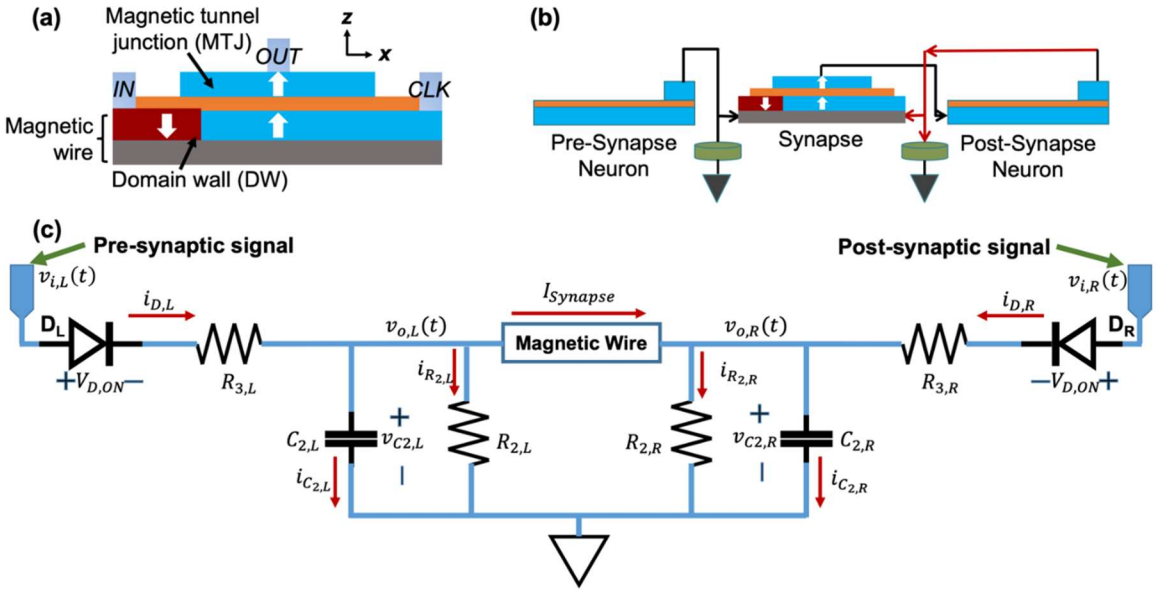

Figure 4.2: (a) Side-view cartoon of the 3T-MTJ device. The up/down arrows and blue/red color represent the magnetization vector of the ferromagnetic thin films; the orange represents the tunnel barrier. (b) Cartoon showing the 3T-MTJ synapse integrated with the pre-synaptic neuron and post-synaptic neuron. The capacitors (green discs) are integral in timing coordination in order to move the domain wall. (c) The balanced synapse circuit schematic with the MTJ magnetic wire (in case of STT) or heavy metal (in case of SOT) modeled as a resistor. $I_{Synapse}$ is the current that flows through the free layer of the MTJ and moves the domain wall, thereby adjusting its weight in the form of tunneling resistance. This schematic is used in the circuit analysis and in the SPICE simulation.

The capacitor to the left of the 3T-MTJ ($C_{2,L}$) and the capacitor to the right ($C_{2,R}$) have equal capacitances. The left resistor ($R_{2,L}$) and right resistor ($R_{2,R}$) are equal resistances. ($R_{3,L}$) and ($R_{3,R}$) are the sum of a resistor and the contact resistance to the left and the right of the 3T-MTJ, respectively. The dynamics of the circuit depend on the arrival times of the pre-synaptic neuron signal (voltage amplitude $v_{i,L}(t)$) and the post-synaptic neuron signal (voltage amplitude $v_{i,R}(t)$), the states of the the diodes D_L and D_R, and the time constants of the RC networks $R_{2,L}C_{2,L}$ and $R_{2,R}C_{2,R}$. These states affect the direction of flow of

$I_{Synapse}$ which will increase or decrease the conductance of the MTJ through STT or SOT switching of a domain wall in the free layer. The current *i* is labeled throughout the circuit.

For either of the diodes to be on, the input signals from the pre-synaptic or post-synaptic neurons must be such that:

$$v_{i,R}(t) - v_{o,R} - i_{D,R}R_{3,R} \geq V_{D,ON} \quad (1)$$

$$v_{i,L}(t) - v_{o,L} - i_{D,L}R_{3,L} \geq V_{D,ON.} \quad (2)$$

When both diodes D_L and D_R turn on at the same time, the pre-synaptic and post-synaptic signals arrive at the same time, and assuming the voltages at the capacitors $C_{2,L}$ and $C_{2,R}$ are at the same value, no current flows through the magnetic wire, i.e.

$$I_{Synapse} = 0; i_{D,L} = i_{D,R} \geq 0, v_{i,L}(t) = v_{i,R}(t). \quad (3)$$

For other conditions (when both diodes are on), the complete set of parametric equations for the circuit can be written from nodal analysis as

$$v_{i,L}(t) - v_{o,L} - i_{D,L}R_{3,L} = V_{D,ON} \quad (4)$$

$$v_{i,R}(t) - v_{o,R} - i_{D,R}R_{3,R} = V_{D,ON} \quad (5)$$

$$i_{D,L} = i_{C_{2,L}} + \frac{v_{o,L} - v_{o,R}}{R_{synapse}} + \frac{v_{o,L}}{R_{2,L}} \quad (6)$$

$$i_{D,R} = i_{C_{2,R}} - \frac{v_{o,L} - v_{o,R}}{R_{synapse}} + \frac{v_{o,R}}{R_{2,R}} \quad (7)$$

$$i_{C_{2,L}} = C_{2,L}\frac{dv_{o,L}}{dt} \quad (8)$$

$$i_{C_{2,R}} = C_{2,R}\frac{dv_{o,R}}{dt}. \quad (9)$$

Using Laplace transforms, we write the input voltages as

$$v_{i,L}(s) = V_{iL} * \left(\frac{1 - \exp(-s * t_{pw})}{s * (1 - \exp(-t_p * s))} \right) \quad (10)$$

$$v_{i,R}(s) = V_{iR} * \left(\frac{\exp(-s * t_d) - \exp\left(-s * (t_d + t_{pw})\right)}{s * (1 - \exp(-t_p * s))} \right) \quad (11)$$

where s is the Laplace frequency variable, V_{iL} and V_{iR} are the pre- and post-synaptic signal amplitudes, respectively, t_{pw} is the pulse width, t_d is the delay between the pre-synaptic signal and the post-synaptic signal, and t_p is the period of both the pre-synaptic and post-synaptic signals. The current through the MTJ synapse can then be derived as:

$$I_{Synapse} = \frac{v_{o,L} - v_{o,R}}{R_{synapse}}. \quad (12)$$

When both diodes D_L and D_R are off and assuming they turn off at about the same time at $t = 0$, the current flowing through the magnetic wire will be a function of the difference of the voltages of $C_{2,L}$ and $C_{2,R}$. And given that $C_{2,L} = C_{2,R} = C_2$ and $R_{2,L} = R_{2,R} = R_2$, I_{Syn} can be written as:

$$I_{Synapse} = \exp\left(-\frac{t * (2 * R_2 + R_{synapse})}{C_2 * R_2 * R_{synapse}} \right) * \left(v_{C2,L}(0) - v_{C2,R}(0) \right) \quad (13)$$

where $v_{C2,L}(0)$ and $v_{C2,R}(0)$ are the voltages of capacitors $C_{2,L}$ and $C_{2,R}$, respectively, at time $t = 0$ when both diodes are off.

4.2.3. Results and Discussion

Circuit Simulation Results

The 3T-MTJ synapse circuit is simulated in HSpice using $v_{i,L}(t)$ and $v_{i,R}(t)$ pulse widths of 1 ns with a 10 ns period. Different delay conditions from 0.1 ns to 5 ns between

onset of V_{iL} and onset of V_{iR} are implemented. Figure 4.3 shows the results of the HSpice simulation, where we plot both the transient voltage pulses and current through the magnetic wire, $I_{Synapse}$. It can be seen from Figs. 4.3a and 4.3b that when the pre-synaptic signal arrives (in the form of a voltage pulse) before the post-synaptic signal, a positive current flows through the 3T-MTJ synapse, which will increase the conductance of the MTJ stack. The magnitude of the current is inversely proportional to the delay between the pre-synaptic neuron signal and the post-synaptic neuron signal. Figures 4.3d and 4.3e show that if the post-synaptic neuron fires before the pre-synaptic neuron, there is a negative flowing (depressing) current through the synapse, and its magnitude is also dependent on how soon the pre-synaptic neuron fires after the post-synaptic neuron. Then there are the cases shown in Figs. 4.3c and 4.3f in which the pre-synaptic neuron fires midway between the span of the post-synaptic neuron firing twice in the first case; and the post-synaptic neuron fires midway between the span of the pre-synaptic neuron firing twice in the second case. In both cases there are equal magnitudes of both positive and negative current spikes flowing through the synapse. This can lead to oscillation of the output MTJ resistance. It should be noted that in all the simulations there is an initial larger current spike, which is an artifact of the circuit starting at time $t = 0$.

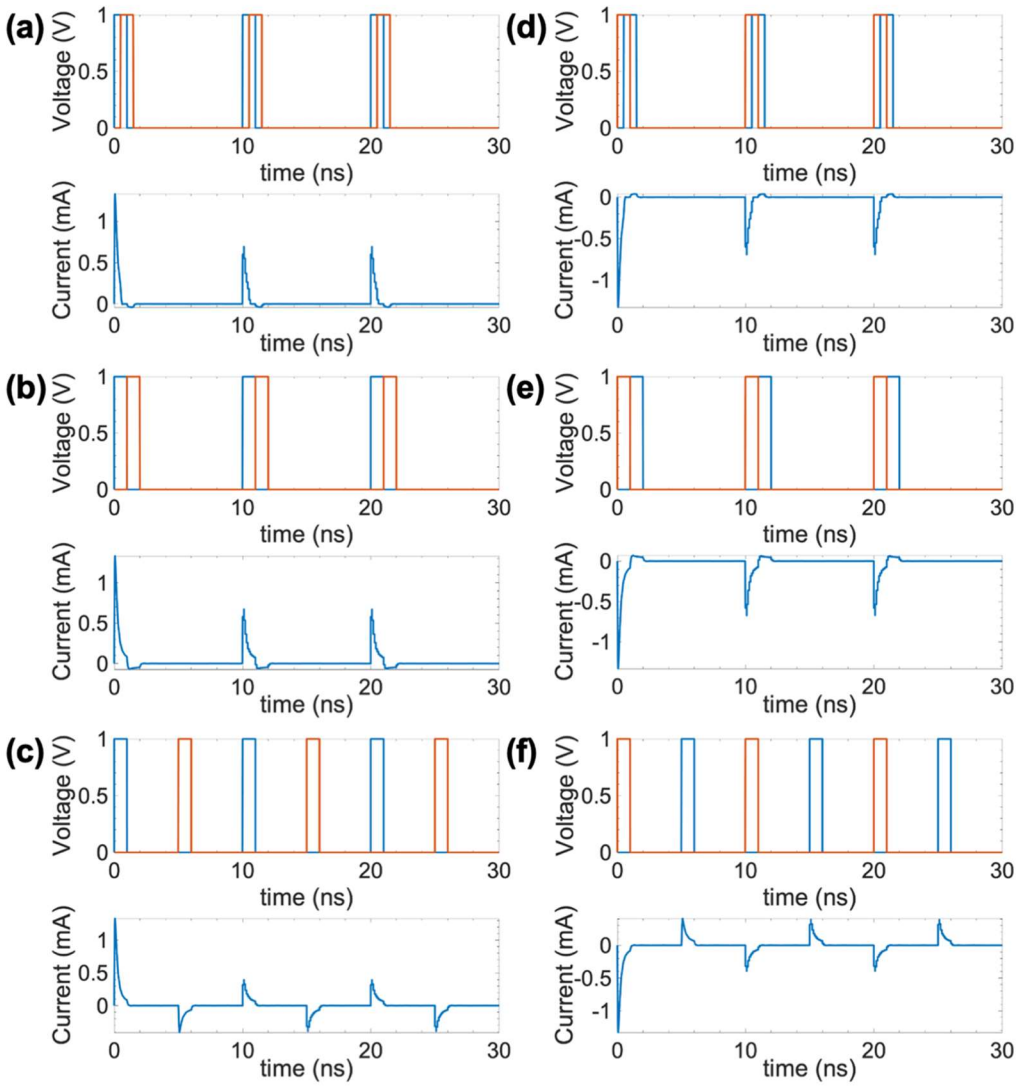

Figure 4.3: Spice simulation results for different delay scenarios between pre-synaptic neuron spike and post-synaptic neuron spike. (a), (b), (c) show the currents (lower plots) that flow through the magnetic wire when the pre-synaptic neuron fires 0.5 ns, 1 ns and 5 ns, respectively, before the post-synaptic neuron fires. Likewise, (d), (e), (f) show the currents (lower plots) that flow through the magnetic wire when the pre-synaptic neuron fires 0.5 ns, 1 ns and 5 ns, respectively, after the post-synaptic neuron fires. The pre- and post-synaptic firing are represented by voltage pulses of 10 ns period and 10% duty cycle as shown in the upper plots.

To compare with the behavior of biological synapses, the current that passes through a chemical synaptic channel, $I_{syn,bio}(t)$, can be represented by[59,188]

$$I_{syn,bio}(t) = g_{syn}(t)\big(u(t) - E_{syn}\big) \tag{14}$$

which depends on the difference between its reversal potential E_{syn} and the actual value of the membrane potential, $u(t)$. $g_{syn}(t)$ is a superpostion of synaptic conductances $\bar{g}_{syn}$ with exponential decay of time constant τ and given by

$$g_{syn}(t) = \sum_{f} \bar{g}_{syn} e^{-\frac{t-t^f}{\tau}} \Theta(t - t^f) \tag{15}$$

where t^f is the arrival time of a pre-synaptic action potential and $\Theta(t - t^f)$ is a Heaviside step function. $g_{syn}(t)$ can be simplified for a single neuron-to-neuron synaptic connection by the alpha-function[188]

$$g_{syn}(t) = \frac{t}{\tau_s} e^{-\frac{t}{\tau_s}} \tag{16}$$

where τ_s is the time constant of the response which specifies slow or fast transmission.

In Fig. 4.4a, we plot $I_{synapse}(t)$ from the Hspice simulation for the Fig. 4.3a condition ("SPICE "), compared to the analytical solution Eqn. (12), using parameters from Eqns. (4)-(11) ("Analytical"), with t_{pw} = 1 ns, t_d = 0.2 ns, t_p = 10 ns, R_2 = 10 kΩ, $R_{Synapse} = 100\ \Omega$, $R_3 = 50\ \Omega$, and C_2 = 1 × 10^{-12} F. We also compare to the biological synapse transient current behavior using τ_s = 0.1 ns ("Biological"). It can be seen that we closely capture the biological transient behavior with the circuit, which also agrees well with simulations, mathematical modeling and analysis of biological neurons[188–196].

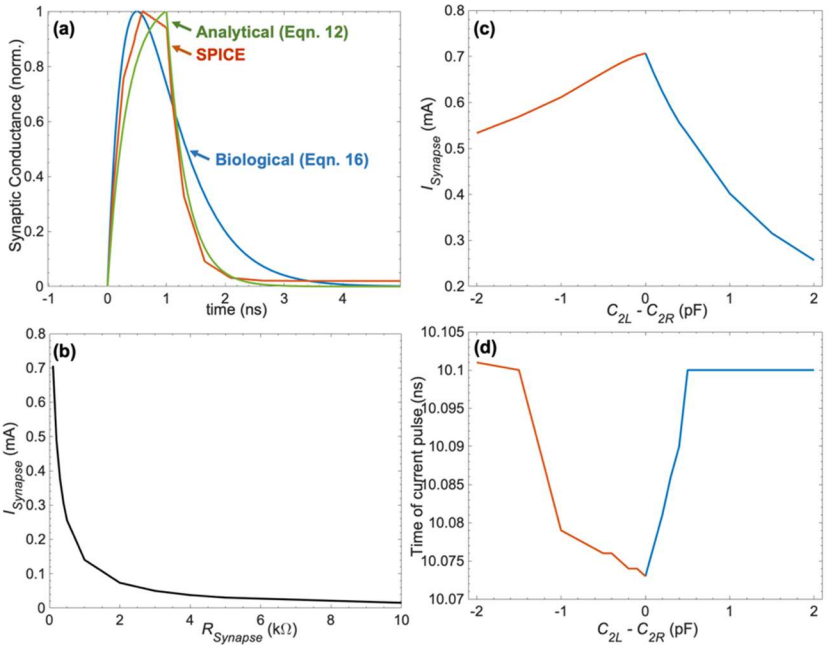

Figure 4.4: (a) Comparison of the transient synaptic current from the SPICE circuit to the analytical expression of the circuit from Eqns. 1-12 and the biological synapse alpha-function from Eqns. 14-16. The plots have been normalized to their maximum values. (b) Plot of current at the synapse vs. resistance of the 3T-MTJ magnetic wire. (c) Plot of current at the synapse and (d) current pulse timing vs. difference in capacitance of the two capacitors in the circuit.

Figure 4.4b shows the $I_{Synapse}(t)$ dependence on $R_{Synapse}$. As the resistance increases, the current decreases exponentially. This provides a design requirement for the 3T-MTJ device to minimize the resistance of the bottom layer(s), e.g. by using a thicker HM layer. The resistance needed depends on the required current for depinning the domain wall for a given device size and materials.

To calculate how much the circuit can tolerate imperfections between the matched capacitors, in Fig. 4.4c we plot $I_{Synapse}$ while increasing the difference between the capacitance of C_{2L} and C_{2R} up to a factor of 3 mismatch. The figure shows the circuit is more tolerant of $C_{2R} > C_{2L}$ with a 3x mismatch producing a 25% change in $I_{Synapse}$. For

$C_{2R} < C_{2L}$, the 3x mismatch reduces the synapse current by a larger factor up to 64%. This analysis assumes the pre-synaptic signal $v_{i,L}$ leads the post-synpatic signal $v_{i,R}$ by 0.1 ns. It is expected that the graph will be similar but flipped along the y-axis if the pre-synaptic signal lags the post-synaptic signal by the same amount of time (0.1 ns).

To investigate how the response time of the current through the 3T-MTJ wire to the pre- and post-synpatic signals varies with the capacitance mismatch on either side of the MTJ, we took the the onset time for signal $I_{Synapse}$ on the second period, using a period of 10 ns and plotted it against the capacitance mismatch. The second period was used rather than the first period because of the artifact that comes with starting the simulation at $t = 0$. Figure 3d shows the timing of the current through the synapse is tolerant to capacitance mismatches with little or no difference in the current timing as the capacitance mismatch gets larger. The current pulse comes quicker on the average if C_{2R} is increased with respect to C_{2L} and saturates as the difference approaches -2 pF. The reason for the small 0.3% dip in timing shown in Fig. 4.4d is not yet fully understood.

Spike-Timing-Dependent Plasticity (STDP)

Taking the different current magnitudes flowing through the synapse at different timing conditions, we graph the current magnitude against time delay between the pre-synaptic neuron spike and the post-synaptic neuron spike. The plot is shown in Fig. 4.5. It is seen that the smaller the delay, either between the pre-synaptic neuron spike and the post-synaptic neuron spike or vice versa, the higher the current magnitude that flows through the synapse.

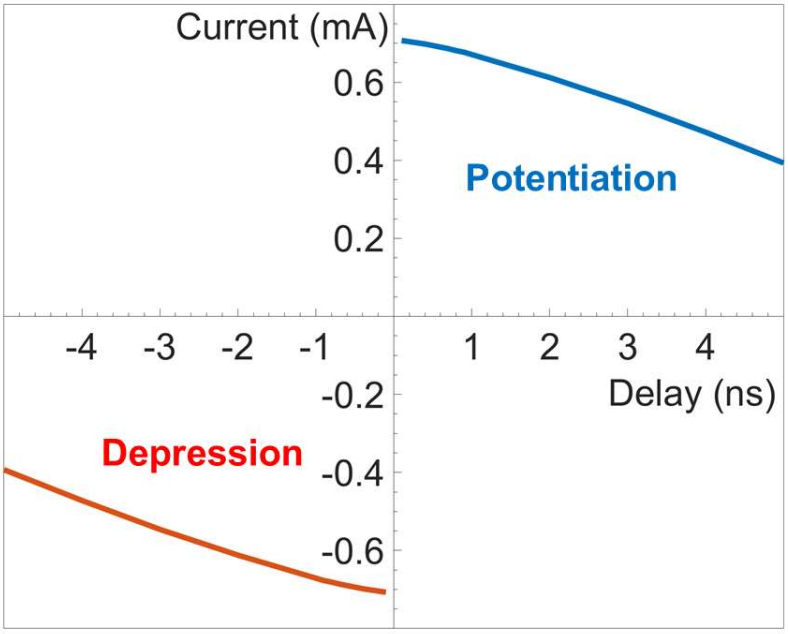

Figure 4.5: Potentiation and depression currents from the SPICE simulation as a function of spiking delay between pre-synaptic and post-synaptic neurons.

Thus, the circuit captures both potentiation and depression, and also captures that the amplitude of the strengthening or weakening of the synapse is based on the timing between the pre- and post- signals. This has a high resemblance to the work of Bi and Poo's clinical experiment on STDP which shows LTP and LTD induced in synapses between hippocampal glutamatergic neurons[87]. Additionally, when the circuit has no correlation between the two signals, we get oscillation in time back and forth between two resistance states, maintaining the state of the synapse conductance.

Micromagnetic Simulations

To observe how the circuit will affect the magnetic behavior of the 3T-MTJ synapse, we run the HSpice model and input the *vector direction* of the resulting $I_{Synapse}$ into a micromagnetic simulation using MuMax3[117] and rendered in OOMMF[197]. While 3T-

MTJs have been modeled as a synapse in perfect wires[49,77,198–203], it is a challenge in a real device to repeatably control the distance of the domain wall along the free layer "racetrack" under the MTJ. One solution, implemented here, is to use lithographically defined notches, which are anisotropy barriers that pin the domain wall.

We model a 1 μm long x 32 nm wide x 4 nm thick CoFeB ferromagnetic wire with perpendicular magnetic anisotropy of 1.5×10^6 J/m^3, exchange stiffness of 13×10^{-12} J/m, damping constant of 0.02, saturation magnetization of 1.44×10^6 A/m, and non-adiabacity constant of 0.02. The notches are 16 nm in diameter with a pitch of 64 nm. Using STT, we use 1 ns pulses of current density 2×10^{12} A/m^2, where the direction of the current depends on the relative timing of the pre- and post-synaptic neurons from the circuit model. The pulses have a period of 10 ns.

The results of the micromagnetic simulation are shown in Fig. 4.6a as snapshots of the wire magnetization after the domain wall motion has stopped after each current pulse (view is $-\hat{z}$ compared to Fig. 4.2a). At the initial state 0 the domain wall is in the center of the wire. Figure 4.6b depicts the polarity of the ten current pulses applied sequentially across the magnetic wire.

We see that each current pulse moves the domain wall left or right depending on the direction of the current. Thus, with a long MTJ placed on top of the wire (not shown), this will controllably increase or decrease the MTJ conductance, setting the synaptic weight. It can be seen that each positive current pulse moves the DW to the left, getting pinned at subsequent notches, while each negative current pulse moves the domain wall to the right, also getting pinned at subsequent notches. Positive current pulses reduce the tunneling resistance of the device and hence increase the weight of the synapse while negative current pulses do the contrary.

In Fig. 4.6c we use measured numbers for CoFeB MTJs fabricated in our group of 166% tunnel magnetoresistance and 20 Ω -μm^2 resistance-area product to convert the domain wall position to expected conductance weight for each corresonding domain wall position in Fig. 4.6a. Because the domain wall can be pinned at a particular notch for a long time if there is no current flowing, this gives the synapse a long-term memory effect. Also because the position of the domain wall along the wire is a resulant effect of potentiation and depression over time, we can safely say that the synapse undergoes LTP and LTD.

The length of the MTJ compared to the width of the domain wall determines the number of notches and hence the number of domain wall positions that can represent different resistance or conductance weights. In a magnetic wire with perpendicular magnetic anisotropy, the width of the domain wall w_{DW} is approximately determined by the width of the MTJ w_{MTJ} as $w_{DW} \approx \frac{W_{MTJ}}{4}$ [165]. This means that with a MTJ of length L_{MTJ}, the maximum number of weights (n_{weigh}) achievable will be given by the relation

$$n_{weights} \leq (L_{MTJ}/w_{DW}) \approx 4 \times L_{MTJ}/w_{MTJ}.$$

Depending on the number of weights needed, the length of the magnetic wire could be shortened to create more compact circuits.

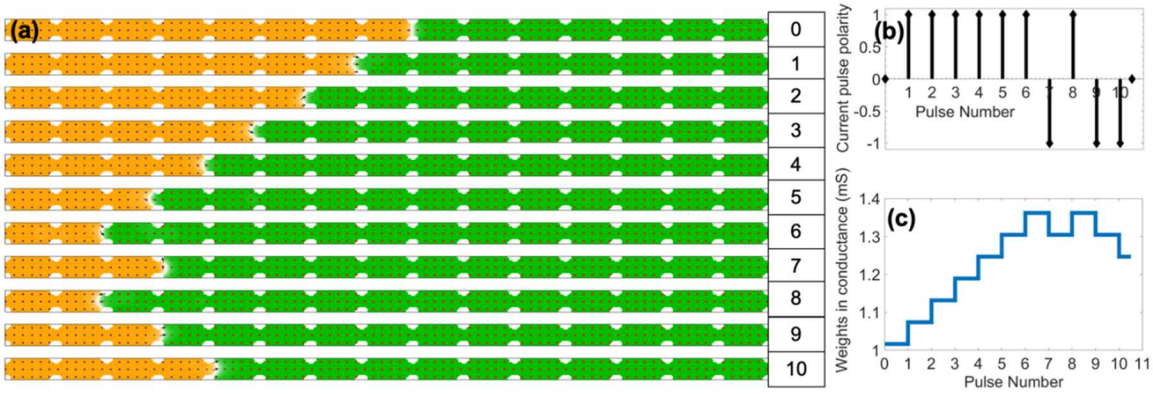

Figure 4.6: (a) Micromagnetic simulation snapshots for the current pulse train shown in (b) through a 1 μm long x 32 nm wide x 4 nm thick CoFeB ferromagnetic nanowire. The notches introduce anisotropies which pin the domain wall. (c) Plot of the resulting conductance weights vs. pulse number, assuming that the green-colored (right) domain is parallel to the top ferromagnetic layer and the orange-colored (left) domain is anti-parallel to the top ferromagnetic layer. The plot shows that the notches introduce a semi-analog behavior into the domain wall movement.

Benchmarking Against Competing STDP Implementations

The results of our micromagnetic and SPICE simulations allow us to make a direct comparison to other state-of-the-art proposals for nanodevice plaforms for implementing online STDP learning. Specifically, we consider how our analog STDP implementation using 3T-MTJ devices compares to phyically realized or proposed analog STDP building block cells using CBRAM[204], metal oxide[205,206], or polymeric[207] active switching layers. As visible in Table 1, the signature advantage of our system is its extreme (nanosecond range) STDP time window; the second fastest device, a CBRAM option, is over 2 orders of magnitude slower, and the other listed nanodevice options are slower still. Since this window serves as a speed limit for overall STDP learning, this could finally allow for online STDP learning functions in an integrated circuit co-integrated with NVM devices in an industrially-relevant context. Our proposal compares favorably in terms of

required voltage, and is comparable though not superior in terms of analog resolution provided by other nanodevices. Our proposal's major weak point relative to competing options is the relatively low resistance and on/off ratio provided by MTJ devices. However, this issue may be ameliorated by further device engineering.

	CBRAM [204]	**Metal Oxide (Al_2O_3/TiO_{2-x})** [205]	**Metal Oxide ($BiFeO_3$)** [206]	**Polymer (PEDOT:PSS)/Ta** [207]	**3T-MTJ (our approach)**
$R_{Synapse}$	5-50 kΩ	10-40 kΩ	~1 MΩ	1-2.5 kΩ	100 Ω-10 kΩ
Switching time	2-4 μs	20 ms	125 μs	50 ms	< 5 ns
$V_{post/pre}$	+/- 1.3 V	+/- 0.6-1.0 V	3.0 V+	+/- 2.0 V	1.0 V
Analog STDP Resolution	Intermediate (~5-10 states)	High (> 20 states)	Intermediate (~10 states)	High (> 30 states)	Intermediate (~10 states)

Table 4.1: Head-to-head comparison of critical parameters for nanodevice and CMOS co-integrated unit cells for providing analog STDP learning (we do not consider here the comparison to probabilistic or binary schemes).

Further transient analysis in SPICE

In the simulations above, for the SPICE circuit model we used a resistor to represent the 3T-MTJ free layer. To observe the effect of the circuit on the micromagnetic behavior of the 3T-MTJ synapse, we input the resulting current polarity from the circuit as a 1 ns current pulse of a fixed amplitude. Here, to capture the full dynamics of the circuit signal waveform (e.g. Fig. 4.3a) on the 3T-MTJ magnetic response, we implement a SPICE-only model of the full circuit that includes DW dynamics. We use a model of the 3T-MTJ for a

notch-free free layer that we have previously developed with Verilog A and is benchmarked against micromagnetic simulations[208]. The 3T-MTJ model is connected via the *IN* and *CLK* terminals to the circuit, replacing the free layer resistor in the Fig. 1d circuit schematic.

With the same capacitance and resistance values ($R_{2,L} = R_{2,R} = R_2$ = 10 $k\Omega$ and $C_{2,L} = C_{2,R} = C_2$ = 1 × 10^{-12} F) used for the simulation in Fig. 4.3, we simulate ten cycles of six constant delay conditions between onset of the pre-synaptic signal and onset of post-synaptic signal. The six delay conditions are shown in Fig. 4.7a. The transient DW position is shown in Fig. 4.7b. With 0 ns delay, the DW does not move. The DW responds to each spiking of the circuit by moving an incremental distance across the free layer, and it is evident that the shorter the non-zero delay, the farther the DW moves after each firing and over the 10 cycles, showing STDP behavior.

In Fig. 4.7c, we randomly vary the timing of the pre- and post-synaptic signals with 1 ns lead or lag between the signals. Figure 4.7d shows that in response to this pulse train the DW moves left or right depending on the polarity of the resulting current spikes across the 3T-MTJ free layer. These results show that including the precise waveform of the circuit corroborates the micromagnetic results. We do see some irregularities in how far and how smoothly the DW moves in response to multiple similarly timed pulses, which shows that external pinning may be important for controlling the conductance weights.

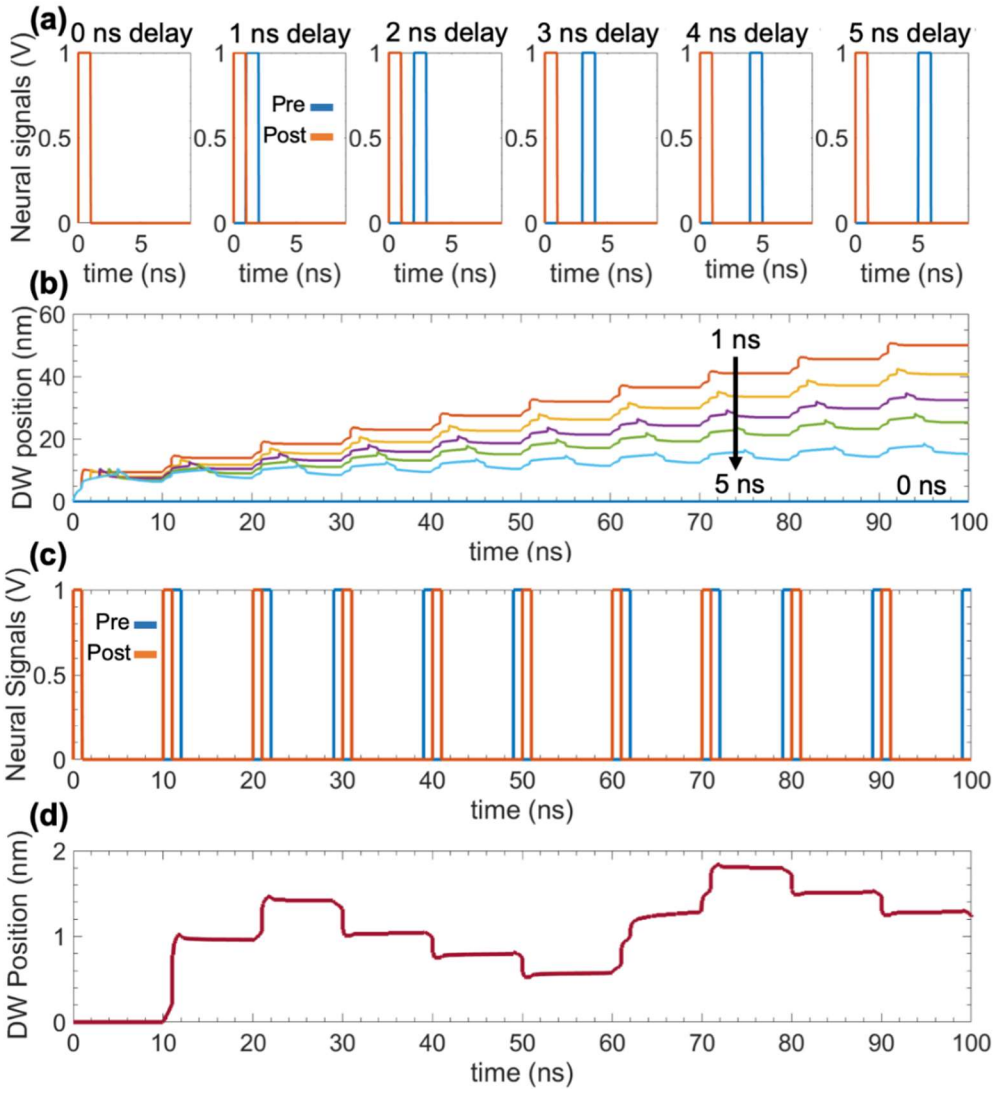

Figure 4.7 (a) Six modeled delay conditions between the pre- and post-synaptic signals, each simulated for ten cycles of 10 ns. (b) DW position output over time from the full SPICE model for the conditions in (a). Here the DW was initiated at the leftmost end of the free layer. (c) Modeled random train of delay conditions between the pre- and post-synaptic signals, with lead and lag times of 1 ns. (d) DW position output over time from the full SPICE model for the conditions in (c), showing the DW position, and therefore synaptic weight, is controlled by the timing between the signals.

4.3. TRANSIENT BEHAVIOR OF CROSSBAR ARRAY OF SYNAPSES

Using the synapse circuit developed above [172] and a 3T-MTJ spice model [208], I show the transient behavior of a 2 by 2 crossbar array whose cartoon is shown in Fig 4.8.

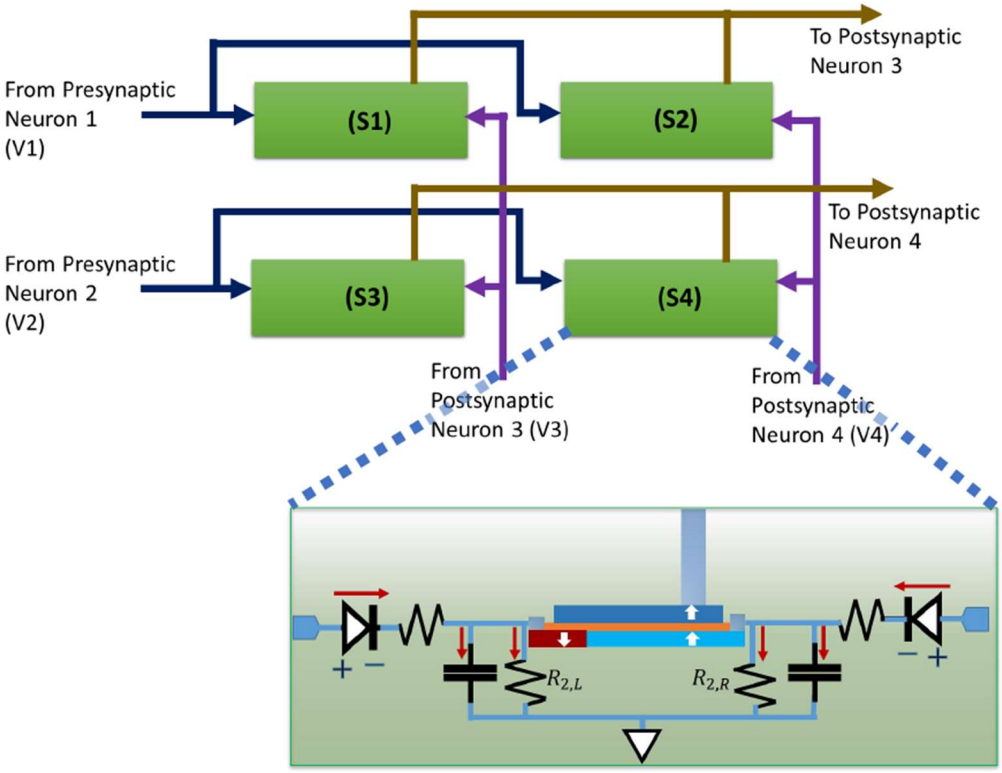

Figure 4.8: Cartoon showing a 2 x 2 crossbar array of synapses. The synapse modules S1, S2, S3 and S4 are developed from 3T-MTJs. The voltage pulses V1 and V2 feed into the synapses from the presynaptic neuron as shown in the blue arrows. The outputs of the synapses feed into the postsynaptic neurons through the golden arrows and the outputs of the postsynaptic neurons feed the voltage pulses V3 and V4 back into the third terminals of the synapses as shown in the purple arrows.

The crossbar array shows STDP for different delay conditions between the presynaptic neural spike and the postsynaptic neural spike. The shorter the time difference between the onset of the presynaptic neuron spike and the post synaptic neuron spike, the

higher the current flowing through the ferromagnet as shown in Fig 4.9. This is modeled in Cadence Spectre with a pulse width of 5 nm of 50 % duty cycle. The times of V1, V2, V3 and V4 are 2 nm, 4 nm, 0 nm and 1 nm, respectively. This gives a delay of 2 ns, 1 ns, 4 ns and 3 ns in pulses at the terminals of Synapses S1, S2, S3 and S4 respectively. Hence, the domain wall positions move further due to higher current magnitudes.

It can be seen that starting from time zero, the initial pair of presynaptic and postsynaptic pulses helps to randomly give the domain walls a head start. The domain wall for synapse S2 (red plot) rises faster because it has the least delay of 1 ns between its presynaptic and postsynaptic pulse. This is despite that its pulses came in a little later than that of S1 whose domain wall has an initial head start. It should be noted that the lesser the delay between the presynaptic pulse and postsynaptic pulses of each synapse, the more the current and hence the higher the rate of change of the domain wall position per neural event.

Scaling up this crossbar array we can implement an online weight adjustment by our 3T MTJ synapse in a machine learning classification task. We have used spatiotemporal encoding of the inputs to be able to better capture STDP. We also benchmark our results against conventional Neural Network architectures.

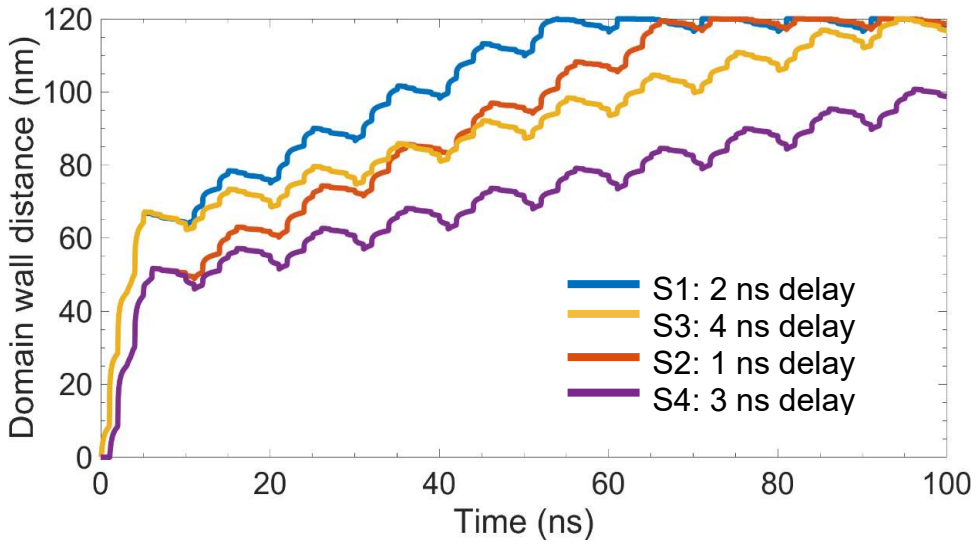

Figure 4.9. Plots showing the domain wall positions of the synapses in Fig 1. This is when the neural pulses V1, V2, V3 and V4 (all 1 V in magnitude) come into the synapses with 2 ns, 4 ns, 0 ns and 1 ns delay, respectively. This corresponds to delays of 2 ns, 1 ns, 4 ns and 3 ns between the presynaptic neural pulse and postsynaptic neural pulse in each of synapses S1, S2, S3 and S4 respectively.

4.4. IMPLEMENTATION OF SPIKING NEURAL NETWORK (SNN) ARCHITECTURE WITH MTJ SYNAPSE ARRAY SHOWING STDP

Showing that the synapse array works well is not sufficient. It is important to show that it can be used to perform real neuromorphic tasks. Here I show a framework that I have mapped out to implement a spiking neural network (SNN) using the synapse model developed such that it will be able to learn to classify the reduced MNIST handwritten image dataset from 0 to 9 using unsupervised learning. The dataset gotten from scikit-learn been scaled down from the 28 X 28 standard MNIST array to an 8 X 8 pixel array for tractability in smaller machine learning tasks [209]. The block diagram of the overall experiment is shown in Fig 4.10.

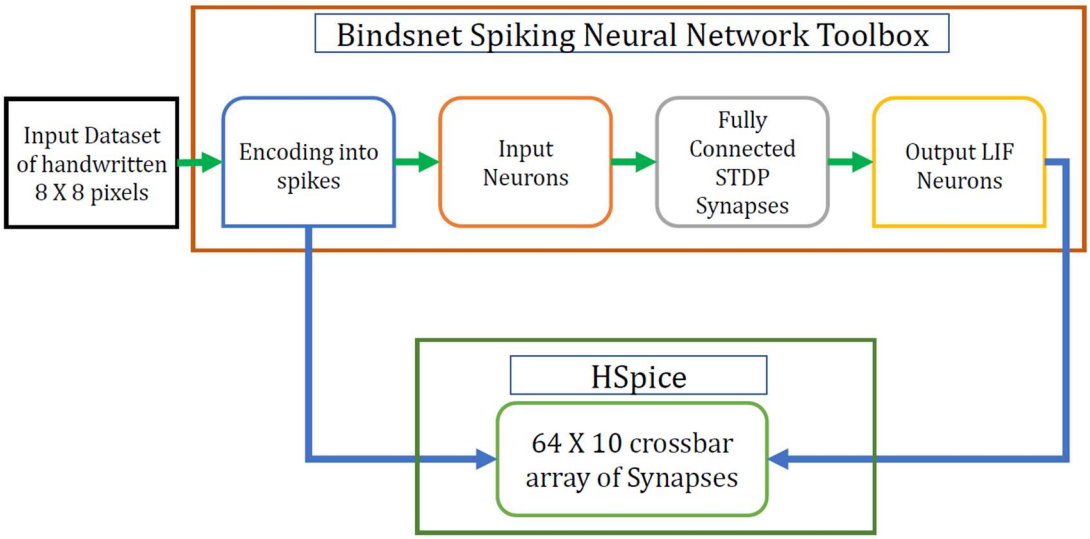

Figure 4.10: Block diagram of machine learning of an 8 X 8 pixel handwritten dataset input with an MTJ synapse array.

The BindsNET SNN toolbox, which is an open source SNN python library for the development of biologically inspired algorithms for machine learning purposes [210], was modified to work with the reduced dataset from Scikit-learn. Each pixel data was converted into time coded spikes using Poisson encoder. The DiehlAndCook2015 network model was used to train the data using STDP and a competitive mechanism. The output is from the STDP synapses are fed into output leaky-integrate-fire (LIF) neuron nodes to generate the output spikes. The details of this flowchart are presented in Fig. 4.11. The performance of the BindsNet SNN machine learning task is plotted in form of classification accuracy and confusion matrix. The accuracy gotten so far has been about 12%. This is an incredibly low accuracy, and work is still being done to bring up the accuracy to up to about 90%.

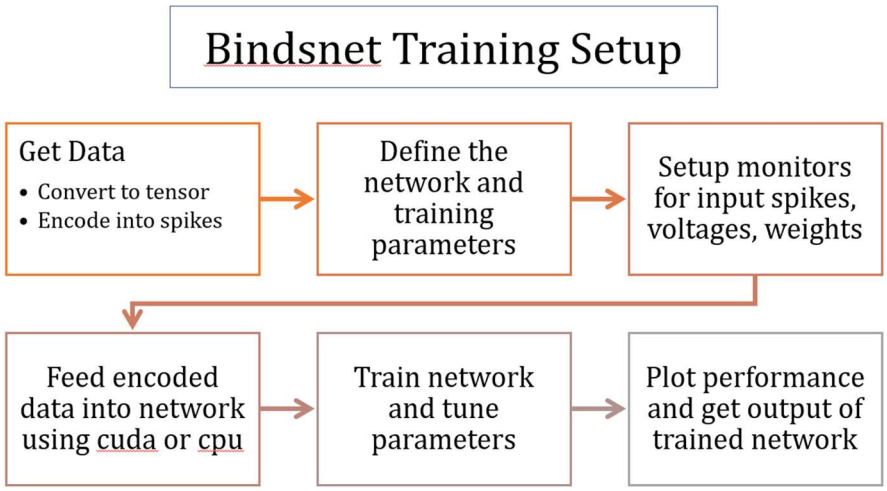

Figure 4.11: Block diagram showing flowchart for machine learning with the BindNET spiking neural network (SNN) toolbox.

The input and output spikes from the BindsNET toolbox are saved in a file with corresponding timestamps. This input file data will be parsed as input vectors into a 64 X 10 crossbar array of synapses designed with Cadence Virtuoso and simulated in HSpice. The flowchart for the simulation is shown in Fig. 4.12.

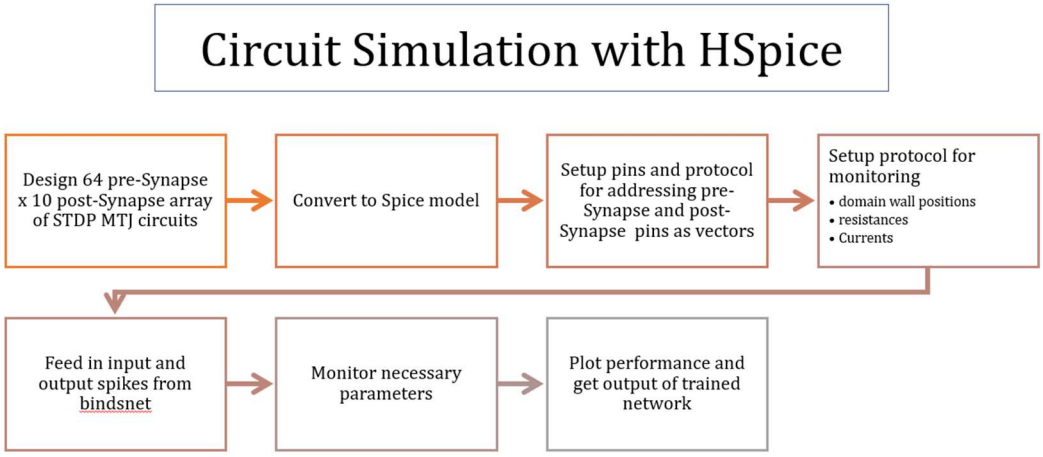

Figure 4.12: Block diagram showing flowchart for circuit implementation of a machine learning with MTJ synapse array in SPICE

4.5. CONCLUSION

We have successfully designed a 3T-MTJ synapse circuit that acheives STDP, LTP, and LTD, essential characteristics of biologically-inspired artificial synapses. We observe that the transient form of the current generated across the synapse corresponds to what is observed in biology, and that shorter delay between the pre- and post- neuron firing results in higher current for potentiation or depression, which shows high similarity to biological neuron behavior. We show that the circuit can acheive a semi-analog pinning of the domain wall along the length of the ferromagnetic wire of a 3T-MTJ using notches, and that the domain wall position can be set using the concept of STDP when integrated with the circuit.

We also show that the synaptic behaviour of our model holds strong in a tiny crossbar array. This is key progress towards making more bio-realistic artificial synapses with multiple weights, which can also be trained online with a promise of CMOS compatibility and energy efficiency.

We acknowledge that future work is needed to understand the impact of the additional circuitry for STDP on scaling and circuit density. And we believe that the results shown can be in the future integrated with the LIF neuron in a crossbar array fashion and used for online machine learning applications in tasks like pattern or speech recognition. And our work in the full scale handwritten digit recognition with MTJ synapses in a SNN is a giant leap in that direction.

Chapter 5: Conclusions and Future Works

5.1. DISSERTATION SUMMARY

This dissertation focuses on the concept of magnetism. It explores different levels of abstractions at which the physics of magnetism can be perfected and utilized for effective electronic and computing purposes.

Chapter 1 gives a broad overview of magnetism and applications. It starts from the fundamental materials science by discussing two-dimensional (2D) magnetic materials. Even though there has been a lot of work on 2D materials, not much progress has been made with synthesizing 2D magnetic materials. The Mermin-Wagner limitation has long thought to be the major limitation of achieving long range magnetic ordering. However, we see that the discovery of CrI_3 which is a 2D ferromagnet for single layers and Ising A-type antiferromagnet for bilayer sheets made us realize that 2D magnets can actually be experimentally derived. I then go on to discuss a unique class of 2D materials known as MXenes. MXenes are 2D transition metal carbides or nitrides. And some of the chromium based MXenes have been predicted from theory to have some form of ferromagnetism at near Curie temperatures.

The next layer of abstraction is the use of magnetic materials in devices. Magnetic tunnel junctions (MTJs), which is a device in which we have at least two ferromagnets separated by a tunnel barrier, has gained a lot of recognition recently. They have the ability to function as a logic device with high resistance states when the magnetic moments of the two ferromagnets are antiparallel and low resistance states when the magnetic moments are parallelly aligned in the same direction. They are also attractive because of their non-volatility creating potential headway for in-memory computing capability, normally off circuits, neuromorphic computing, to name a few. I take the reader another level of

abstraction further by discussing about neuromorphic computing. All fingers in computing are pointing towards the ability to understand and perceive the ubiquitous data around us in a way that is as energy efficient and meaningful as the human brain does. This quest has paved the field for the field of neuromorphic computing and the MTJ has been largely shown to be a device best suited for this purpose.

Chapter 2 walks through the methods I have developed to synthesize the Cr_2C MXene from its parent Cr_2AlC bulk MAX phase. This was done by removing the Al from Cr_2AlC etching in hydrochloric acid and a fluoride salt of an alkali metal. The best results were gotten when the etch was done in sodium fluoride (NaF) in a 9 °C environment and using a modified minimally intensive layer delamination method (mMILD) method. Using this method, I was able to reduce the etch time from 96 hours to 45 hours and get more products. I show the SEM images and a couple of results that were gotten from various characterization methods including the EDX, XRD, XPS, Raman, TEM. I also show some preliminary magnetic characterization data from SQUID and some of my attempts to separate the products into nanosheet by doing a tape exfoliation.

In chapter 3 I start by discussing the theory of micromagnetics in a little more detail. The dynamics of magnetization in a ferromagnet can be understood by exploring how the magnetic moments change with time. This rate of change of magnetization gives rise to a couple of torques that can be used to explain field induced magnetization switching (FIMS) or current induced magnetization switching (CIMS) in a magnetic device. SOT has been shown to be more responsive and energy efficient method than STT method of CIMS. I show some of my work on the micromagnetic simulation of a scaled MTJ device that can be used to create a more energy efficient non-volatile multiply and add array circuit for machine learning purposes. I also discuss my work on the electrical characterization of DW-MTJ SOT devices. I helped with writing the measurement automation code for the

electrical measurement setup that was used to characterize some fabricated MTJ devices. We calculated the TMR value and the cycle-to-cycle variation in the switching voltages for the device.

In chapter 4 I discuss about my work in using the three terminal magnet tunnel junction (3T-MTJ) to model a biological synapse. Some previous work has been done in modeling the LIF neuron behavior with MTJ. This chapter focuses more on modeling synaptic behavior. Adding a resistor capacitor network at the both ends of a 3T-MTJ allows it to capture the spike timing dependent plasticity of biological neurons. The STDP is fundamental to learning, perception, and memory in humans and the ability to effectively capture it means that we can now be able to give computers the ability to perceive the physical world like humans do.

5.2. DIRECTIONS FOR FUTURE WORK

5.2.1. Magnetic Characterization and Delamination of Cr_2C MXenes

The work in this dissertation on the synthesis of Cr_2C MXenes is a major first step in ascertaining the predicted magnetic properties of this MXene material. While the synthesis process was quite successful, it is important to do more work in verifying the magnetism of the synthesized Cr_2C MXenes. The figure presented in Fig 2.9 has a number of ambiguities that will be necessary to clear up. If Cr_2C is indeed ferromagnetic as predicted from literature, this will make it a very attractive material as a magnetic ceramic metal.

In addition, it is important to work more on separating the synthesized Cr_2C into nanosheets or few layer sheets. A method that is common in the 2D synthesis world is tape exfoliation method. However, other options would be appropriate such as dispersing it in a surfactant using electrolysis.

5.2.2. Understanding the pinning effect on domain walls through atomistic and micromagnetic simulations

The use of DW-MTJs in circuit applications is still quite limited because of the variability of the DW motions and pinning. Introducing notches tend to increase their operational current but does not guarantee that the DW will move all the way across the track without stopping if the force from the depinning current is not strong enough. Also, for extremely scaled wires, fringe field from the pinned edges exert a repulsive force on the DW that contributes to the unpredictability. It is therefore important to study how the different anisotropies that arise from the lattice imperfections in the ferromagnet can contribute to the DW motion and what are the best ways to go around this.

5.2.3. Circuit simulation of unsupervised learning with MTJ synapses and neurons

In section 4.4 I discuss my ongoing work on using the MTJ synapses that I modelled in a real-time machine learning task. It would be necessary to use this as a template for a Python – SPICE library for machine learning hardware research and other further neuromorphic computing research with MTJs. While I used BindsNET as my spiking neural network python toolbox, I think that the BindsNET framework still needs a lot of improvement. So future work will entail customizing this toolbox and making it applicable for custom datasets and applications.

5.2.4. Fabrication and electrical characterization of MTJ synapse and neurons in a spiking neural network architecture.

While it is important to do a number of circuit and micromagnetic simulations to understand the behavior of proposed models, it is necessary that these models are fabricated and experimentally tested. Work needs to be done in

fabricating the synapse model that was proposed in chapter 4 and tested in a crossbar array. This would pave the way to a fully neuromorphic MTJ circuit in hand.

References

[1] P. A. M. Dirac. On the theory of quantum mechanics. *Proc. R. Soc. London. Ser. A, Contain. Pap. a Math. Phys. Character* **112,** 661–677 (1926).

[2] N. D. Mermin & H. Wagner. Absence of ferromagnetism or antiferromagnetism in one- or two-dimensional isotropic Heisenberg models. *Phys. Rev. Lett.* **17,** 1133–1136 (1966).

[3] C. Gong & X. Zhang. Two-dimensional magnetic crystals and emergent heterostructure devices. *Science (80-.).* **363,** (2019).

[4] B. Uchoa, V. N. Kotov, N. M. R. Peres & A. H. Castro Neto. Localized magnetic states in graphene. *Phys. Rev. Lett.* **101,** 026805 (2008).

[5] H. González-Herrero, J. M. Gómez-Rodríguez, P. Mallet, M. Moaied, J. J. Palacios, C. Salgado, M. M. Ugeda, J. Y. Veuillen, F. Yndurain & I. Brihuega. Atomic-scale control of graphene magnetism using hydrogen atoms. *arXiv* **352,** 437–442 (2020).

[6] O. V. Yazyev & L. Helm. Defect-induced magnetism in graphene. *Phys. Rev. B - Condens. Matter Mater. Phys.* **75,** 1–5 (2007).

[7] K. M. McCreary, A. G. Swartz, W. Han, J. Fabian & R. K. Kawakami. Magnetic moment formation in graphene detected by scattering of pure spin currents. *Phys. Rev. Lett.* **109,** 186604 (2012).

[8] J. Červenka, M. I. Katsnelson & C. F. J. Flipse. Room-temperature ferromagnetism in graphite driven by two-dimensional networks of pointdefects. *Nat. Phys.* **5,** 840–844 (2009).

[9] M. M. Ugeda, I. Brihuega, F. Guinea & J. M. Gómez-Rodríguez. Missing atom as a source of carbon magnetism. *Phys. Rev. Lett.* **104,** 096804 (2010).

[10] H. González-Herrero, J. M. Gómez-Rodríguez, P. Mallet, M. Moaied, J. J. Palacios, C. Salgado, M. M. Ugeda, J. Y. Veuillen, F. Yndurain & I. Brihuega. Atomic-scale control of graphene magnetism by using hydrogen atoms. *Science (80-.).* **352,** 437–441 (2016).

[11] R. R. Nair, I. L. Tsai, M. Sepioni, O. Lehtinen, J. Keinonen, A. V. Krasheninnikov, A. H. Castro Neto, M. I. Katsnelson, A. K. Geim & I. V. Grigorieva. Dual origin of defect magnetism in graphene and its reversible switching by molecular doping. *Nat. Commun.* **4,** 1–6 (2013).

[12] J. Červenka, M. I. Katsnelson & C. F. J. Flipse. Room-temperature ferromagnetism in graphite driven by two-dimensional networks of pointdefects. *Nat. Phys.* **5,** 840–844 (2009).

[13] K. M. McCreary, A. G. Swartz, W. Han, J. Fabian & R. K. Kawakami. Magnetic moment formation in graphene detected by scattering of pure spin currents. *Phys.*

Rev. Lett. **109,** 1–5 (2012).

[14] R. R. Nair, I. L. Tsai, M. Sepioni, O. Lehtinen, J. Keinonen, A. V. Krasheninnikov, A. H. Castro Neto, M. I. Katsnelson, A. K. Geim & I. V. Grigorieva. Dual origin of defect magnetism in graphene and its reversible switching by molecular doping. *Nat. Commun.* **4,** (2013).

[15] C. Gong, L. Li, Z. Li, H. Ji, A. Stern, Y. Xia, T. Cao, W. Bao, C. Wang, Y. Wang, Z. Q. Qiu, R. J. Cava, S. G. Louie, J. Xia & X. Zhang. Discovery of intrinsic ferromagnetism in two-dimensional van der Waals crystals. *Nature* **546,** 265–269 (2017).

[16] B. Huang, G. Clark, E. Navarro-Moratalla, D. R. Klein, R. Cheng, K. L. Seyler, Di. Zhong, E. Schmidgall, M. A. McGuire, D. H. Cobden, W. Yao, D. Xiao, P. Jarillo-Herrero & X. Xu. Layer-dependent ferromagnetism in a van der Waals crystal down to the monolayer limit. *Nature* **546,** 270–273 (2017).

[17] J. L. Lado & J. Fernández-Rossier. On the origin of magnetic anisotropy in two dimensional CrI 3. *2D Mater.* **4,** 035002 (2017).

[18] M. A. McGuire, H. Dixit, V. R. Cooper & B. C. Sales. Coupling of crystal structure and magnetism in the layered, ferromagnetic insulator cri3. *Chem. Mater.* **27,** 612–620 (2015).

[19] Z. Wang, I. Gutiérrez-Lezama, N. Ubrig, M. Kroner, M. Gibertini, T. Taniguchi, K. Watanabe, A. Imamoğlu, E. Giannini & A. F. Morpurgo. Very large tunneling magnetoresistance in layered magnetic semiconductor CrI3. *Nat. Commun.* **9,** (2018).

[20] L. D. Casto, A. J. Clune, M. O. Yokosuk, J. L. Musfeldt, T. J. Williams, H. L. Zhuang, M. W. Lin, K. Xiao, R. G. Hennig, B. C. Sales, J. Q. Yan & D. Mandrus. Strong spin-lattice coupling in CrSiTe3. *APL Mater.* **3,** (2015).

[21] H. L. Zhuang, Y. Xie, P. R. C. Kent & P. Ganesh. Computational discovery of ferromagnetic semiconducting single-layer CrSnTe3. *Phys. Rev. B - Condens. Matter Mater. Phys.* **92,** 2–7 (2015).

[22] W. Chen, Z. Sun, Z. Wang, L. Gu, X. Xu, S. Wu & C. Gao. Direct observation of van der Waals stacking–dependent interlayer magnetism. *Science (80-.).* **366,** 983–987 (2019).

[23] S. Mondal, A. Midya, M. M. Patidar, V. Ganesan & P. Mandal. Magnetic and magnetocaloric properties of layered van der Waals CrCl3. *Appl. Phys. Lett.* **117,** 1–6 (2020).

[24] Z. Wang, M. Gibertini, D. Dumcenco, T. Taniguchi, K. Watanabe, E. Giannini & A. F. Morpurgo. Determining the phase diagram of atomically thin layered antiferromagnet CrCl3. *Nat. Nanotechnol.* **14,** 1116–1122 (2019).

[25] A. S. Ahmad, Y. Liang, M. Dong, X. Zhou, L. Fang, Y. Xia, J. Dai, X. Yan, X.

Yu, J. Dai, G. J. Zhang, W. Zhang, Y. Zhao & S. Wang. Pressure-driven switching of magnetism in layered CrCl3. *Nanoscale* **12,** 22935–22944 (2020).

[26] M. Abramchuk, S. Jaszewski, K. R. Metz, G. B. Osterhoudt, Y. Wang, K. S. Burch & F. Tafti. Controlling Magnetic and Optical Properties of the van der Waals Crystal CrCl3−xBrx via Mixed Halide Chemistry. *Adv. Mater.* **30,** 1–7 (2018).

[27] J. X. Zhu, M. Janoschek, D. S. Chaves, J. C. Cezar, T. Durakiewicz, F. Ronning, Y. Sassa, M. Mansson, B. L. Scott, N. Wakeham, E. D. Bauer & J. D. Thompson. Electronic correlation and magnetism in the ferromagnetic metal Fe3GeTe2. *Phys. Rev. B* **93,** 1–6 (2016).

[28] H. L. Zhuang, P. R. C. Kent & R. G. Hennig. Strong anisotropy and magnetostriction in the two-dimensional Stoner ferromagnet Fe3GeTe2. *Phys. Rev. B* **93,** 1–7 (2016).

[29] A. F. May, S. Calder, C. Cantoni, H. Cao & M. A. McGuire. Magnetic structure and phase stability of the van der Waals bonded ferromagnet Fe3-xGeTe2. *Phys. Rev. B* **93,** 1–11 (2016).

[30] J. Yi, H. Zhuang, Q. Zou, Z. Wu, G. Cao, S. Tang, S. A. Calder, P. R. C. Kent, D. Mandrus & Z. Gai. Competing antiferromagnetism in a quasi-2D itinerant ferromagnet: Fe3GeTe2. *2D Mater.* **4,** (2017).

[31] Y. Deng, Y. Yu, Y. Song, J. Zhang, N. Z. Wang, Z. Sun, Y. Yi, Y. Z. Wu, S. Wu, J. Zhu, J. Wang, X. H. Chen & Y. Zhang. Gate-tunable room-temperature ferromagnetism in two-dimensional Fe3GeTe2. *Nature* **563,** 94–99 (2018).

[32] Z. Fei, B. Huang, P. Malinowski, W. Wang, T. Song, J. Sanchez, W. Yao, D. Xiao, X. Zhu, A. F. May, W. Wu, D. H. Cobden, J. H. Chu & X. Xu. Two-dimensional itinerant ferromagnetism in atomically thin Fe3GeTe2. *Nat. Mater.* **17,** 778–782 (2018).

[33] C. Tan, J. Lee, S. G. Jung, T. Park, S. Albarakati, J. Partridge, M. R. Field, D. G. McCulloch, L. Wang & C. Lee. Hard magnetic properties in nanoflake van der Waals Fe3GeTe2. *Nat. Commun.* **9,** 1–7 (2018).

[34] G. D. Nguyen, J. Lee, T. Berlijn, Q. Zou, S. M. Hus, J. Park, Z. Gai, C. Lee & A. P. Li. Visualization and manipulation of magnetic domains in the quasi-two-dimensional material F e3GeT e2. *Phys. Rev. B* **97,** 1–7 (2018).

[35] M. Naguib, M. Kurtoglu, V. Presser, J. Lu, J. Niu, M. Heon, L. Hultman, Y. Gogotsi & M. W. Barsoum. Two-dimensional nanocrystals produced by exfoliation of Ti3AlC2. *Adv. Mater.* **23,** 4248–4253 (2011).

[36] B. Anasori, M. R. Lukatskaya & Y. Gogotsi. 2D metal carbides and nitrides (MXenes) for energy storage. *Nat. Rev. Mater.* **2,** (2017).

[37] M. Ghidiu, M. R. Lukatskaya, M. Q. Zhao, Y. Gogotsi & M. W. Barsoum. Conductive two-dimensional titanium carbide ‘clay’ with high volumetric

capacitance. *Nature* **516,** 78–81 (2015).

[38] Y. Dall'Agnese, P. L. Taberna, Y. Gogotsi & P. Simon. Two-dimensional vanadium carbide (MXene) as positive electrode for sodium-ion capacitors. *J. Phys. Chem. Lett.* **6,** 2305–2309 (2015).

[39] Y. W. Cheng, J. H. Dai, Y. M. Zhang & Y. Song. Transition metal modification and carbon vacancy promoted Cr2CO2 (MXenes): a new opportunity for a highly active catalyst for the hydrogen evolution reaction. *J. Mater. Chem. A* **6,** 20956–20965 (2018).

[40] X. Zou, G. Li, Q. Wang, D. Tang, B. Wu & X. Wang. Energy storage properties of selectively functionalized Cr-group MXenes. *Comput. Mater. Sci.* **150,** 236–243 (2018).

[41] A. Yadav, A. Dashora, N. Patel, A. Miotello, M. Press & D. C. Kothari. Study of 2D MXene Cr 2 C material for hydrogen storage using density functional theory. *Appl. Surf. Sci.* **389,** 88–95 (2016).

[42] S. Sun, C. Liao, A. M. Hafez, H. Zhu & S. Wu. Two-dimensional MXenes for energy storage. *Chem. Eng. J.* **338,** 27–45 (2018).

[43] D. Sun, Q. Hu, J. Chen, X. Zhang, L. Wang, Q. Wu & A. Zhou. Structural Transformation of MXene (V2C, Cr2C, and Ta2C) with O Groups during Lithiation: A First-Principles Investigation. *ACS Appl. Mater. Interfaces* **8,** 74–81 (2016).

[44] Á. Morales-García, A. Fernández-Fernández, F. Viñes & F. Illas. CO2 abatement using two-dimensional MXene carbides. *J. Mater. Chem. A* **6,** 3381–3385 (2018).

[45] B. Anasori, Y. Xie, M. Beidaghi, J. Lu, B. C. Hosler, L. Hultman, P. R. C. Kent, Y. Gogotsi & M. W. Barsoum. Two-Dimensional, Ordered, Double Transition Metals Carbides (MXenes). *ACS Nano* **9,** 9507–9516 (2015).

[46] C. Si, J. Zhou & Z. Sun. Half-Metallic Ferromagnetism and Surface Functionalization-Induced Metal-Insulator Transition in Graphene-like Two-Dimensional Cr<inf>2</inf>C Crystals. *ACS Appl. Mater. Interfaces* **7,** 17510–17515 (2015).

[47] H. J. M. Swagten & P. V. Paluskar. Magnetic Tunnel Junctions. *Ref. Modul. Mater. Sci. Mater. Eng.* 2–7 (2016). doi:10.1016/b978-0-12-803581-8.01710-0

[48] E. Y. Tsymbal, O. N. Mryasov & P. R. LeClair. Spin-dependent tunnelling in magnetic tunnel junctions. *J. Phys. Condens. Matter* **15,** (2003).

[49] A. Sengupta, Y. Shim & K. Roy. Proposal for an all-spin artificial neural network: Emulating neural and synaptic functionalities through domain wall motion in ferromagnets. *IEEE Trans. Biomed. Circuits Syst.* **10,** 1152–1160 (2016).

[50] D. E. Nikonov & I. A. Young. Overview of beyond-CMOS devices and a uniform

methodology for their benchmarking. *Proc. IEEE* **101,** 2498–2533 (2013).

[51] G. S. D. Beach, M. Tsoi & J. L. Erskine. Current-induced domain wall motion. *J. Magn. Magn. Mater.* **320,** 1272–1281 (2008).

[52] S. Manipatruni, D. E. Nikonov, R. Ramesh, H. Li & I. A. Young. Spin-Orbit Logic with Magnetoelectric Nodes: A Scalable Charge Mediated Nonvolatile Spintronic Logic. 1–60 (2015). doi:10.1038/nmat4566

[53] J. Yu, X. Qiu, Y. Wu, J. Yoon, P. Deorani, J. M. Besbas, A. Manchon & H. Yang. Spin orbit torques and Dzyaloshinskii-Moriya interaction in dual-interfaced Co-Ni multilayers. *Sci. Rep.* **6,** 1–23 (2016).

[54] A. Brataas & K. M. D. Hals. Spin-orbit torques in action. *Nat. Nanotechnol.* **9,** 86–88 (2014).

[55] S. Fukami & H. Ohno. Perspective: Spintronic synapse for artificial neural network. *J. Appl. Phys.* **124,** (2018).

[56] J. Hsu. IBM's new brain [News]. *IEEE Spectr.* **51,** 17–19 (2014).

[57] B. Sengupta & M. B. Stemmler. Power consumption during neuronal computation. *Proc. IEEE* **102,** 738–750 (2014).

[58] L. F. Abbott & W. G. Regehr. Synaptic computation. *Nature* **431,** 796–803 (2004).

[59] W. Gerstner, W. M. Kistler, R. Naud & L. Paninski. *Neuronal Dynamics: From Single Neurons to Networks and Models of Cognition*. (Cambridge University Press, 2014).

[60] M. Foster & C. S. Sherrington. *Textbook of Physiology, Part 3*. (Macmillan and Co., Limited, 1897).

[61] F. Attneave, M. B. & D. O. Hebb. *The Organization of Behavior; A Neuropsychological Theory*. *The American Journal of Psychology* **63,** (John Wiley & Sons, Inc, 2006).

[62] I. S. Freiman. *Conditioned Reflexes and Neuron Organization*. *American Journal of Psychotherapy* **4,** (Cambridge University Press, 2018).

[63] L. A. O'Tuama & P. R. Jolles. The developing brain. *Pediatr. PET Imaging* **267,** 323–333 (2006).

[64] G. W. Burr, R. M. Shelby, A. Sebastian, S. Kim, S. Kim, S. Sidler, K. Virwani, M. Ishii, P. Narayanan, A. Fumarola, L. L. Sanches, I. Boybat, M. Le Gallo, K. Moon, J. Woo, H. Hwang & Y. Leblebici. Neuromorphic computing using non-volatile memory. *Adv. Phys. X* **2,** 89–124 (2017).

[65] S. Park, A. Sheri, J. Kim, J. Noh, J. Jang, M. Jeon, B. Lee, B. R. Lee, B. H. Lee & H. Hwang. Neuromorphic speech systems using advanced ReRAM-based synapse. *Tech. Dig. - Int. Electron Devices Meet. IEDM* 625–628 (2013). doi:10.1109/IEDM.2013.6724692

[66] M. J. Lee, G. S. Park, D. H. Seo, S. M. Kwon, H. J. Lee, J. S. Kim, M. Jung, C. Y. You, H. Lee, H. G. Kim, S. B. Pang, S. Seo, H. Hwang & S. K. Park. Reliable Multivalued Conductance States in TaO x Memristors through Oxygen Plasma-Assisted Electrode Deposition with in Situ-Biased Conductance State Transmission Electron Microscopy Analysis. *ACS Appl. Mater. Interfaces* **10,** 29757–29765 (2018).

[67] M. Suri, O. Bichler, D. Querlioz, O. Cueto, L. Perniola, V. Sousa, D. Vuillaume, C. Gamrat & B. DeSalvo. Phase change memory as synapse for ultra-dense neuromorphic systems: Application to complex visual pattern extraction. *2011 Int. Electron Devices Meet.* 4.4.1-4.4.4 (2011). doi:10.1109/IEDM.2011.6131488

[68] M.-W. Kwon, S. Kim, M.-H. Kim, J. Park, H. Kim, S. Hwang & B.-G. Park. Integrate-and-Fire (I&F) Neuron Circuit Using Resistive-Switching Random Access Memory (RRAM). *J. Nanosci. Nanotechnol.* **17,** 3038–3041 (2017).

[69] T. Chang, S. H. Jo & W. Lu. Short-term memory to long-term memory transition in a nanoscale memristor. *ACS Nano* **5,** 7669–7676 (2011).

[70] S. La Barbera, D. Vuillaume & F. Alibart. Filamentary switching: Synaptic plasticity through device volatility. *ACS Nano* **9,** 941–949 (2015).

[71] C. H. Bennett, S. La Barbera, A. F. Vincent, J. O. Klein, F. Alibart & D. Querlioz. Exploiting the short-term to long-term plasticity transition in memristive nanodevice learning architectures. *Proc. Int. Jt. Conf. Neural Networks* **2016-Octob,** 947–954 (2016).

[72] C. Du, F. Cai, M. A. Zidan, W. Ma, S. H. Lee & W. D. Lu. Reservoir computing using dynamic memristors for temporal information processing. *Nat. Commun.* **8,** 1–10 (2017).

[73] J. J. Kan, C. Park, C. Ching, J. Ahn, L. Xue, R. Wang, A. Kontos, S. Liang, M. Bangar, H. Chen, S. Hassan, S. Kim, M. Pakala & S. H. Kang. Systematic validation of 2x nm diameter perpendicular MTJ arrays and MgO barrier for sub-10 nm embedded STT-MRAM with practically unlimited endurance. *Tech. Dig. - Int. Electron Devices Meet. IEDM* 27.4.1-27.4.4 (2017). doi:10.1109/IEDM.2016.7838493

[74] J. Torrejon, M. Riou, F. A. Araujo, S. Tsunegi, G. Khalsa, D. Querlioz, P. Bortolotti, V. Cros, K. Yakushiji, A. Fukushima, H. Kubota, S. Yuasa, M. D. Stiles & J. Grollier. Neuromorphic computing with nanoscale spintronic oscillators. *Nature* **547,** 428–431 (2017).

[75] A. Antonyan, S. Pyo, H. Jung & T. Song. Embedded MRAM Macro for eFlash Replacement. *Proc. - IEEE Int. Symp. Circuits Syst.* **2018-May,** 2–5 (2018).

[76] D. E. Nikonov & I. A. Young. Benchmarking of Beyond-CMOS Exploratory Devices for Logic Integrated Circuits. *IEEE J. Explor. Solid-State Comput. Devices Circuits* **1,** 3–11 (2015).

[77] D. Zhang, L. Zeng, Y. Qu, Y. Zhang, M. Wang, W. Zhao, T. Tang & Y. Wang. Energy-efficient neuromorphic computation based on compound spin synapse with stochastic learning. *Proc. - IEEE Int. Symp. Circuits Syst.* **2015-July,** 1538–1541 (2015).

[78] J. A. Currivan-Incorvia, S. Siddiqui, S. Dutta, E. R. Evarts, J. Zhang, D. Bono, C. A. Ross & M. A. Baldo. Logic circuit prototypes for three-terminal magnetic tunnel junctions with mobile domain walls. *Nat. Commun.* **7,** 1–7 (2016).

[79] S. Lequeux, J. Sampaio, V. Cros, K. Yakushiji, A. Fukushima, R. Matsumoto, H. Kubota, S. Yuasa & J. Grollier. A magnetic synapse: Multilevel spin-torque memristor with perpendicular anisotropy. *Sci. Rep.* **6,** 1–7 (2016).

[80] J. Grollier, D. Querlioz & M. D. Stiles. Spintronic Nanodevices for Bioinspired Computing. *Proc. IEEE* **104,** 2024–2039 (2016).

[81] A. Sengupta & K. Roy. Encoding neural and synaptic functionalities in electron spin: A pathway to efficient neuromorphic computing. *Appl. Phys. Rev.* **4,** (2017).

[82] N. Hassan, X. Hu, L. Jiang-Wei, F. Garcia-Sanchez, M. Pasquale, O. G. Akinola, C. H. Bennett, N. Hassan, J. A. C. Incorvia, W. H. Brigner & J. S. Friedman. Magnetic domain wall neuron with lateral inhibition. *J. Appl. Phys.* **124,** 152127 (2018).

[83] S. Lequeux, J. Sampaio, V. Cros, K. Yakushiji, A. Fukushima, R. Matsumoto, H. Kubota, S. Yuasa & J. Grollier. A magnetic synapse: Multilevel spin-torque memristor with perpendicular anisotropy. *Sci. Rep.* **6,** (2016).

[84] J. Torrejon, M. Riou, F. A. Araujo, S. Tsunegi, G. Khalsa, D. Querlioz, P. Bortolotti, V. Cros, K. Yakushiji, A. Fukushima, H. Kubota, S. Yuasa, M. D. Stiles & J. Grollier. Neuromorphic computing with nanoscale spintronic oscillators. *Nature* **547,** 428–431 (2017).

[85] N. K. Upadhyay, H. Jiang, Z. Wang, S. Asapu, Q. Xia & J. Joshua Yang. Emerging Memory Devices for Neuromorphic Computing. *Adv. Mater. Technol.* **1800589,** 1–13 (2019).

[86] V. Calayir & L. Pileggi. All-magnetic analog associative memory. *2013 IEEE 11th Int. New Circuits Syst. Conf. NEWCAS 2013* 1–4 (2013). doi:10.1109/NEWCAS.2013.6573563

[87] G. Bi & M. Poo. Synaptic Modification by Correlated Activity: Hebb's Postulate Revisited. *Annu. Rev. Neurosci.* **24,** 139–166 (2002).

[88] H. Markram, W. Gerstner & P. J. Sjöström. Spike-Timing-Dependent Plasticity: A Comprehensive Overview. *Front. Synaptic Neurosci.* **4,** 2–5 (2012).

[89] B. Anasori, M. R. Lukatskaya & Y. Gogotsi. 2D metal carbides and nitrides (MXenes) for energy storage. *Nat. Rev. Mater.* **2,** (2017).

[90] B. M. Jun, S. Kim, J. Heo, C. M. Park, N. Her, M. Jang, Y. Huang, J. Han & Y. Yoon. Review of MXenes as new nanomaterials for energy storage/delivery and selected environmental applications. *Nano Res.* **12,** 471–487 (2019).

[91] X. Sang, Y. Xie, M. W. Lin, M. Alhabeb, K. L. Van Aken, Y. Gogotsi, P. R. C. Kent, K. Xiao & R. R. Unocic. Atomic defects in monolayer titanium carbide (Ti3C2Tx) MXene. *ACS Nano* **10,** 9193–9200 (2016).

[92] M. Alhabeb, K. Maleski, B. Anasori, P. Lelyukh, L. Clark, S. Sin & Y. Gogotsi. Guidelines for Synthesis and Processing of Two-Dimensional Titanium Carbide (Ti3C2Tx MXene). *Chem. Mater.* **29,** 7633–7644 (2017).

[93] J.-C. Lei, X. Zhang & Z. Zhou. Recent advances in MXene: Preparation, properties, and applications. *Front. Phys.* **10,** 276–286 (2015).

[94] X. H. Wang & Y. C. Zhou. Layered Machinable and Electrically Conductive Ti2AlC and Ti3AlC2 Ceramics: a Review. *J. Mater. Sci. Technol.* **26,** 385–416 (2010).

[95] M. Wu, B. Wang, Q. Hu, L. Wang & A. Zhou. The synthesis process and thermal stability of V2C MXene. *Materials (Basel).* **11,** 8–11 (2018).

[96] K. Rajavel, T. Ke, K. Yang & D. Lin. Condition optimization for exfoliation of two dimensional titanium carbide (Ti 3 C 2 T x). *Nanotechnology* **29,** 095605 (2018).

[97] L. Li, G. Li, L. Tan, Y. Zhang & B. Wu. Highly Efficiently Delaminated Single-Layered MXene Nanosheets with Large Lateral Size. *Langmuir* **33,** 9000–9006 (2017).

[98] A. Feng, Y. Yu, Y. Wang, F. Jiang, Y. Yu, L. Mi & L. Song. Two-dimensional MXene Ti3C2produced by exfoliation of Ti3AlC2. *Mater. Des.* **114,** 161–166 (2017).

[99] W. M. Haynes, D. R. Lide & T. J. Bruno. *CRC Handbook of Chemistry and Physics: : A Ready-reference Book of Chemical and Physical Data*. (CRC Press, 2016).

[100] K. Huang, Z. Li, J. Lin, G. Han & P. Huang. Two-dimensional transition metal carbides and nitrides (MXenes) for biomedical applications. *Chem. Soc. Rev.* **47,** 5109–5124 (2018).

[101] J. Halim, S. Kota, M. R. Lukatskaya, M. Naguib, M. Q. Zhao, E. J. Moon, J. Pitock, J. Nanda, S. J. May, Y. Gogotsi & M. W. Barsoum. Synthesis and Characterization of 2D Molybdenum Carbide (MXene). *Adv. Funct. Mater.* **26,** 3118–3127 (2016).

[102] P. Urbankowski, B. Anasori, T. Makaryan, D. Er, S. Kota, P. L. Walsh, M. Zhao, V. B. Shenoy, M. W. Barsoum & Y. Gogotsi. Synthesis of two-dimensional titanium nitride Ti4N3 (MXene). *Nanoscale* **8,** 11385–11391 (2016).

[103] NIST X-ray Photoelectron Spectroscopy Database. *NIST Standard Reference Database Number 20* (2000). doi:10.18434/T4T88K

[104] Thermo Scientific. XPS Interpretation of Carbon. (2016). Available at: http://xpssimplified.com/elements/carbon.php. (Accessed: 25th February 2021)

[105] E. I. Zamulaeva, E. A. Levashov, E. A. Skryleva, T. A. Sviridova & P. V. Kiryukhantsev-Korneev. Conditions for formation of MAX phase Cr2AlC in electrospark coatings deposited onto titanium alloy. *Surf. Coatings Technol.* **298,** 15–23 (2016).

[106] D. B. Lee, T. D. Nguyen & S. W. Park. Corrosion of Cr 2AlC in Ar/1%SO 2 gas between 900 and 1200 °c. *Oxid. Met.* **75,** 313–323 (2011).

[107] A. Obrosov, R. Gulyaev, A. Zak, M. Ratzke, M. Naveed, W. Dudzinski & S. Weiß. Chemical and morphological characterization of magnetron sputtered at different bias voltages Cr-Al-C coatings. *Materials (Basel).* **10,** 1–16 (2017).

[108] I. Grohmann, E. Kemnitz, A. Lippitz & W. E. S. Unger. Curve fitting of Cr 2p photoelectron spectra of Cr2O3 and CrF3. *Surf. Interface Anal.* **23,** 887–891 (1995).

[109] Z. M. Khamdokhov, Z. K. Kalazhokov, R. S. Teshev & K. H. Kalazhokov. Chromium-Nickel Alloy for the Synthesis of Carbon Nanoparticles. *Nano Hybrids Compos.* **28,** 123–129 (2020).

[110] S. Ma, J. Ye, A. Liu, Y. Liu, J. Wang, J. Pang & I. Reimanis. Synthesis, Characterization, and Consolidation of Cr2(C,N) Solid Solution Powders. *J. Am. Ceram. Soc.* **99,** 1943–1950 (2016).

[111] S. M. Schmuecker, D. Clouser, T. J. Kraus & B. M. Leonard. Synthesis of metastable chromium carbide nanomaterials and their electrocatalytic activity for the hydrogen evolution reaction. *Dalt. Trans.* **46,** 13524–13530 (2017).

[112] Electronic Supplementary Material (ESI) for Dalton Transactions . This journal is © The Royal Society of Chemistry 2017 Synthesis of Metastable Chromium Carbide Nanomaterials and their Electrocatalytic Activity for the Hydrogen Evolution Reaction Samant. (2017).

[113] E. Bouzy, E. Bauer-Grosse & G. Le Caër. Naci and filled re3b-type structures for two metastable chromium carbides. *Philos. Mag. B Phys. Condens. Matter; Stat. Mech. Electron. Opt. Magn. Prop.* **68,** 619–638 (1993).

[114] W. Jeitschko, H. Nowotny & F. Benesovsky. Carbon-containing ternary compounds (H-Phase). *Monatshefte für Chemie* **94,** 672–676 (1963).

[115] F. Z. Abderrahim, H. I. Faraoun & T. Ouahrani. Structure, bonding and stability of semi-carbides M 2C and sub-carbides M 4C (M=V, Cr, Nb, Mo, Ta, W): A first principles investigation. *Phys. B Condens. Matter* **407,** 3833–3838 (2012).

[116] M. A. Rouault, P. Herpin & M. R. Fruchart. Crystallographic study of carbides Cr7C3 and Mn7C2. *Ann. Chim. Fr.* (1970).

[117] A. Vansteenkiste, J. Leliaert, M. Dvornik, M. Helsen, F. Garcia-Sanchez & B. Van Waeyenberge. The design and verification of MuMax3. *AIP Adv.* **4,** (2014).

[118] W. F. Brown. Some magnetostatic and micromagnetic properties of the infinite rectangular bar. *J. Appl. Phys.* **35,** 2102–2106 (1964).

[119] A. Vansteenkiste, J. Leliaert, M. Dvornik, M. Helsen, F. Garcia-Sanchez & B. Van Waeyenberge. The design and verification of MuMax3. *AIP Adv.* **4,** (2014).

[120] A. N. Bogdanov & U. B. Rößler. Chiral symmetry breaking in magnetic thin films and multilayers. *Phys. Rev. Lett.* **87,** 37203-1-37203–4 (2001).

[121] S. Rohart & A. Thiaville. Skyrmion confinement in ultrathin film nanostructures in the presence of Dzyaloshinskii-Moriya interaction. *Phys. Rev. B - Condens. Matter Mater. Phys.* **88,** 1–8 (2013).

[122] S. Zhang & Z. Li. Roles of nonequilibrium conduction electrons on the magnetization dynamics of ferromagnets. *Phys. Rev. Lett.* **93,** 1–4 (2004).

[123] P. Gambardella. Introduction to spin torques and spin-orbit torques in metal layers. *Spinmechanics III* 87 (2015).

[124] J. Xiao, A. Zangwill & M. D. Stiles. Boltzmann test of Slonczewski's theory of spin-transfer torque. *Phys. Rev. B - Condens. Matter Mater. Phys.* **70,** 1–4 (2004).

[125] J. C. Slonczewski. Current-driven excitation of magnetic multilayers. *J. Magn. Magn. Mater.* **159,** L1–L7 (1996).

[126] K. Garello, I. M. Miron, C. O. Avci, F. Freimuth, Y. Mokrousov, S. Blügel, S. Auffret, O. Boulle, G. Gaudin & P. Gambardella. Symmetry and magnitude of spin-orbit torques in ferromagnetic heterostructures. *Nat. Nanotechnol.* **8,** 587–593 (2013).

[127] K. Garello, C. O. Avci, I. M. Miron, M. Baumgartner, A. Ghosh, S. Auffret, O. Boulle, G. Gaudin & P. Gambardella. Ultrafast magnetization switching by spin-orbit torques. *Appl. Phys. Lett.* **105,** (2014).

[128] S. Majumdar, H. S. Majumdar & R. Österbacka. Organic Spintronics. in *Comprehensive Nanoscience and Technology* 109–142 (Elsevier, 2011). doi:10.1016/B978-0-12-374396-1.00023-4

[129] N. S. Hosmane. Chapter 1 – Electronic Structure: Quantum Theory Revisited. *Adv. Inorg. Chem.* 3–13 (2017). doi:10.1016/B978-0-12-801982-5.00001-1

[130] J. A. Ricodeau. Magnetocrystalline Anisotropy and Spin-Orbit Coupling in Nonspherical Crystal Potentials. *Phys. Rev. B* **7,** 4950–4958 (1973).

[131] I. Dzyaloshinsky. A thermodynamic theory of 'weak' ferromagnetism of antiferromagnetics. *J. Phys. Chem. Solids* **4,** 241–255 (1958).

[132] T. Moriya. Anisotropic superexchange interaction and weak ferromagnetism. *Phys. Rev.* **120,** 91–98 (1960).

[133] P. M. Levy. Antisymmetric Exchange. *Phys. Rev. Lett.* **20,** 1366–1370 (1968).

[134] J. Pelzl, R. Meckenstock, D. Spoddig, F. Schreiber, J. Pflaum & Z. Frait. Spin-orbit-coupling effects on g-value and damping factor of the ferromagnetic resonance in Co and Fe films. *J. Phys. Condens. Matter* **15,** (2003).

[135] H. Ebert, A. Vernes & J. Banhart. Magnetoresistance, Anisotropic. *Encycl. Mater. Sci. Technol.* 5079–5083 (2001). doi:10.1016/b0-08-043152-6/00882-2

[136] T. R. Mcguire & R. I. Potter. Anisotropic Magnetoresistance in Ferromagnetic 3D Alloys. *IEEE Trans. Magn.* **11,** 1018–1038 (1975).

[137] N. Nagaosa, J. Sinova, S. Onoda, A. H. MacDonald & N. P. Ong. Anomalous Hall effect. *Rev. Mod. Phys.* **82,** 1539–1592 (2010).

[138] C. Z. Chang, J. Zhang, X. Feng, J. Shen, Z. Zhang, M. Guo, K. Li, Y. Ou, P. Wei, L. L. Wang, Z. Q. Ji, Y. Feng, S. Ji, X. Chen, J. Jia, X. Dai, Z. Fang, S. C. Zhang, K. He, *et al.* Experimental observation of the quantum anomalous Hall effect in a magnetic topological Insulator. *Science (80-.).* **340,** 167–170 (2013).

[139] M. I. D'Yakonov & V. I. Perel'. Possibility of Orienting Electron Spins with Current. *JETPL* **13,** 467 (1971).

[140] M. I. Dyakonov & V. I. Perel. Current-induced spin orientation of electrons in semiconductors. *Phys. Lett. A* **35,** 459–460 (1971).

[141] S. Murakami. Quantum spin hall effect and enhanced magnetic response by spin-orbit coupling. *Phys. Rev. Lett.* **97,** 1–4 (2006).

[142] J. Wunderlich, B. Kaestner, J. Sinova & T. Jungwirth. Experimental observation of the spin-hall effect in a two-dimensional spin-orbit coupled semiconductor system. *Phys. Rev. Lett.* **94,** 1–4 (2005).

[143] J. Sinova, D. Culcer, Q. Niu, N. A. Sinitsyn, T. Jungwirth & A. H. MacDonald. Universal intrinsic spin Hall effect. *Phys. Rev. Lett.* **92,** 1–4 (2004).

[144] Y. A. Bychkov & É. I. Rashba. Properties of a 2D electron gas with lifted spectral degeneracy. *JETPL* **39,** 78 (1984).

[145] E. I. Rashba & V. I. Sheka. Symmetry of Energy Bands in Crystals of Wurtzite Type II . Symmetry of Bands with Spin-Orbit Interaction Included Construction of double-valued irreducible representations. *Dtsch. Phys. Gesellschaft* **2,** 162–176 (1959).

[146] V. M. Edelstein. Spin polarization of conduction electrons induced by electric current in two-dimensional asymmetric electron systems. *Solid State Commun.* **73,** 233–235 (1990).

[147] J. C. R. Sánchez, L. Vila, G. Desfonds, S. Gambarelli, J. P. Attané, J. M. De

Teresa, C. Magén & A. Fert. Spin-to-charge conversion using Rashba coupling at the interface between non-magnetic materials. *Nat. Commun.* **4,** 1–7 (2013).

[148] J. C. Rojas-Sánchez, S. Oyarzún, Y. Fu, A. Marty, C. Vergnaud, S. Gambarelli, L. Vila, M. Jamet, Y. Ohtsubo, A. Taleb-Ibrahimi, P. Le Fèvre, F. Bertran, N. Reyren, J. M. George & A. Fert. Spin to Charge Conversion at Room Temperature by Spin Pumping into a New Type of Topological Insulator: α -Sn Films. *Phys. Rev. Lett.* **116,** 1–6 (2016).

[149] G. Dresselhaus. Spin-Orbit Coupling Effects in Zinc Blende Structures. *Phys. Rev.* **100,** 580–586 (1955).

[150] T. Gao & K. Ando. *Spin–orbit torques*. *Handbook of Magnetic Materials* **29,** (Elsevier B.V., 2020).

[151] A. Hirohata, K. Yamada, Y. Nakatani, L. Prejbeanu, B. Diény, P. Pirro & B. Hillebrands. Review on spintronics: Principles and device applications. *J. Magn. Magn. Mater.* **509,** (2020).

[152] K. Zhang, U. Bhattacharya, Z. Chen, F. Hamzaoglu, D. Murray, N. Vallepalli, Y. Wang, B. Zheng & M. Bohr. SRAM design on 65-nm CMOS technology with dynamic sleep transistor for leakage reduction. *Solid-State Circuits, IEEE J.* **40,** 895–901 (2005).

[153] F. Tachibana, O. Hirabayashi, Y. Takeyama, M. Shizuno, A. Kawasumi, K. Kushida, A. Suzuki, Y. Niki, S. Sasaki, T. Yabe & Y. Unekawa. A 27% Active and 85% Standby Power Reduction in Dual-Power-Supply SRAM Using BL Power Calculator and Digitally Controllable Retention Circuit. *IEEE J. Solid-State Circuits* **49,** 118–126 (2014).

[154] R. Likamwa, Y. Hou, Y. Gao, M. Polansky & L. Zhong. RedEye: Analog ConvNet Image Sensor Architecture for Continuous Mobile Vision. *Proc. - 2016 43rd Int. Symp. Comput. Archit. ISCA 2016* 255–266 (2016). doi:10.1109/ISCA.2016.31

[155] D. Ielmini & H. S. P. Wong. In-memory computing with resistive switching devices. *Nat. Electron.* **1,** 333–343 (2018).

[156] B. Wang, Z. Wang, A. Du, Y. Qiang, K. Cao, Y. Zhao, H. Zheng, S. Yan, P. Zhai, J. Liu, G. Guo, Y. Bai, J. Wang & W. Zhao. Radiation impact of swift heavy ion beams on double-interface CoFeB/MgO magnetic tunnel junctions. *Appl. Phys. Lett.* **116,** 172401 (2020).

[157] I. P. Radu, O. Zografos, A. Vaysset, F. Ciubotaru, J. Yan, J. Swerts, D. Radisic, B. Briggs, B. Soree, M. Manfrini, M. Ercken, C. Wilson, P. Raghavan, S. Sayan, C. Adelmann, A. Thean, L. Amaru, P. E. Gaillardon, G. De Micheli, *et al.* Spintronic majority gates. *Tech. Dig. - Int. Electron Devices Meet. IEDM* **2016-Febru,** 32.5.1-32.5.4 (2015).

[158] D. E. Nikonov, G. I. Bourianoff & T. Ghani. Proposal of a spin torque majority

gate logic. *IEEE Electron Device Lett.* **32,** 1128–1130 (2011).

[159] Z. Luo, A. Hrabec, T. P. Dao, G. Sala, S. Finizio, J. Feng, S. Mayr, J. Raabe, P. Gambardella & L. J. Heyderman. Current-driven magnetic domain-wall logic. *Nature* **579,** 214–218 (2020).

[160] D. Morris, D. Bromberg, J.-G. J.-. G. J. Zhu & L. Pileggi. mLogic: Ultra-low voltage non-volatile logic circuits using STT-MTJ devices. *Proc. 49th Annu. Des. Autom. Conf.* 486–491 (2012).

[161] V. Sokalski, D. M. Bromberg, D. Morris, M. T. Moneck, E. Yang, L. Pileggi & J.-G.-. G. Zhu. Naturally Oxidized FeCo as a Magnetic Coupling Layer for Electrically Isolated Read/Write Paths in mLogic. *IEEE Trans. Magn.* **49,** 4351–4354 (2013).

[162] D. M. Bromberg, M. T. Moneck, V. M. Sokalski, J. Zhu, L. Pileggi & J. G. Zhu. Experimental demonstration of four-terminal magnetic logic device with separate read- and write-paths. *Tech. Dig. - Int. Electron Devices Meet. IEDM* **2015-Febru,** 33.1.1-33.1.4 (2015).

[163] D. M. Bromberg, J. Zhu, L. Pileggi, V. Sokalski, M. Moneck & P. C. Richardson. (12) United States Patent. **2,**

[164] J. G. J. Zhu, D. M. Bromberg, M. Moneck, V. Sokalski & L. Pileggi. MLogic: All spin logic device and circuits. *2015 4th Berkeley Symp. Energy Effic. Electron. Syst. E3S 2015 - Proc.* 1–2 (2015). doi:10.1109/E3S.2015.7336781

[165] J. A. Currivan, Y. Jang, M. D. Mascaro, M. A. Baldo & C. A. Ross. Low energy magnetic domain wall logic in short, narrow, ferromagnetic wires. *IEEE Magn. Lett.* **3,** (2012).

[166] J. A. Currivan, M. A. Baldo & C. A. Ross. (12) Patent Application Publication (10) Pub . No .: US 2013 / 0181158 A1. *US Pat.* **1,** 12–15 (2013).

[167] X. Hu, A. Timm, W. H. Brigner, J. A. C. Incorvia & J. S. Friedman. SPICE-only model for spin-transfer torque domain-wall MTJ logic. *IEEE Trans. Electron Devices* **66,** 2817–2821 (2019).

[168] T. Patrick Xiao, M. J. Marinella, C. H. Bennett, X. Hu, B. Feinberg, R. Jacobs-Gedrim, S. Agarwal, J. S. Brunhaver, J. S. Friedman & J. A. C. Incorvia. Energy and Performance Benchmarking of a Domain Wall-Magnetic Tunnel Junction Multibit Adder. *IEEE J. Explor. Solid-State Comput. Devices Circuits* **5,** 188–196 (2019).

[169] J. A. Currivan-Incorvia, S. Siddiqui, S. Dutta, E. R. Evarts, C. A. Ross & M. A. Baldo. Spintronic logic circuit and device prototypes utilizing domain walls in ferromagnetic wires with tunnel junction readout. *2015 IEEE Int. Electron Devices Meet.* 32–36 (2015).

[170] D. Wan, M. Manfrini, A. Vaysset, L. Souriau, L. Wouters, A. Thiam, E.

Raymenants, S. Sayan, J. Jussot, J. Swerts, S. Couet, N. Rassoul, K. B. Gavan, K. Paredis, C. Huyghebaert, M. Ercken, C. J. Wilson, D. Mocuta & I. P. Radu. Fabrication of magnetic tunnel junctions connected through a continuous free layer to enable spin logic devices. *Jpn. J. Appl. Phys.* **57,** (2018).

[171] J. A. Currivan, Y. Jang, M. D. Mascaro, M. A. Baldo & C. A. Ross. Low Energy Magnetic Domain Wall Logic in Short, Narrow, Ferromagnetic Wires. *IEEE Magn. Lett.* **3,** 3000104 (2012).

[172] O. Akinola, X. Hu, C. H. Bennett, M. Marinella, J. S. Friedman & J. A. C. Incorvia. Three-terminal magnetic tunnel junction synapse circuits showing spike-timing-dependent plasticity. *J. Phys. D. Appl. Phys.* **52,** (2019).

[173] C. Cui, O. G. Akinola, N. Hassan, C. H. Bennett, M. J. Marinella, J. S. Friedman & J. A. C. Incorvia. Maximized lateral inhibition in paired magnetic domain wall racetracks for neuromorphic computing. *Nanotechnology* **31,** (2020).

[174] S. A. Siddiqui, S. Dutta, A. Tang, L. Liu, C. A. Ross & M. A. Baldo. Magnetic domain wall based synaptic and activation function generator for neuromorphic accelerators. *Nano Lett.* (2019). doi:10.1021/acs.nanolett.9b04200

[175] G. Zahnd, V. T. Pham, A. Marty, M. Jamet, C. Beigné, L. Notin, C. Vergnaud, F. Rortais, L. Vila & J. P. Attané. Introduction and pinning of domain walls in 50 nm NiFe constrictions using local and external magnetic fields. *J. Magn. Magn. Mater.* **406,** 166–170 (2016).

[176] S. F. Zhang, W. L. Gan, J. Kwon, F. L. Luo, G. J. Lim, J. B. Wang & W. S. Lew. Highly Efficient Domain Walls Injection in Perpendicular Magnetic Anisotropy Nanowire. *Sci. Rep.* **6,** 1–8 (2016).

[177] L. Xue, C. Ching, A. Kontos, J. Ahn, X. Wang, R. Whig, H. W. Tseng, J. Howarth, S. Hassan, H. Chen, M. Bangar, S. Liang, R. Wang & M. Pakala. Process optimization of perpendicular magnetic tunnel junction arrays for last-level cache beyond 7 nm node. *Dig. Tech. Pap. - Symp. VLSI Technol.* **2018-June,** 117–118 (2018).

[178] P. Jadaun, C. Cui & J. A. C. Incorvia. Design of self-adaptive oscillating neurons using electrically reconfigurable skyrmion lattices. 1–12 (2020).

[179] M. Alamdar, T. Leonard, C. Cui, B. P. Rimal, L. Xue, O. G. Akinola, T. Patrick Xiao, J. S. Friedman, C. H. Bennett, M. J. Marinella & J. A. C. Incorvia. Domain wall-magnetic tunnel junction spin–orbit torque devices and circuits for in-memory computing. *Appl. Phys. Lett.* **118,** 112401 (2021).

[180] N. Nuntalid. Evolving Probabilistic Spiking Neural Networks for Modelling and Pattern Recognition of Spatio-temporal Data on the Case Study of Electroencephalography (EEG) Brain Data Evolving Probabilistic Spiking Neural Networks for Modelling and Pattern Recognitio. (2012).

[181] W. Maass. Networks of spiking neurons: The third generation of neural network models. *Neural Networks* **10,** 1659–1671 (1997).

[182] Intel. Neuromorphic Computing - Next Generation of AI. 1–1 (2019). Available at: https://www.intel.com/content/www/us/en/research/neuromorphic-computing.html. (Accessed: 29th March 2021)

[183] C. Mead. Neuromorphic Electronic Systems. *Proc. IEEE* **78,** 1629–1636 (1990).

[184] C. S. Herrmann, S. Rach, T. Neuling & D. Strüber. Transcranial alternating current stimulation: a review of the underlying mechanisms and modulation of cognitive processes. *Front. Hum. Neurosci.* **7,** 671–675 (2013).

[185] W. H. Brigner, N. Hassan, X. Hu, L. Jiang-Wei, O. G. Akinola, F. Garcia-Sanchez, M. Pasquale, C. H. Bennett, J. A. C. Incorvia & J. S. Friedman. Magnetic domain wall neuron with intrinsic leaking and lateral inhibition capability. in *Spintronics XII* (eds. Drouhin, H.-J. M., Wegrowe, J.-E. & Razeghi, M.) 128 (SPIE, 2019). doi:10.1117/12.2528218

[186] W. H. Brigner, X. Hu, N. Hassan, C. H. Bennett, J. A. C. Incorvia, F. Garcia-Sanchez & J. S. Friedman. Graded-Anisotropy-Induced Magnetic Domain Wall Drift for an Artificial Spintronic Leaky Integrate-and-Fire Neuron. *IEEE J. Explor. Solid-State Comput. Devices Circuits* **5,** 1–1 (2019).

[187] C. Cui, O. G. Akinola, N. Hassan, H. Christopher, M. J. Marinella, J. S. Friedman & J. A. C. Maximized Lateral Inhibition in Paired Magnetic Domain Wall Racetracks for Neuromorphic Computing. *ArXiv e-prints* 1–8 (2019).

[188] M. H. Hennig. Modeling synaptic transmission. *N Week - ANC, Informatics, Univ. Edinburgh* **4,** 1–18 (2008).

[189] James Sneyd; R Bertram; Mathematical Biosciences Institute at the Ohio State University. *Tutorials in Mathematical Biosciences II: Mathematical Modeling of Calcium Dynamics and Signal Transduction*. *Springer e-books* **1867,** (Springer, 2005).

[190] M. L. Dustin, C. T. Baldari, K. I. Jankowska, J. K. Burkhardt, N. Blas-Rus, E. Bustos-Morán, F. Sánchez-Madrid, Martín-Cófreces, A. Hashimoto-Tane, T. Yokosuka, T. Saito, X. Su, J. A. Ditlev, M. K. Rosen, R. D. Vale, C. R. Nowosad, P. Tolar, E. Calleja, B. Alarcón, *et al. The Immune Synapse*. *Methods in Molecular Biology* **1584,** (2017).

[191] H. Z. Shouval & G. Kalantzis. Stochastic Properties of Synaptic Transmission Affect the Shape of Spike Time–Dependent Plasticity Curves. *J. Neurophysiol.* **93,** 1069–1073 (2004).

[192] H. Shouval. Spike timing dependent plasticity: a consequence of more fundamental learning rules. *Front. Comput. Neurosci.* **4,** 1–13 (2010).

[193] N. Frémaux & W. Gerstner. Neuromodulated Spike-Timing-Dependent Plasticity,

and Theory of Three-Factor Learning Rules. *Front. Neural Circuits* **9,** (2016).

[194] M. Graupner. Mechanisms of induction and maintenance of spike-timing dependent plasticity in biophysical synapse models. *Front. Comput. Neurosci.* **4,** 1–19 (2010).

[195] B. Porr, A. Saudargiene & F. Worgotter. Analytical solution of spike-timing dependent plasticity based on synaptic biophysics. *Adv. Neural Inf. Process. Syst.* (2004).

[196] X. Zhang. A Mathematical Model of a Neuron with Synapses based on Physiology. *Nat. Preced.* (2008). doi:10.1038/npre.2008.1703.1

[197] M. J. Donahue & D. G. Porter. *OOMMF user's guide, Version 1.0*. (2012).

[198] A. Sengupta & K. Roy. Neuromorphic computing enabled by physics of electron spins: Prospects and perspectives. *Appl. Phys. Express* **11,** (2018).

[199] M. Sharad, C. Augustine, G. Panagopoulos & K. Roy. Spin based neuron-synapse module for ultra low power programmable computational networks. *Proc. Int. Jt. Conf. Neural Networks* 10–15 (2012). doi:10.1109/IJCNN.2012.6252609

[200] L. Zeng, D. Zhang, Y. Zhang, F. Gong, T. Gao, S. Tu, H. Yu & W. Zhao. Spin wave based synapse and neuron for ultra low power neuromorphic computation system. *Proc. - IEEE Int. Symp. Circuits Syst.* **2016-July,** 918–921 (2016).

[201] A. Sebastian, S. Kim, A. Fumarola, S. Kim, J. Woo, L. L. Sanches, K. Virwani, P. Narayanan, S. Sidler, R. M. Shelby, I. Boybat, G. W. Burr, Y. Leblebici, M. Le Gallo, K. Moon, H. Hwang & M. Ishii. Neuromorphic computing using non-volatile memory. *Adv. Phys. X* **2,** 89–124 (2016).

[202] A. F. Vincent, J. Larroque, N. Locatelli, N. Ben Romdhane, O. Bichler, C. Gamrat, W. S. Zhao, J. O. Klein, S. Galdin-Retailleau & D. Querlioz. Spin-transfer torque magnetic memory as a stochastic memristive synapse for neuromorphic systems. *IEEE Trans. Biomed. Circuits Syst.* **9,** 166–174 (2015).

[203] D. Zhang, L. Zeng, K. Cao, M. Wang, S. Peng, Y. Zhang, Y. Zhang, J. O. Klein, Y. Wang & W. Zhao. All Spin Artificial Neural Networks Based on Compound Spintronic Synapse and Neuron. *IEEE Trans. Biomed. Circuits Syst.* **10,** 828–836 (2016).

[204] D. Mahalanabis, M. Sivaraj, W. Chen, S. Shah, H. J. Barnaby, M. N. Kozicki, J. B. Christen & S. Vrudhula. Demonstration of Spike Timing Dependent Plasticity in CBRAM Devices with Silicon Neurons. *2016 IEEE Int. Symp. Circuits Syst.* 2314–2317 (2016). doi:10.1109/ISCAS.2016.7539047

[205] M. Prezioso, F. M. Bayat, B. Hoskins, K. Likharev & D. Strukov. Self-Adaptive Spike-Time- Dependent Plasticity of Metal- Oxide Memristors. *Nat. Publ. Gr.* 2–7 (2016). doi:10.1038/srep21331

[206] N. Du, M. Kiani, C. G. Mayr, T. You, D. Bürger, I. Skorupa, O. G. Schmidt & H. Schmidt. Single pairing spike-timing dependent plasticity in BiFeO 3 memristors with a time window of 25 ms to 125 μ s. *Front. Neurosci.* **9,** 1–10 (2015).

[207] S. Li, F. Zeng, C. Chen, H. Liu, G. Tang, S. Gao, C. Song, Y. Lin, F. Pan & D. Guo. Synaptic plasticity and learning behaviours mimicked through Ag interface movement in an Ag/conducting polymer/Ta memristive system. *J. Mater. Chem. C* 5292–5298 (2013). doi:10.1039/c3tc30575a

[208] X. Hu, A. Timm, W. H. Brigner, J. A. C. Incorvia & J. S. Friedman. SPICE-Only Model for Spin-Transfer Torque Domain Wall MTJ Logic. *IEEE Trans. Electron Devices* **66,** 2817–2821 (2019).

[209] É. D. Fabian Pedregosa, Gaël Varoquaux, Alexandre Gramfort, Vincent Michel, Bertrand Thirion, Olivier Grisel, Mathieu Blondel, Peter Prettenhofer, Ron Weiss, Vincent Dubourg, Jake Vanderplas, Alexandre Passos, David Cournapeau, Matthieu Brucher, Matthieu Perrot. Scikit-learn: Machine Learning in Python. *J. Mach. Learn. Res.* **19,** 29–33 (2015).

[210] H. Hazan, D. J. Saunders, H. Khan, D. Patel, D. T. Sanghavi, H. T. Siegelmann & R. Kozma. BindsNET: A machine learning-oriented spiking neural networks library in python. *Front. Neuroinform.* **12,** (2018).